Abstract

Background:

3D printing is a relatively new process that allows rapid prototyping and additive manufacturing. Fused Filament Fabrication (FFF), also referred to as Fused Deposition Modelling (FDM, a copyrighted acronym of Stratasys Inc.), is a 3D printing process in which layers of extruded fibres are deposited to form a component. FFF is an attractive method for flexible manufacturing – there are no tooling costs associated with altering products as it fabricates complex geometries by printer movements generated directly from CAD data. FFF is rarely used to produce 'end-use components' (ie. manufacturing products using FFF rather than simply rapid prototyping) due a lack of characterisation of mechanical properties of the printed material.

Aims and Research Questions:

The study aims to progress FFF towards producing end-use components by developing mechanical property models of the printed material. In particular, the study seeks to answer three questions:

- Is it possible to predict the mechanical behaviour of FFF-ABS material?
- Is it possible to predict this behaviour consistently if the parts are produced using a consumer-level printer, as the machine may not have the same precision as industrial printers previously used in research?
- Can post-fabrication annealing 'heal' the effects of a varied temperature history on the material, allowing more consistent mechanical properties and thus a more accurate mechanical characterisation?

Research Process:

Annealed and non-annealed (control) tensile testing specimens were fabricated on a consumer-level FFF printer. These specimens were tested in a tensile load frame, giving experimental elastic and strength properties. Microscopy of the material cross-section was used to estimate the interfibre bonding length and material void content in the material,

which were used as inputs to develop the mechanical model. A simple strength model of FFF-ABS was produced and applied, and previously established elastic characterisation methods were used to predict the tensile elastic modulus.

Some previous studies' experimental testing methods were discovered to have flawed tensile coupon design and shear characterisation tests. Therefore the experimental process designed and employed an alternative shear characterisation and coupon fabrication method. A printer g-code generator was also developed as current 'CAD to printer pathing' software does not allow precise control over the fabrication properties.

Research Findings:

- A comprehensive list of parameters influential to the mechanical properties of the material was developed, including the effects of printing parameters, extrusion parameters and bulk material properties. This establishes the background for further research into the process.
- Post-fabrication annealing was found to have an insignificant effect on the material properties, suggesting that the temperature control commonly seen on consumer-level printers is adequate for production of end-use components.
- The developed strength modelling techniques were found to correlate very well with the experimental data as well as 2 external datasets.
- Elastic modelling procedures developed by Renaud et al. (1999) were applied to the experimental data and found to correlate reasonably well.

Significance of Findings:

Findings suggest that the established elastic properties model and the developed strength model can be used to estimate material laminate properties with a reasonable degree of accuracy. Effective orthotropic material strengths of FFF-ABS laminate are now able to be estimated under plane stress assumptions. The research presents a comprehensive survey of the influential factors and their effects on the material properties, which may eventually allow for structural end-use component design and fabrication.

Acknowledgements

Dedicated to my mum, Lynne McAlister.

Thanks to Lydia Kavanagh, for your helpful guidance.

Thanks to John Scott at Cartesian Co., for all your help over the past year.

Thanks to Hayley Wilkinson for being a pretty lovely lady to hang out with.

This study is in accordance with the open notebook science philosophy.

Data, research and analyses produced during the study can be found at

www.thistinypla.net/FFFThesis

Contents

List of Figures

List of Tables

Glossary

Printing	The 3D printing process used to produce a part.
FFF	Fused Filament Fabrication, the investigated 3D printing method.
Printing	The 3D printing process used to produce a part.
Bulk Material	The polymer material, before being used in the FFF process.
ABS	Acrylonitrile-Butadiene-Styrene, the bulk material used in the study.
FFF-ABS	The 'effective material' after the ABS has been subjected to the FFF process.
Part	A physical object produced using a 3D printer.
Component	A physical object produced using a 3D printer.
Microstructure	Microscopic structure, at the scale where polymer mechanics effects are relevant – 200x magnification or more.
Mesostructure	Structure between the Micro- and Macro- level. At this level, the ABS fibre, inter-fibre bonding and air gap are all apparent – approximately 50x-200x magnification (0.$\tilde{0}$5 mm detail visible)
Macrostructure	Component body structure, visible to the naked eye.
Macroscopic	Macroscopic properties refer to effective mechanical properties of the printed material.
FE	Finite Element
FEM	Finite Element Method
RVE	Representative Volume Element
Filament	The 'bulk' ABS cord that is fed into the printer (1.75 mm nominal diameter).
Fibre	The ABS fibre present in the finished material after extrusion (0.4 mm nominal diameter).

Isotropic	Material properties are constant regardless of material orientation.
Anisotropic	Material properties depend on the orientation of the material.
Orthotropic	Properties of material are constant along three material axes normal to each other.
Monoclinic	Properties have one plane of symmetry with normal parallel to fibre axis.
Transversely Isotropic	Material has one symmetry axis, along the fibre axis.
Young's Modulus	Material property: Stiffness of the material; ratio of stress to strain under tensile loading.
Shear Modulus	Material property: Ratio of shear stress to shear strain under shear loading.
Poisson's Ratio	Material property: Ratio of transverse and axial strains under tensile loading. Poisson's ratio notes how much a specimen will contract in the direction normal to applied tensile loading.
Coupon, Test Specimen	The printed 'strap' component loaded during tensile testing.
Interfibre shear strength	The material strength against a between-fibre shear failure.
Intralaminar shear strength	Same as interfibre shear strength: the material strength against a between-fibre shear failure.
Bounding Box Area	Refers to the total area taken up by the part (ie. fibres and voids). Equivalent to the CAD file input/geometry input.

List of Symbols

S_{ij} Mechanical strength. Subscripts indicate strength axis [MPa].

S_{ty} Tensile yield strength of bulk ABS material [MPa].

S_{sy} Shear yield strength of bulk ABS material [MPa]

C_{ij} Elastic coefficients of the Hookean stress-strain relationship [MPa].

σ_i Stress in i direction [MPa]

$1, 2, 3$ Material axes notation: 1 is parallel to the fibre axis, 2 and 3 are perpendicular to fibre axis.

x, y, z Global axes notation: x is direction of applied tensile stress; y and z are perpendicular to this axis.

ρ_1 Void density (ratio of material void area to material total area) in the transverse plane.

ρ_2,ρ_3 Void density (ratio of material void area to material total area) in the planes parallel to the fibre axis.

A Composite material area – area taken up by the 'bounding box' of the fibre or design area. $[mm^2]$

A_f Fibre area – area of the fibres in the composite. Equivalent to $A(1-\rho_1)$ $[mm^2]$.

A_v Void area – area of the voids in the composite. Equivalent to $A\rho_1$ $[mm^2]$.

d Diameter of the extruded ABS fibre [mm].

1: Introduction

1.1 Background and Justification of Research

3D printing has recently received attention for allowing manufacture of components previously not possible. Artificial heart valves, aircraft components and houses have all been 3D printed (Lilleholm, 2014). 3D printing has many advantages over traditional subtractive manufacturing: the process allows waste-free, labour-free and near-instant production of a bespoke component. Companies such as Ford, Boeing, General Electric and NASA have realised the potential of the technology and have invested heavily in the research and development of the process (Boulton, 2013).

3D printing allows for decentralised and digitally distributable manufacturing whereby components can be downloaded and printed locally and on-demand. Fused Filament Fabrication (FFF)[1] is a 3D printing process in which polymer fibres are extruded in layers to additively manufacture a component. FFF can produce bespoke parts with no initial tooling, allowing flexible manufacturing and lower relative start-up cost. Due to the 'layer by layer' nature of the fabrication, FFF also allows production of components difficult to manufacture using conventional subtractive methods, such as freeform surfaces or complex internal geometries (Cantu and Jonsson, 2012).

1.2 Impact and Applications of Research

FFF has tremendous potential both as a manufacturing method and as a tool for humanitarian use. Examples already exist of FFF-fabricated prosthetics being produced at far cheaper cost than commercial offerings (McCue, 2014). Conductive printing filament has also been used to produce some rudimentary sensors, which could see working electronic or biomedical components being printed in the future (Leigh et al., 2012). Distributed filament production, in which waste plastic is recycled locally into 3D printing material, has a more positive impact on the environment than conventional recycling in rural areas (Kreiger et al., 2013). The 3D printing process would have multiple benefits in areas

[1]Also known as FDM. The FDM acronym is trademarked by Stratasys Inc.

such as Nepal, where trash is commonly burnt rather than recycled – a distributed recycling, filament production and printing system could ease local air pollution, create local industry and allow needed medical components to be printed locally and inexpensively. 3D printing also has potential industrial applications in removing the cost of maintaining a spares inventory – by replacing the spare with a printed part during the replacement order lead time.

FFF is currently mainly used to produce non-load-bearing parts for rapid prototyping; there is little application to the production of load-bearing end-use[2] components. Part of the reason for this is the lack of knowledge surrounding mechanical characterisation of the FFF material. It is theorised this knowledge gap exists due to the small financial incentive for industrial investment in FFF research: 3D printing methods already exist for engineering materials such as metals and ceramics, and FFF-based production does not enjoy benefits from economy of scale[3]. FFF material can be weak and unreliable if printing parameters are poorly set, and characterisation of the mechanical behaviour is difficult due to the composite nature of the printed material.

The majority of prior research on the FFF process has been done using expensive industrial machines. The expense associated with purchasing and running these machines would remove a lot of the aforementioned benefits. If the mechanical behaviour of the FFF-ABS material produced by a consumer-level printer can be adequately characterised, however, these benefits could make FFF an attractive distributed manufacturing process. This lack of mechanical characterisation forms the knowledge gap that the thesis aims to address.

[2]'End-use' components defined as components printed as the final product; ie. not a rapid prototype.

[3]A single-unit production run will have the same per-unit cost as a large production run, as components are fabricated without cost-reducing unit-specific tooling.

1.3 Goals and Research Questions

The overall goal of the investigation is to progress application of the FFF process towards manufacturing reliable load-bearing end-use components on consumer-level printers. The work aims to do this by producing a simple mechanical characterisation of the FFF-ABS material. Specifically it asks two research questions:

- Is it possible to predict the mechanical behaviour of FFF-ABS material?
- Is it possible to predict this behaviour consistently if the parts are produced using a consumer-level printer, as the machine may not have the same precision as industrial printers previously used in research?

During the investigation it was found that temperature history of the material played a large role in determining the mechanical properties. It was theorised that post-fabrication annealing of the printed component would thus result in more consistent mechanical properties, especially in consumer-level printers where poor temperature control is commonly seen. A third research question was constructed to investigate this phenomena:

- Can post-fabrication annealing 'heal' the effects of the temperature history on the material, allowing more consistent mechanical properties and thus a more accurate mechanical characterisation?

This question underpins both of the previous research questions.

1.4 Contents of Report

This report details the investigation of these three research questions.

- Section 2 presents an overview of the the FFF process.
- Section 3 discusses manufacturing parameters influential to the mechanical strength of the final part.
- Section 4 investigates prior mechanical characterisation research and develops strength characterisation methods. The study then uses the tensile test method to evaluate the mechanical characterisation methods.

- Section 5 details the experimental design process for the tensile testing.
- Section 6 presents experimental results of the mechanical testing;
- Section 7 compares the theoretical and experimental results and discusses the relevance to the constructed mechanical model. Weaknesses and improvements to the testing methods are also discussed.
- Section 8 concludes the report by presenting the conclusions of the investigations.

2: Fused Filament Fabrication (FFF)

2.1 FFF Process Overview

FFF produces components by progressively extruding layers of plastic fibre. A 3D CAD model is 'sliced' by software into multiple layers with a fixed thickness. The sliced model is converted to G-code and sent to the printer. The printer then follows the G-code directions to extrude each layer of ABS fibre. This printing process is illustrated in Figure 2.1.

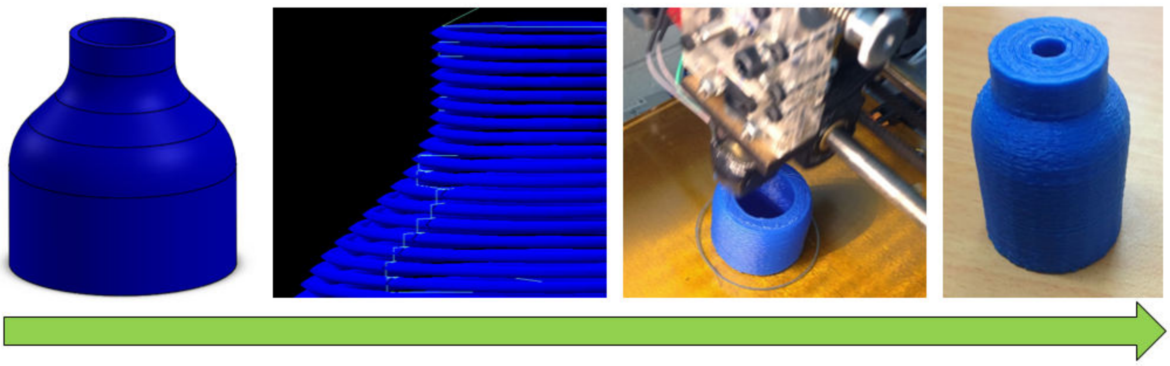

Figure 2.1: Manufacturing process of an FFF component

The *slicing stage* takes the CAD model (saved as a stereolithography .stl file) and describes the geometry as an assembly of fixed-height horizontal layers. These layers then constitute the actual geometry of the component. These layers can be seen in Figure 2.1. It is evident that the slicing of the part determines the alignment of the printed fibres in the part – as the FFF-ABS material strength is dependent on this alignment, the slicing stage contributes significantly to the mechanical performance of the final part (Ahn et al., 2002).

The *extrusion stage* takes the layer-based description of the part and extrudes the fibres layer by layer – the bulk ABS material is pushed through the hot-end of the extrusion head, and layered onto the build platform as seen in Figure 2.2.

2.2 FFF Printed Mesostructure

As the produced part is constructed of layers of fibres, the printed material is by nature anisotropic[1]. The FFF-ABS material acts as an composite of the extruded fibres, the

[1]Anisotropic: Material properties depend on the material orientation; not homogenous.

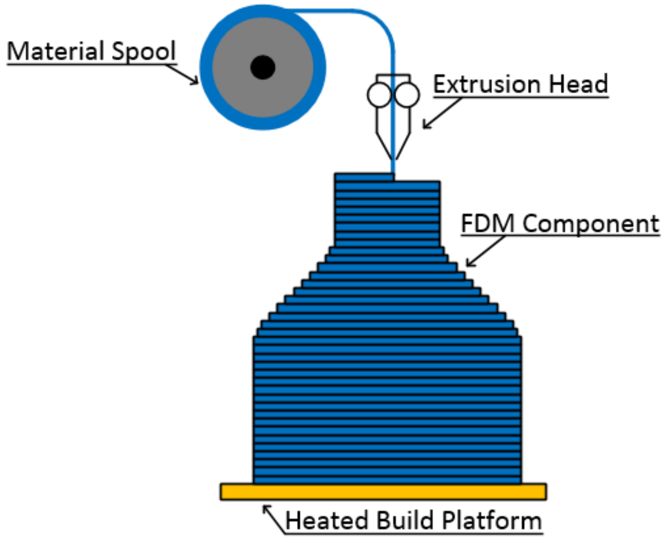

Figure 2.2: The extrusion stage of the FFF process

inter-fibre bonds and the air gaps between fibres (Li. et al., 2001). Whether the composite is orthotropic[2], monoclinic[3] or transversely isotropic[4] is a matter of debate. This study chose to model the composite as orthotropic as it is the most general form. This composite mesostructure of the FFF-ABS material is illustrated in 2.3.

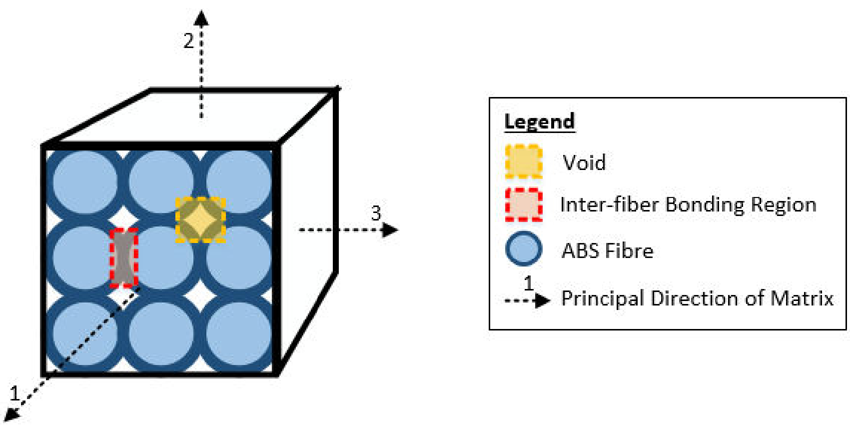

Figure 2.3: Composite mesostructure of FFF-ABS.

Figure 2.4 shows a 3-dimension view of the material mesostructure[5] and the material coordinate system used in this study. 1 denotes the principal fibre axis; 2 and 3 denote the transverse and thickness axes respectively.

[2]Orthotropic: Properties are constant along three material axes normal to each other.
[3]Monoclinic: Properties have one plane of symmetry with normal parallel to fibre axis.
[4]Transverse Isotropy: Material has one symmetry axis along the fibre axis.
[5]Structure between the Micro- and Macro- level. At this level, the ABS fibre, inter-fibre bonding and air gap are all apparent. The mesostructure level exists at approximately 50x-200x magnification (0.05 mm detail visible)

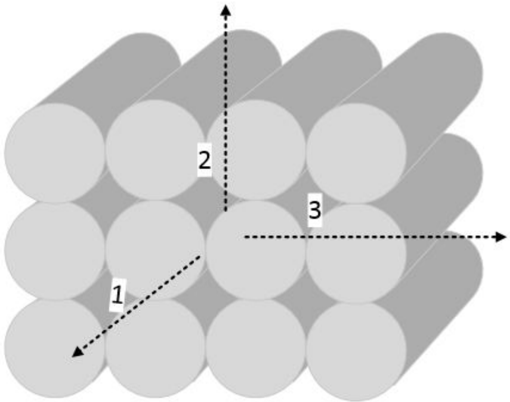

Figure 2.4: 1-2-3 Material Coordinate System

Previous research into the FFF was compared and it was found that the mechanical properties of the composite are a strong function of several controllable factors.

3: Influential Fabrication Parameters

3.1 Overview

The factors contributing to the mechanical properties of an FFF part are illustrated in Figure 3.1; the data supporting this diagram incorporates independent evaluation as well as research conducted by Sood et al. (2009), Renaud et al. (1999), Rodriguez et al. (2000), Ahn et al. (2002) and Li. et al. (2001).

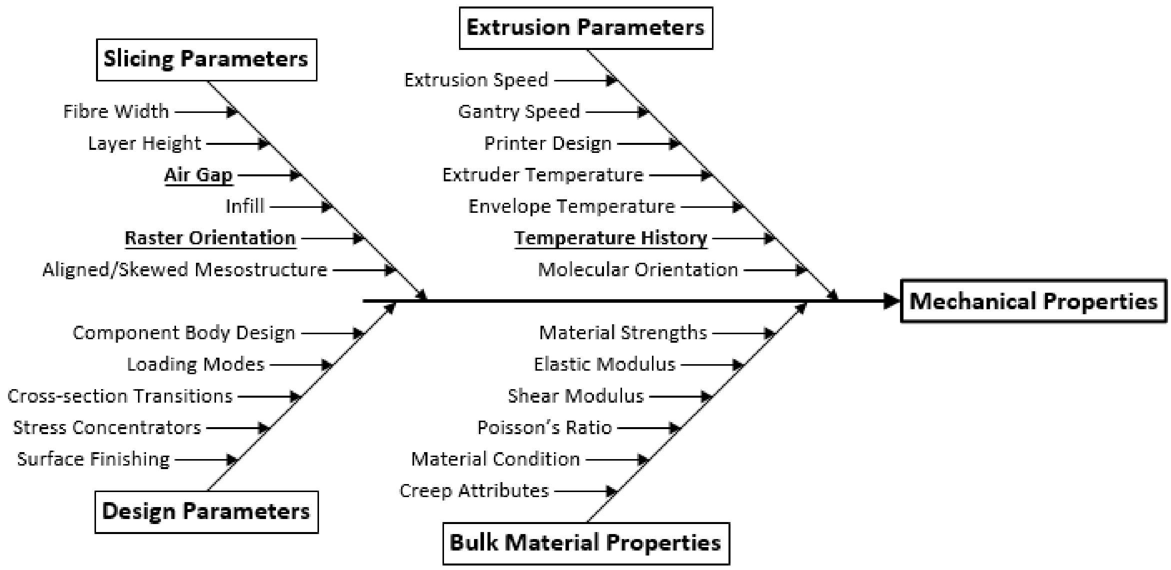

Figure 3.1: Factors contributing to mechanical performance

Only the factors underlined in Figure 3.1 were varied during the study. As all factors in the fishbone diagram are influential, however, it is constructive to explain the meaning and influence of each. Sections 3.2–3.5 explain each factor in detail, presenting a comprehensive list of influential factors and representing a major component of this research.

3.2 Slicing Parameters

3.2.1 Overview

The 'Slicing Parameters' were categorised as the parameters set during the slicing stage of the process. Printer pathing is usually generated by a slicing program that automatically controls the slicing parameters. In this study, however, a manual g-code pather (referred to as 'OGCode') was programmed and used; this allowed greater control over the slicing parameters of the finished part. This g-code pather is attached in Appendix A. The source code of the 'OGCode' pather is worth viewing as it gives insight into how the printer is controlled and how the printed part is deposited.

3.2.2 Layer Height and Fibre Width

'Layer Height' is the height of each slice of the printed component; 'Fibre Width' is the width of the extruded ABS fibre. As the filament is extruded onto the workpiece, the fibre cools and shrinks into a mesostructural shape that highly dependent on the vertical distance from the nozzle to the workpiece (Rodriguez et al., 2000). If the nozzle does not have enough spacing relative to the workpiece, the extruded fibres will be compressed into space already occupied by other fibres, which results in part defects. Figure 3.2 shows an extreme example of this phenomena.

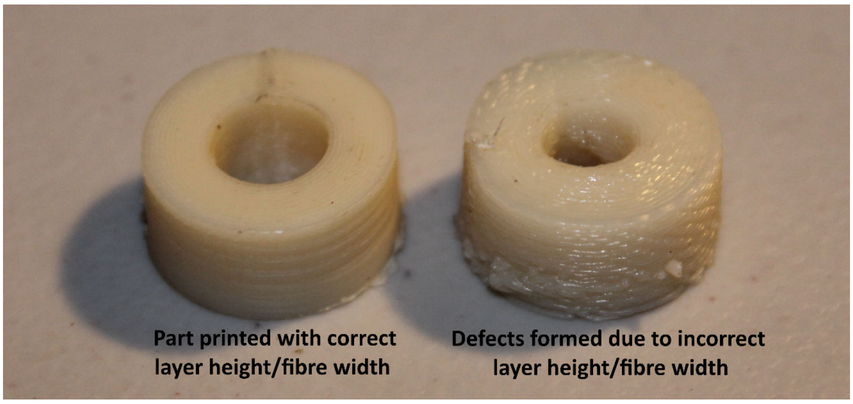

Figure 3.2: Comparison of correct and incorrect fibre width/layer height parameters.

If the nozzle has too much spacing relative to the workpiece, the extruded fibres may have insufficient contact with the parallel fibres to make a good inter-fibre bond. This can also result in an inconsistent mesostructure being produced. Figure 3.3 shows microscopy of the mesostructure resulting from excessive nozzle-workpiece spacing.

Extruding fibre into free space will give a circular fibre of the same width as the nozzle. The fibre width is changed when extruding onto a component, however, as the fibre shape becomes constrained by the previously solidified fibres. The fibre width is a function of the layer height and the *air gap* build parameters.

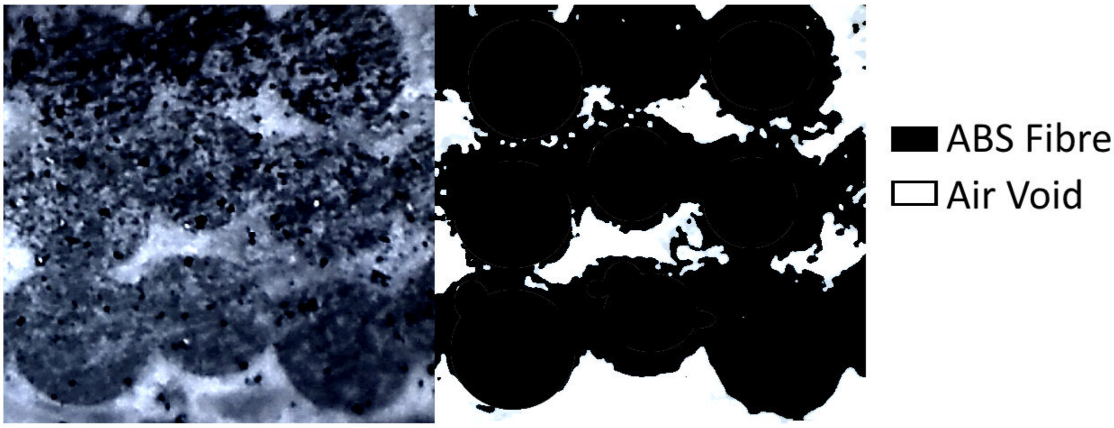

Figure 3.3: Microscopy of mesostructure resulting from excessive interfibre spacing.

3.2.3 Air Gap

'Air Gap' is defined as the distance between adjacent extruded fibres. For example, if adjacent fibres of width 0.4 mm are deposited with 0.36 mm axis to axis distance, the air gap is -0.04 mm. Setting a negative air gap in this manner will increase the transverse and intralaminar shear strength of the print, as the air gap directly alters the bond area between adjacent fibres (Ziemian et al., 2012).

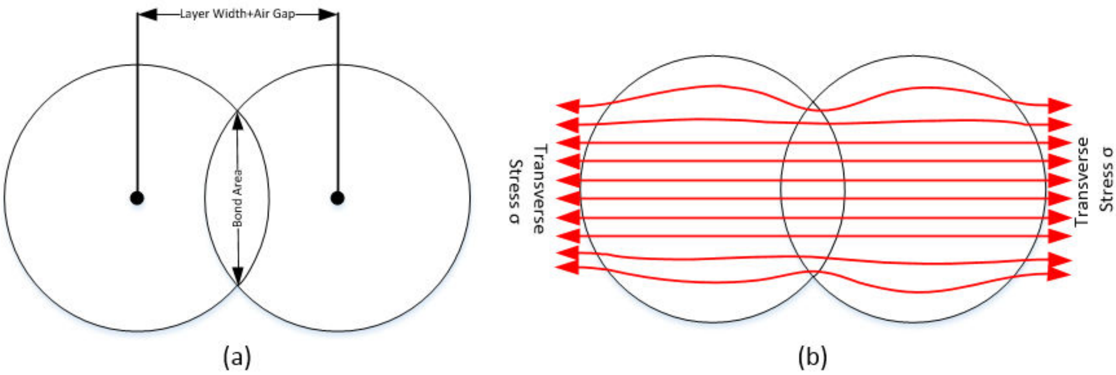

Figure 3.4: (a) Illustration of air gap notation (negative air gap); (b) Force line diagram showing transverse force lines passing through bond area.

As seen in Figure 3.4(b), the bond area gives an effective cross-sectional area for transverse loading. As all transverse or interfibre-shear force must be transferred through the bond area, this region is the 'weakest link' for transverse and shear loading. Mechanical performance under these loading modes is therefore directly dependent on the air gap. Figure 3.5 shows the decrease in transverse bond area with increasing air gap. Of particular note is the very small bond area for air gap settings of 0.0 mm.

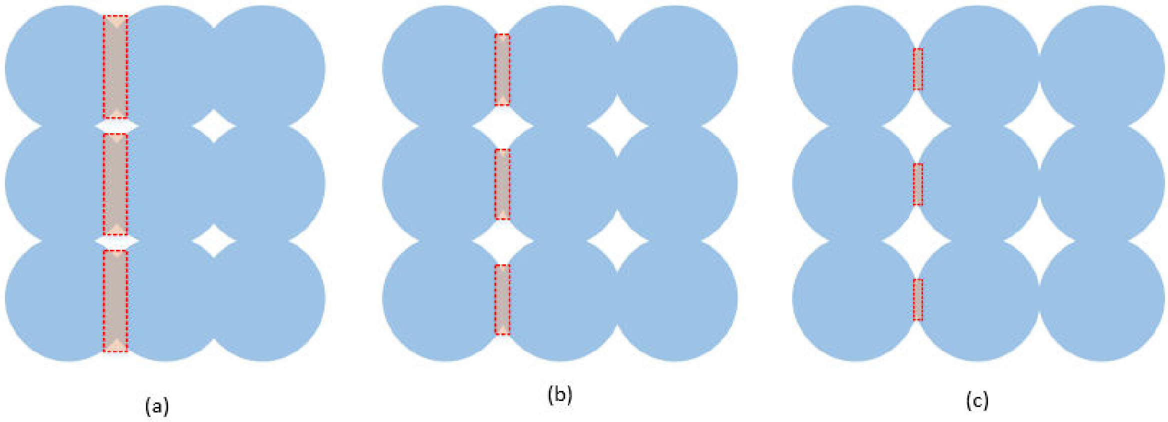

Figure 3.5: Illustration of the change in transverse bond area (shown by red areas) with changing air gap: (a) Large negative air gap; (b) Small negative air gap; (c) Approximately zero air gap.

In this study, layer height and fibre width are used to refer to the vertical and horizontal spacing disregarding the air gap. The actual height increase per deposition layer is thus layer height plus the air gap and the actual horizontal distance between adjacent fibres is the fibre width plus the air gap[1]. This study set the layer height and fibre width parameters as equal to the nozzle diameter as this produced circular fibre depositions that allow for more reliable part tolerances[2]. Evaluative testing was carried out to determine the optimal air gap for the 0.4 mm extruder nozzle; –0.04 mm was found as the air gap resulting in maximum interfibre bonding area without significant probability of part defects.

3.2.4 Infill

Conventional slicing programs feature *infill pathing*, which fill in the cores of solid objects with low-density fibre patterns. Low-density infill pathing routines are commonly used in models or prototypes to save weight and material in non-structural components. As the mechanical properties of FFF components are not well understood even without this added complexity, the infill method used was full-density unidirectional rectilinear pathing. Figure 3.6 shows an example of unidirectional rectilinear infill.

[1]Note that the air gap is usually negative.

[2]If the layer height is smaller than the nozzle diameter, the fibre is compressed into an elliptical shape. As fibres being deposited in sucessive horizontal lines only have one adjacent fibre to support them, fine dimensional tolerance is harder to achieve.

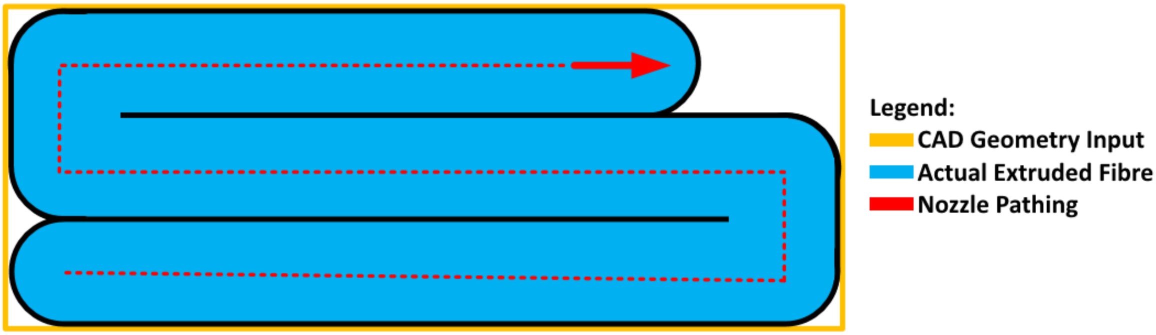

Figure 3.6: Illustration of the full-density unidirectional rectilinear pathing.

3.2.5 Raster Orientation

'Raster Orientation' defines the direction of the fibre axis with respect to the FFF component. For a uniaxial tensile test, the angle between the load axis and the fibre axis defines the raster orientation. This is illustrated in Figure 3.7.

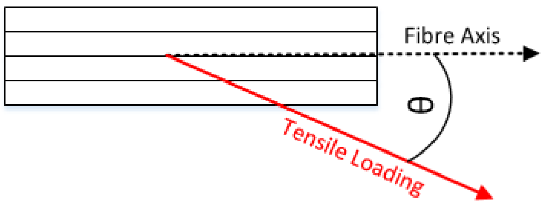

Figure 3.7: Illustration of the raster orientation angle θ.

Studies have been conducted into the tensile strength of FFF-ABS specimens with varying raster angles. Ahn et al. (2002), Ziemian et al. (2012), Sood et al. (2009) and Tymrak et al. (2014) found the mechanical properties of tensile specimens to be a strong function of raster orientation. Tensile yield strength varied from approximately 20–25 MPa for the $\theta = 0°$ case to approximately 3–15 MPa for the $\theta = 90°$ case across these studies[3]. A review of 'strength vs. orientation' studies was undertaken; this review revealed issues with some methods used to tensile test the FFF components. These issues are explained further in Section 7.4.2. Based on these insights, studies by Tymrak et al. (2014) and Sood et al. (2009) were not included in the review data. As the area of study is such an unexplored field, this left very little valid data to review. The strength vs. raster orientation plot of the reviewed data is shown in 3.8.

As the raster orientation is changed, the failure mode also changes: stress along

[3]A large part of this variation can be attributed to the differing air gap and ABS material grades.

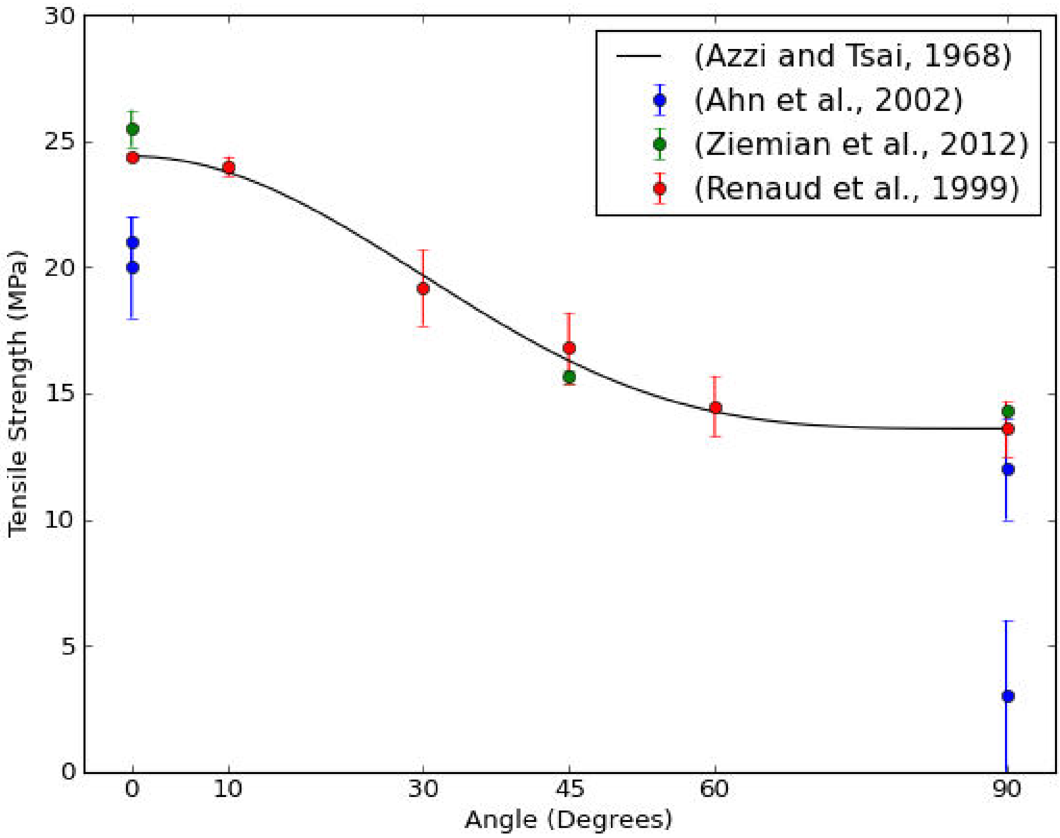

Figure 3.8: Review of studies of Tensile Strength vs. Raster Orientation θ.

$\theta = 0°$ will cause failure along the fibres; stress along $\theta = 90°$ will cause failure in the interlayer bonding region; stress along an axis between the two angles will cause a combination of axial, transverse and shear stresses and an associated combined failure mode. Renaud et al. (1999) cites this as a possible reason for the relatively large error in the $\theta = 30, 45, 60$ data. The failure strength curve fit is based on the failure surface theory from Azzi and Tsai (1968). The failure surface theory is explained further in Section 4.

Raster angle can also be made to vary over sucessive layers. Such practice is common in composites manufacturing, as it allows fibre axis to be oriented in multiple directions, giving required strength and stiffness in more directions. Some mechanical testing has been done on multiple orientation FFF laminates – this data is available in Ahn et al. (2002) and Ziemian et al. (2012). Only unidirectional laminates are be examined in the study.

3.2.6 Aligned/Skewed Mesostructure

Renaud et al. (1999) and Rodriguez et al. (2000) presented mechanical testing of FFF parts built using *skewed* mesostructure, in which slices are offset so fibres are deposited between peaks of fibres on the layer below. This was seen as introducing unnecessary complexity – printer slicing and part supports would have to be planned around the overhanging edge fibres. As noted by Jose F. Rodriguez (2001), the skewed mesostructure components are also weaker and less stiff than the aligned mesostructure components. This leads there to be no logical reason to use them in design of a part. Aligned mesostructures were used in the experimental study.

3.3 Bulk Material Properties

3.3.1 Overview

'Bulk material properties' refer to the material properties of the bulk printer filament – the polymer itself, before being fabricated into a composite material. Printer filament is sold commercially in a wide variety of plastic materials and material blends, including PLA (Polylactic Acid), Polycarbonate, Nylon, ASA (Acrylonitrile Styrene Acrylate) and HDPE (High-Density Polyethylene). Of these, ABS and PLA (PolyLactic Acid) are most commonly used. ABS was employed as the material for this study as it has a larger body of background data to compare to. Only one research article was found into the material properties of FFF-PLA, conducted by Tymrak et al. (2014).

ABS FFF filament is produced by adding finely shredded ABS pellets to a hopper, which feeds an extrusion chamber. The chamber extrudes a nominal diameter filament (commonly 1.75 mm±0.05 mm).

One of the issues of using FFF as a production method is that very few filament manufacturers supply material datasheets with the filament – as printed material properties are dependent on the bulk material properties, this leads to uncertainty in the mechanical performance of the final part. Though most filament material grade is unspecified, it is likely that a given filament is a standard grade such as PA-747 or P400. ABS filament specified as PA-747 was used in this study as it was the only grade available with an associated material datasheet. This issue is discussed further in Section 7.4.1. Filament supply was purchased from *3DMakerWorld*, which uses bulk supply from *Chi-Mei Corporation*. The relevant bulk material properties are reproduced from (Chi-Mei-Corporation, 2006) in Table 3.1. Further properties can be found in Appendix D.

Table 3.1: Bulk material properties of PA-747 ABS.

Property	**Value**	**Standard**
Material Grade	ABS	PA-747
Density	1.03 g/cc	ISO 1183
Linear Mold Shrinkage	0.003–0.007 mm/mm	ASTMD955
Melt Flow Rate	13 g/10 mins at Load 10.00 kg, Temperature 220° C	ISO-1133
Tensile Strength at Yield	31.0 MPa	50 mm/min; ISO 527
Elongation at Break	45%	50 mm/min; ISO 527
Flexural Strength	58.0 MPa	2 mm/min; ISO 178
Flexural Modulus	1.80 GPa	2 mm/min; ISO 178
Vicat Softening Point	92.0°C at Load 5.00kg, 94.0° C at Load 5.00 kg 101° C at Load 1.00 kg 103° C at Load 1.00 kg	50°C/hr; ISO 306 120° C/hr; ISO 306 50° C/hr; ISO 306 120° C/hr; ISO 306

This section presents some of the characteristic properties of the ABS material and how these properties influence the strength of the final part.

3.3.2 Material Strengths

Material strength refers to the maximum stress before yield (*yield strength*) or break (*ultimate strength*) of a material. ABS yield occurs at the maximum material strength. This indicates that any constant stress that exceeds the yield strength will also result in ultimate failure of the material; therefore post-yield behaviour is irrelevant for the purposes of this study (Lokensgard, 2004).

The tensile, compressive and shear strengths of the bulk filament material are a major determining factor in the tensile, compressive and shear strengths of the printed material – however, there exists no simple relationship between the two strengths as factors such as mesostructural stress concentrators must be taken into account. Methods to predict the strength of the printed material are presented in 4.4.

3.3.3 Elastic Properties

Li, Sun, Bellehumeur, and Gu (2002) and Renaud et al. (1999) showed that the elastic properties of the printed component are directly proportional to the elastic properties of the bulk ABS material. ABS elastic properties vary widely with the the Acrylonitrile, Butadiene and Styrene composition of the material, as well as any additives. ABS has an elastic modulus of 1.00–2.65 GPa (Datavase, 2014); information on shear modulus and poisson's ratio of any filament material was not available. For this reason, indicative poisson's ratio values are used from Renaud et al. (1999). This approach was also employed by Li, Sun, Bellehumeur, and Gu (2002).

3.3.4 Material Condition

ABS filament absorbs airborne moisture from the surrounding air. Due to this phenomena, filament must be stored in an airtight container with a desiccant such as silica gel present. Test prints were done using two filament sources – one stored without desiccant, the other (the experimental feedstock) stored with desiccant. Figure 3.9 shows the result of the test prints.

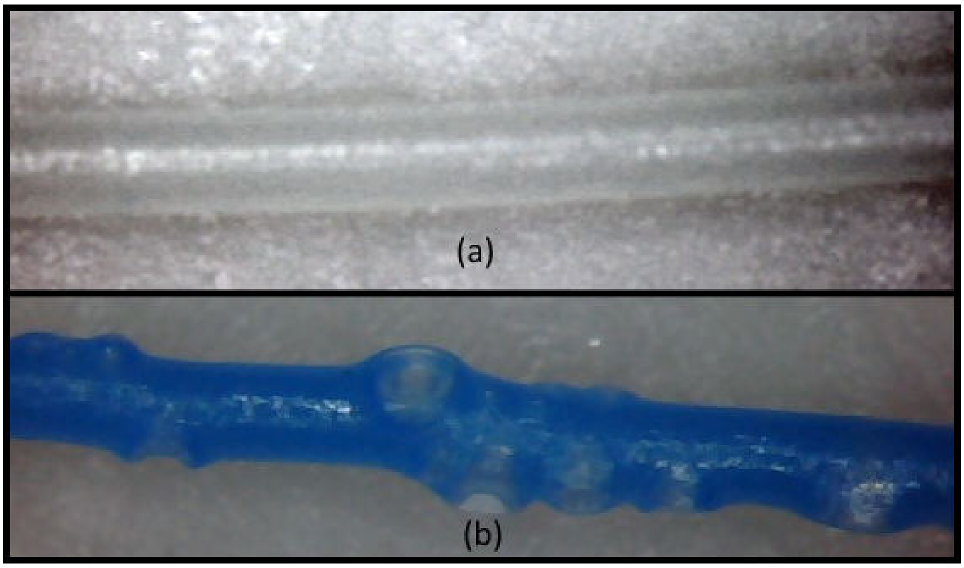

Figure 3.9: (a) Extruded filament stored with desiccant present; (b) 'Bubbling' phenomena produced from filament exposed to air.

The phenomena is due to the rapid boiling of the moisture when coming into contact with the extruder, which forms steam 'bubbles' in the semi-molten plastic. Bubbling induces a large amount of mesostructural deformation in the printed material, reducing print quality and part tolerance. It also very likely reduces strength and stiffness for obvious reasons. Material used in this study was stored in an airtight container with dessicant and no bubbling was observed during extrusion.

3.3.5 Creep Attributes

ABS plastic also has time-dependent stress relaxation/creep associated with mechanical loading – higher strain rates of the material tend to produce higher strength and stiffness results. Tymrak et al. (2014) cites this as a likely source of variation between experimental testing. The variation of strength with loading rate was kept constant in this experiment: a 2 mm/min strain rate as per standard ASTM D3039 was used (ASTM-International, n.d.). The selection of this rate is further discussed in Section 7.4.2.

3.4 Extrusion Parameters

3.4.1 Extrusion Speed and Gantry Speed

'Extrusion Speed' is defined as the feedrate of the material into the extrusion chamber. During printing, filament is driven by a gear coupled to a stepper motor into the extrusion feed chamber. The tangential velocity of this driven gear is denoted as the 'extrusion speed'. As the diameter of the filament is constant, the extrusion speed is directly proportional to rate of volume deposition of the print. 'Gantry Speed' is defined as the speed of the extruder head as it moves across the workpiece. These two concepts are analogous to the 'speeds and feeds' concepts in machining jargon.

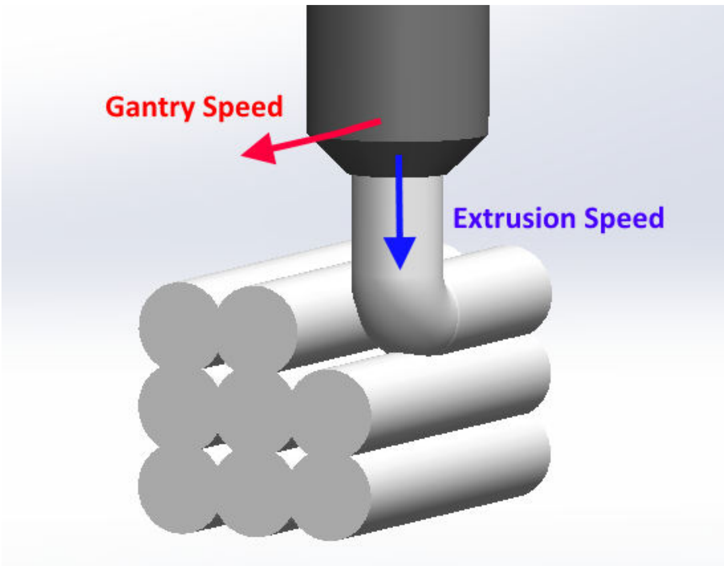

Figure 3.10: Illustration of Extrusion Speed and Gantry Speed

As as is the case with most FFF research, there has been little study into the effect of extrusion speed on the final component. Mesostructural microscopy produced by

Rodriguez et al. (2000) found that extrusion speed influences the shape of the extruded fibres: if the extrusion speed is above the gantry speed, too much plastic is extruded, and the fibre is squished in the horizontal plane by the nozzle; if the gantry speed is above the extrusion speed, not enough fibre is extruded, and the fibre cross-section shrinks as the nozzle is pulled away. Both of these effects are seen as unacceptably diminishing the dimensional tolerance of the final part. Based on these findings, the gantry speed and the extrusion speed used in the study were set as equal at 2700 mm/min. The magnitude of this value has been based on speed values commonly used on the same hardware.

3.4.2 Printer Design

Printer design necessarily plays a role in the development of the material characteristics. The printer model used in the study is a 'Solidoodle 3'[4]. Many consumer-level printers are very similar, consisting of the same basic elements shown in Figure 2.2. Printer design will determine the reproducibility of part fabrication; tests were conducted on the Solidoodle 3 and the machine was found to print very consistently after calibration. It was therefore assumed that manufacturing reproducibility of test specimens could be neglected in the study – ie. for the same g-code and printing parameters, the same component was fabricated. Printer design also plays a large role in determining the temperature conditions within the build chamber. 'Open' designs, such as the Solidoodle, are susceptible to temperature variation due to air movement. To reduce this effect, rudimentary sheeting of perspex and aluminium foil was used to 'wall off' the build area.

3.4.3 Temperature-Based Parameters

ABS is an amorphous material that exhibits a glass transition. In a glass transition, there is no 'step change' in phases – ABS will smoothly transition from a 'glassy' solid state to a 'rubbery' liquid state over a temperature range (Lokensgard, 2004). The material properties are also subject to the a smooth transition between values as the phase changes. This glass transition occurs at approximately 105°C (Datavase, 2014). If the extruder temperature is too high, the ABS will become chemically unstable and decompose, forming noxious gases. This tends to occur if extruder temperatures are much above 270°C (Li,

[4]Produced by the Solidoodle corporation (www.solidoodle.com)

Sun, Bellehumeur, and Gu, 2002). If the extruder temperatures are too low, the extruder nozzle will clog with the solidified ABS and extrusion cannot occur. In this study, the extruder temperature was set to 210°C based on the usual extrusion temperatures of the same hardware.

'Envelope Temperature' refers to the temperature of the build environment. This study set the envelope temperature at 70°C to allow direct comparison of results with previous studies conducted by Ahn et al. (2002) and Ziemian et al. (2012). Thomas and Rodriguez (2000) showed that raising the envelope temperature increased the fracture strength between the fibres, leading to greater transverse strength. An increase from 70°C to 80°C resulted in an approximately 5% increase in strength.

This increase in strength is explained by thermal contraction effects. As the fibre is deposited, it shrinks due to thermal contraction[5]. This contraction has two negative effects on the strength of the printed part: the contraction introduces residual stresses to the material, as the material 'tries to pull away from itself' during cooling; and the bonding quality and bonding length between the fibres is reduced due to the reduced contact area. These effects lead to a lower fracture toughness and transverse/interfibre shear strength (Thomas and Rodriguez, 2000).

Temperature effects become more apparent as the number of specimen layers increases. As each layer is deposited, the part experiences a temperature fluctuation, increasing the amount of residual stress in the component (Sood et al., 2009). This provides the justification for the heat-treatment component of the investigation: if the final material can be annealed to 'heal' the effects of the contraction, the variation in properties due to localised different cooling conditions can be eliminated – making mechanical characterisation more consistent across the part.

The polymer bonding process occurs through 'reptation'[6] of polymer surfaces. As the fibre being extruded makes contact with the deposited part, the polymer chains on the surface of each fibre entangle and form bonds. This process is driven by the thermal energy of the extruded plastic (Bellehumeur et al., 2004). Finite-element heat transfer studies of this process have been carried out, notably in studies by Sin et al. (2008) and

[5]Chi-Mei Corporation (2006) quotes a linear mold shrinkage of approximately 0.003–0.007 mm/mm for PA-747 ABS.

[6]Named after the 'reptile' snake-like action of polymer chain entanglement.

Y. Zhang (2006). The salient points are that temperature history plays a large role in the bonding quality of the fibres, with the bonding quality and length increasing with increasing fibre contact time above the glass transition temperature. This 'neck growth' phenomena[7])is illustrated in Figure 3.11 Bellehumeur et al. (2004).

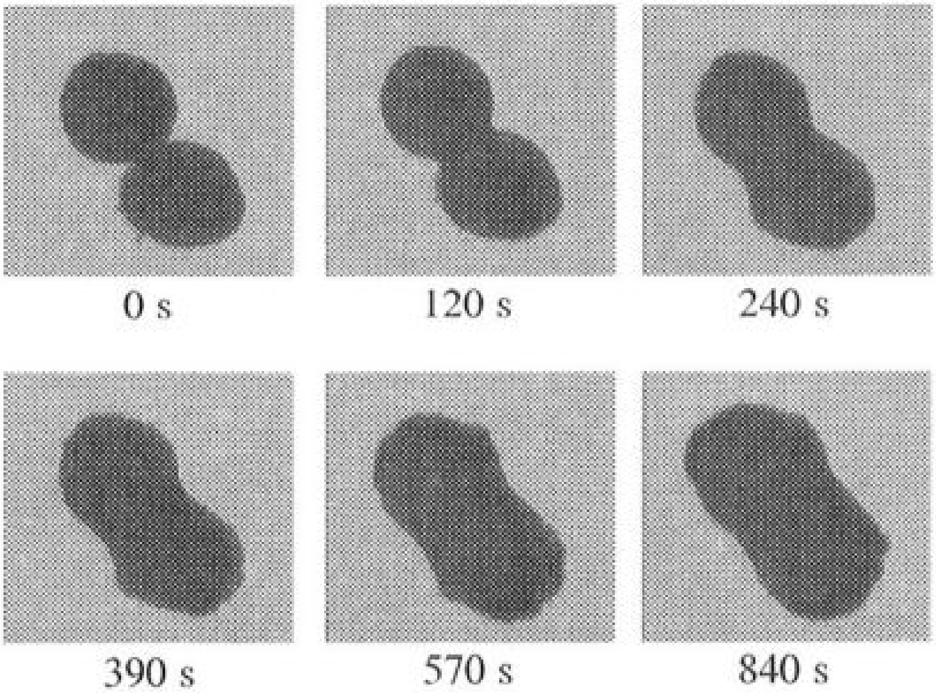

Figure 3.11: Neck growth with time, temperature of 200°C. Reproduced from Bellehumeur et al. (2004).

Bellehumeur et al. (2004) proposed a model for annealing of the fibre bond under constant temperature conditions. The model presents an *intrinsic healing function*, which is the ratio of the fracture toughness at time t to the fracture toughness of the virgin material. The full non-isothermal model can be found in Bellehumeur et al. (2004) and is not reproduced here.

The salient point is that for a specified temperature above the glass transition temperature, there exists a reptation time t after which the fibre bonds will be fully annealed. This time was estimated at approximately 90 minutes for a temperature of $125°C$ based on data presented by Thomas and Rodriguez (2000).

Tensile testing in this study attempted to anneal the material to a predictable state and compare this with control specimens. The annealing process was found to have

[7]The 'neck' referring to the inter-fibre bond.

an insignificant effect on the mechanical properties. It is theorised this is at least partly due to the near-constant envelope temperature afforded by the enclosed build chamber. Further discussion can be found in Section 7.

3.4.4 Molecular Orientation

Polymers can be subject to *molecular orientation*, in which the polymer chains change in alignment above the glass transition temperature. This can dramatically effect the strength and stiffness of the polymer, as the mechanical properties of the polymer chains are dependent on loading alignment. Polymers tend to have much more stiffness and strength along the polymer 'backbone' than transverse to this backbone (Landel and Lielsen, 1993). This effect is likely to increase the strength and stiffness of the final part along the fibre axis and reduce the strength and stiffness transverse to this axis. The printer nozzle 'draws out' the extruding fibre while moving across the workpiece, which is a similar process used to stiffen/strengthen some polymers along an extrusion axis in conventional manufacturing (Landel and Lielsen, 1993). A simple test to see if the material data quoted by a supplier is subject to molecular reorientation effects is given: if test results for annealed and control specimens are similar, molecular reorientation is likely not influential to the post-extrusion material properties. Section 7 shows that molecular orientation appeared to have no effect on the study, as the post-annealing specimens had very similar properties to the control specimens (ie. movement of the polymer chains above the glass transition temperature had no effect on the mechanical properties). Molecular orientation effects are dependent on the bulk material source and so is a factor to take into consideration in end-use manufacture.

3.5 Design Parameters

Design parameters are defined as set upon design of a real end-use FFF-ABS component. An initial research goal was to hydrostatically test printed 'pressure vessels', which were to be used to investigate the effect of body design parameters. Preliminary test vessels were fabricated and pressure tested, shown in Figure 3.12[8].

The burst pressure of these vessels was approximately 1100 PSI for an approxi-

[8]Thanks goes to John Scott at Cartesian Co. for the initial hydrostatic pressure testing.

Figure 3.12: Preliminary pressure vessels printed for design parameter investigation.

mately 1 cm thickness. As the basic strength characterisation of the FFF-ABS laminate is not well understood, this hydrostatic test method was not used in the final study. It is recommended future research uses this method to characterise the FFF-ABS material as it behaves in an end-use component, factoring in body design effects as listed in Figure 3.1. Further details on this can be found in Section 8.

4: Modelling of FFF-ABS

4.1 Modelling Overview

This section presents mathematical models for the mechanical characterisation of FFF-ABS. For the purposes of this study, a full mechanical characterisation is defined as solved when the displacement, stress state and material strength of any point in an arbitrary FFF-ABS body can be calculated. Mechanical characterisation therefore is distilled to two problems:

- Characterise the elastic properties, which can be used to predict the stresses and strains generated in the material by an applied load;
- Characterise the strength properties, which can be used to predict the stress at which that material will fail.

Composites modelling is extremely complex as opposed to the modelling of isotropic engineering materials such as steel. Average-stress or average-strain solutions of failure are not applicable to composite materials, which facilitates special composite characterisation theory (Bogetti et al., 1995). First-Order Shear Deformation Theory[1] is the most commonly used theory in practice, however it is not suitable to model a real FFF component. This is due to the theory only being applicable to thin shell structures[2] where the smallest dimension is approximately ten or more times larger than the thickness of the shell (Barbero, 2014). As FFF-ABS material has a relatively low strength, any structures made from them will likely need to be thicker than this restriction, rendering application of the theory invalid.

A proposed solution to this problem is to use the 'smear-unsmear' technique illustrated by Bogetti et al. (1995). Actual application of this process is outside the scope of this study, however various codes exist to allow FEM analysis of structures through use of this technique, making the process suitable to fulfill the 'enabling simple characterisation'

[1]Sometimes referred to by the acronym FSDT.

[2]Much of composite theory was developed for application in aerospace or high-performance vehicle body design, as thin shell structures provide high strength-to-weight ratios.

aim of the research. A 'smear-unsmear' analysis first decomposes the composite structure under analysis into sections of laminates, which are then each solved for the effective material properties – 'smearing' the complexities of the composite structure by modelling it as an equivalent homogenous material. Structural FEM analysis is then carried out on the 'smeared' structure, and the stress/strain field determined. This solution is then 'unsmeared' to find the stresses and strains in each lamina, which allows meaningful interpretation of the deflections and likely failure modes in the material (Bogetti et al., 1995).

This study therefore focuses on finding the effective material properties rather than composites properties[3]. Section 4.3 presents solutions to the elastic characterisation problem and Section 4.4 presents solutions to the strength characterisation problem.

4.2 Coordinate Conventions

The coordinate conventions used in this section are shown in Figure 4.1.

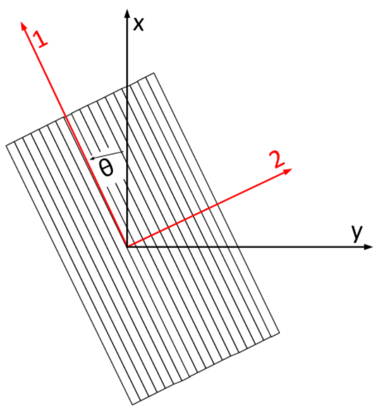

Figure 4.1: Coordinate conventions used in this investigation.

Material coordinate 1 refers to the fibre axis of the material; 2 refers to the transverse axis; 3 (out of plane) refers to the thickness transverse axis. x is the direction of the applied tensile load; y is the direction normal to this axis; z (out of plane) is the thickness direction, equivalent to 3 for a state of plane stress[4]. Equations 4.1–4.5 show the stress transformation into material coordinates for an applied load in the x-direction under plane-stress conditions.

[3]Such as A-B-C-D matricies or similar.

[4]*Plane stress* in this case referring to a 2-dimensional stress state. As the $z(3)$ length is much smaller than the x or y length, the stress in the z direction can be assumed to be zero.

General stress transformation into material coordinates:

$$\begin{Bmatrix} \sigma_1 \\ \sigma_2 \\ \tau_{12} \end{Bmatrix} = \begin{bmatrix} \cos^2\theta & \sin^2\theta & 2\sin\theta\cos\theta \\ \sin^2\theta & \cos^2\theta & -2\sin\theta\cos\theta \\ -\sin\theta\cos\theta & \sin\theta\cos\theta & \cos^2\theta - \sin^2\theta \end{bmatrix} \begin{Bmatrix} \sigma_x \\ \sigma_y \\ \tau_{xy} \end{Bmatrix} \tag{4.1}$$

Where σ_{ij} [MPa] and τ_{ij} [MPa] give the normal and shear stresses respectively. As only uniaxial x-direction stress is applied to tensile specimen:

$$\sigma_y = 0; \tau_{xy} = 0 \tag{4.2}$$

Therefore the stress transformation is simply

$$\sigma_1 = \cos\theta^2\sigma_x \tag{4.3}$$

$$\sigma_2 = \sin\theta^2\sigma_x \tag{4.4}$$

$$\tau_{12} = -\sin\theta\cos\theta\sigma_x \tag{4.5}$$

Composite materials can be analysed on different levels: the *micromechanics* level analyses composites based on the micromechanical interactions of their constituents; the *lamina* level analyses one ‘slice’ of the composite; and the *laminate* level analyses the entire composite as a single solid. Micromechanics-based analyses are usually used when very fine detail is required, and so was thus disregarded for this application as a basic mechanical characterisation was sought. The focus then shifts to attempting to model the effective material as an orthotropic solid.

4.3 Modelling of Elastic Properties

Hooke’s formulation of the stiffness matrix $[C]$ describing the relationship between stress and strain for an anisotropic material is as shown in 4.6.

$$\begin{Bmatrix} \sigma_1 \\ \sigma_2 \\ \sigma_3 \\ \tau_{12} \\ \tau_{23} \\ \tau_{13} \end{Bmatrix} = \begin{bmatrix} C_{11} & C_{12} & C_{13} & C_{14} & C_{15} & C_{16} \\ C_{21} & C_{22} & C_{23} & C_{24} & C_{25} & C_{26} \\ C_{31} & C_{32} & C_{33} & C_{34} & C_{35} & C_{36} \\ C_{41} & C_{42} & C_{43} & C_{44} & C_{45} & C_{46} \\ C_{51} & C_{52} & C_{53} & C_{54} & C_{55} & C_{56} \\ C_{61} & C_{62} & C_{63} & C_{64} & C_{65} & C_{66} \end{bmatrix} \begin{Bmatrix} \epsilon_1 \\ \epsilon_2 \\ \epsilon_3 \\ \gamma_{12} \\ \gamma_{23} \\ \gamma_{13} \end{Bmatrix} \tag{4.6}$$

The material is hereafter assumed to be orthotropic[5]. As an orthotropic material has planes of symmetry along the 1, 2, and 3 axes, the stiffness matrix for loading along the material axes reduces as follows

$$\begin{Bmatrix} \sigma_1 \\ \sigma_2 \\ \sigma_3 \\ \tau_{13} \\ \tau_{23} \\ \tau_{12} \end{Bmatrix} = \begin{bmatrix} C_{11} & C_{12} & C_{13} & 0 & 0 & 0 \\ C_{21} & C_{22} & C_{23} & 0 & 0 & 0 \\ C_{31} & C_{32} & C_{33} & 0 & 0 & 0 \\ 0 & 0 & 0 & C_{44} & 0 & 0 \\ 0 & 0 & 0 & 0 & C_{55} & 0 \\ 0 & 0 & 0 & 0 & 0 & C_{66} \end{bmatrix} \begin{Bmatrix} \epsilon_1 \\ \epsilon_2 \\ \epsilon_3 \\ \gamma_{13} \\ \gamma_{23} \\ \gamma_{12} \end{Bmatrix} \tag{4.7}$$

(Barbero, 2014)

If a plane stress assumption is made, which is valid for the thin tensile testing coupon employed in this experiment[6], stresses σ_3, τ_{13}, τ_{23} and strains ϵ_3, γ_{13}, γ_{23} are taken as zero. The stress-strain relationship for a orthotropic laminate under plane stress then becomes

$$\begin{Bmatrix} \sigma_1 \\ \sigma_2 \\ \tau_{13} \end{Bmatrix} = \begin{bmatrix} C_{11} & C_{12} & 0 \\ C_{21} & C_{22} & 0 \\ 0 & 0 & C_{66} \end{bmatrix} \begin{Bmatrix} \epsilon_1 \\ \epsilon_2 \\ \gamma_{12} \end{Bmatrix} \tag{4.8}$$

(Nettles, 1994) This greatly simplifies the elastic modelling, as only 4 elastic constants[7] are required to specify the elastic behaviour of the laminate rather than the 21 required

[5]This assumption can be validated by examination of the mesostructure under microscope, which shows the uniformity of the material along the 1,2,3 axes.

[6]As the width (25.0 mm) is much greater than the thickness (2.0 mm).

[7]Note that the stiffness matrix is symmetrical.

to specify a thick anisotropic material (Barbero, 2014).

If the loading is not along the material axis, ie. the fibre axis is not parallel or perpendicular to the loading axis, the stress-strain relationship becomes

$$\begin{Bmatrix} \sigma_x \\ \sigma_y \\ \tau_{xy} \end{Bmatrix} = \begin{bmatrix} C_{xx} & C_{xy} & C_{xs} \\ C_{yx} & C_{yy} & C_{ys} \\ C_{sx} & C_{sy} & C_{ss} \end{bmatrix} \begin{Bmatrix} \epsilon_x \\ \epsilon_y \\ \gamma_{xy} \end{Bmatrix} \tag{4.9}$$

where subscript s denotes a shear (1–2) relationship. If the material-axes elastic properties are known, the elastic properties along the tensile axis x for any angle θ can be interpolated as in Equation 4.18.

$$C_{xx} = C_{11} \cos^4 \theta + 2(C_{12} + 2C_{66}) \cos^2 \theta \sin^2 \theta + C_{22} \sin^4 \theta \tag{4.10}$$

(Nettles, 1994).

To model the elastic behaviour of the laminate under tensile loading, the 4 elastic constants (C_1, C_{12}, C_{22} and C_{66}) must be determined. The 'Mechanics of Materials Approach' developed in Renaud et al. (1999) was selected as the focus for this study based on simplicity, however alternative methods are available [8].

4.3.1 Mechanics of Materials Approach

The *mechanics of materials* approach detailed by Renaud et al. (1999) is a feasible approach for simple characterisation as it is solely based on material mesostructure and bulk material properties. The bulk material properties input to the model are the simple elastic properties of the bulk material: Young's modulus[9], Shear modulus[10] and Poisson's Ratio[11].

The mechanics of materials approach characterises the mesostructure by determining a void density ρ that represents the density of air voids (regions not occupied by fibres) for a given plane through the FFF-ABS material (Renaud et al., 1999). The void

[8] See Renaud et al. (1999) for discussion of representative volume element based approaches.
[9] Stiffness of the material; ratio of stress to strain under tensile loading.
[10] Ratio of shear stress to shear strain under shear loading.
[11] Ratio of transverse and axial strains under tensile loading. Poisson's ratio notes how much a specimen will contract in the direction normal to applied tensile loading.

density is assumed to be constant for any plane through the material. The validity of this assumption was confirmed by microscopy of the long-range order of the printed material mesostructure. Classical composite theory (the *model of mixtures*) is then applied to the void-fibre composite in order to determine the effective elastic properties. Full derivation of the mechanics of materials method is not reproduced in this study. The derivation can be found in Li, Sun, Bellehumeur, and Gu (2002) and Renaud et al. (1999). ρ_1 is taken as representing the void density of the plane orthogonal to the fibre axis. Renaud et al. (1999) derived the result that the void density ρ_2 and ρ_3 of the transverse planes are equal to $\sqrt{\rho_1}$. The mechanics of materials approach is shown in equations 4.11–4.16.

$$\bar{E_1} = (1 - \rho_1)E \tag{4.11}$$

$$\bar{E_2} = \bar{E_3} = (1 - \rho_1^{1/2})E \tag{4.12}$$

$$\bar{G_{12}} = \bar{G_{13}} = G\frac{(1 - \rho_1)(1 - \rho_1^{1/2})}{(1 - \rho_1) + (1 - \rho_1^{1/2})} \tag{4.13}$$

$$\bar{G_{23}} = (1 - \rho_1^{1/2})G \tag{4.14}$$

$$\bar{\nu_{12}} = \bar{\nu_{13}} = (1 - \rho_1)\nu \tag{4.15}$$

$$\bar{\nu_{23}} = \bar{\nu_{21}} = \bar{\nu_{31}} = \bar{\nu_{32}} = (1 - \rho_1^{1/2})\nu \tag{4.16}$$

where:

$\bar{E_i}$ represent effective Young's modulus values for 1,2,3 principal directions;

$\bar{\nu_{ij}}$ represent effective Poisson's ratio for 1,2,3 principal directions;

$\bar{G_{ij}}$ represent effective shear modulus for 1,2,3 principal directions and

E, ν, G represent Young's modulus, Poisson's ratio and shear modulus of the bulk material.

The difficulty with this method lies in determining ρ_1, which is determined from image analysis of SEM (Scanning Electron Microscopy) of the printed mesostructure. However, this contravenes the stated aim of the thesis as SEM exceeds the resources available to the typical engineer. The void density can not be assumed to be a constant across all FFF printers, as it is based on the specific mesostructure made by the combination of printer and slicing software (Rodriguez et al., 2000). It was found that an inexpensive USB microscope provided adequate magnification levels for this purpose (approximately 200x), allowing the method to be applied to the research goals[12].

If these predicted laminate properties are substituted into the stiffness matrix [C] (Equation 4.8), the stress-strain matrix becomes

$$\begin{Bmatrix} \sigma_x \\ \sigma_y \\ \tau_{xy} \end{Bmatrix} = \begin{bmatrix} \frac{E_{11}}{1-\nu_{12}\nu_{21}} & \frac{\nu_{12}E_{11}}{1-\nu_{12}\nu_{21}} & 0 \\ \frac{\nu_{12}E_{22}}{1-\nu_{12}\nu_{21}} & \frac{E_{22}}{1-\nu_{12}\nu_{21}} & 0 \\ 0 & 0 & G_{12} \end{bmatrix} \begin{Bmatrix} \epsilon_x \\ \epsilon_y \\ \gamma_{xy} \end{Bmatrix} \tag{4.17}$$

This equivalency is based on composite mechanics theory in Nettles (1994). Substituting properties from the mechanics of materials approach into Equation 4.10, the x-direction elastic modulus for an orientation angle θ can be found as

$$C_{xx} = E_x = E_{11}\cos^4\theta + 2(E_{12} + 2G_{12})\cos^2\theta\sin^2\theta + E_{22}\sin^4\theta \tag{4.18}$$

Only this tensile axis elastic modulus E_x was calculated and compared in this research, as the validity of using this method to predict other elastic properties is shown by Renaud et al. (1999) and project time constraints prevented evaluation of the other material properties. For the purposes of answering the research questions, it was assumed that accurate estimation of the elastic modulus implied the ability to accurately estimate the other elastic constants. The results of this analysis are found in Section 7.1.

4.4 Modelling of Material Strength

Very little research has previously been conducted in the modelling of the strength of FFF material. Renaud et al. (1999) found that strength of a tensile tested laminate corresponded very well to Azzi and Tsai's multiaxial strength theory, in which the yield condition is assumed to be quadratic in the stress components. The theory predicts that a failure occurs when Equation 4.19 is satisfied (Azzi and Tsai, 1968):

[12] An alternative solution to mesostructure microscopy altogether is to estimate the void density based on measurements of a test print of known geometry, in which case the void density would be the 'bounding box' area (see Glossary) of the specimen minus the area of the material deposited (taken from the slicing software).

$$K_1(\sigma_y - \sigma_z)^2 + K_2(\sigma_z - \sigma_x)^2 + K_3(\sigma_x - \sigma_z)^2 + 2K_4\tau_{yz}^2 + 2K_5\tau_{zx}^2 + 2K_6\tau_{xy}^2 = 1 \quad (4.19)$$

where K_i are experimentally determined material coefficients. To avoid determining these material coefficients, however, an alternative derivation is proposed based on the 'interaction formula' as described by Norris (1962). This derivation is presented in Appendix B. The multiaxial strength theory is thus described as:

$$(\frac{1}{S_1^2})\sigma_x^2 \cos^4\theta + (\frac{1}{S_{12}^2} - \frac{1}{S_1^2})\sigma_x^2 \cos^2\theta \sin^2\theta + (\frac{1}{S_2^2})\sigma_x^2 \cos^4\theta = 1 \quad (4.20)$$

Failure occurs when this equation is satisfied. To characterise the strength of the tensile coupon at an arbitrary angle θ a method must therefore be established to determine the strength values S_1 (fibre-axis tensile strength), S_2 (transverse tensile strength) and S_{12} (intralaminar shear strength[13]). This study developed methods to estimate these strengths. These methods are established in the following sections.

4.4.1 Longitudinal Tensile Strength

Given a unidirectional laminate, the total fibre cross-sectional area A_f can be found from the definition of the void density ρ_1:

$$A_f = A - A_{void} = A - A\rho_1 = A(1 - \rho_1) \quad (4.21)$$

If the assumptions are made that all fibres carry the tensile load in simple axial tension (ie. coupling effects under fibre-axis tensile loading are insignificant) and each fibre experiences the same elongation[14], then the tensile failure load is simply

$$F = A_f S_{ty} \quad (4.22)$$

which gives an effective longitudinal tensile strength S_1 from the stress definition

[13]Or fibre-bond shear strength

[14]Which is valid before failure of the material, as differing elongation between fibres will cause failure by fibre pull-out.

$$S_1 = \frac{F}{A} = \frac{A_f S_{ty}}{A} = \frac{(1-\rho_1)AS_{ty}}{A} = (1-\rho_1)S_{ty} \tag{4.23}$$

This relationship was originally derived in the investigation from stress analysis of the summation of the area of each fibre. It was later discovered that Jose F. Rodriguez (2001) independently determined a similar method. The equivalent void density form of the equation is presented here as it is more elegant. It should be noted that this relationship assumes there are no molecular orientation effects during extrusion; further discussion on this subject is presented in Section 7.4.1.

4.4.2 Intralaminar Shear Strength

No previous research has attempted prediction of the interfibre shear strength of the FFF composite. Renaud et al. (1999) estimated the intralaminar shear strength of a FFF-ABS composite from tensile testing results by applying the multiaxial strength formula (Equation 4.20). This is simply applying an interpolation function applied to existing data, however – it can not be used to predict the shear strength of a different FFF-ABS laminate.

No data is available on the shear strength of PA-747 ABS material (or even the more common P400 grade). The shear yield strength can however be estimated from the tensile yield strength. The tensile load required to cause yielding is approximately 31.0 MPa (Chi-Mei-Corporation, 2006). As quoted tensile yield strengths are simply the uniaxial tensile stress required to cause yield, this value can be transformed as per Equation 4.5 to find the shear stress present at this point:

$$\tau_{xy} = -\sin\theta\cos\theta\ S_{ty} \tag{4.24}$$

Which reaches it's maximum at $\theta = 45°$:

$$\tau_{xy} = \frac{S_{ty}}{2} = 15.5MPa \tag{4.25}$$

If the Tresca yield criterion is used[15], this failure shear stress becomes a good

[15] Which states that a material will yield if the maximum shear stress present exceeds the shear yield strength

approximation to the shear yield strength of the material. If the composite is loaded in pure interfibre shear, all loading will be carried through the interfibre bonds. We thus imagine a hypothetical fibre interface surface subjected solely to shear loading. Given ρ_2, the void density in this bonding plane, we can find the effective transverse bond area A_{f2}. Figure 4.2 shows a graphical representation of this effective area.

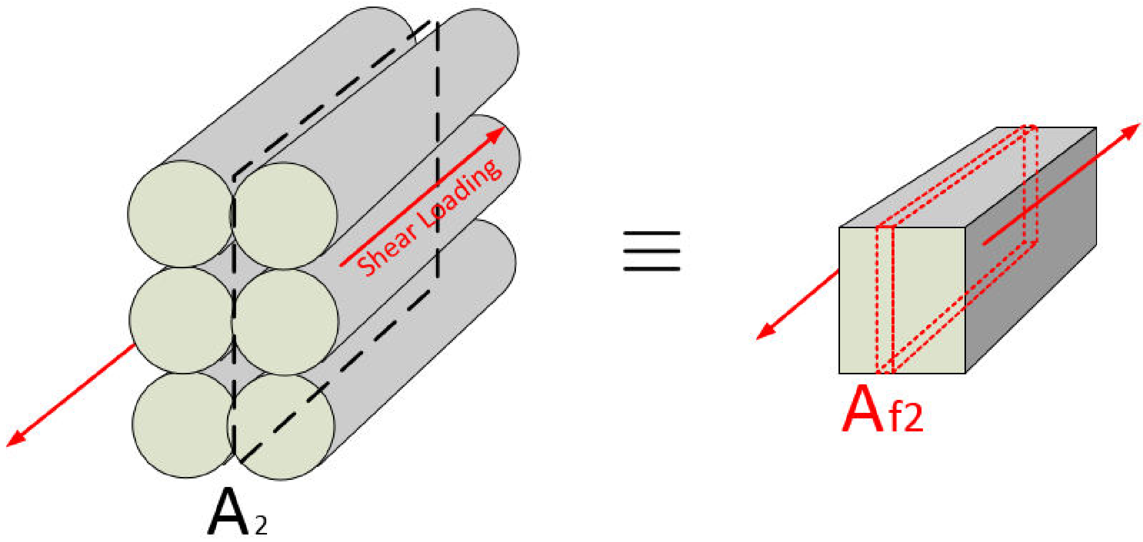

Figure 4.2: Illustration of the shear-load carrying area.

This shear-load carrying area can be calculated as

$$A_{f2} = A_2(1 - \rho_2) \tag{4.26}$$

The shear stress required to cause yield is given by the Tresca yield criterion as

$$\tau_{xy} = S_{sy}A_{f2} \tag{4.27}$$

As the interfibre shear strength S_{12} is the shear strength of the total laminate, it is associated with the total area A. This is equated to the shear stress at failure τ_{xy} to give

$$S_{sy}A_{f2} = S_{12}A \tag{4.28}$$

Substituting Equation 4.26 gives

$$S_{12}A = S_{sy}A(1 - \rho_2) = \frac{S_{ty}}{2}A(1 - \rho_2) \tag{4.29}$$

As noted by Renaud et al. (1999), the bond void density ρ_2 is equivalent to $\sqrt{\rho_1}$. The interfibre shear strength S_{12} simplifies to

$$S_{12} = \frac{S_{ty}}{2}(1 - \sqrt{\rho_1}) \tag{4.30}$$

It should be noted that this value is an estimate, and assumes that the shear yield strength is equal to $\frac{1}{2}$ the tensile yield strength; that the post-extrusion fibre tensile strength is equivalent to the bulk material tensile strength; that stress concentrations are not significant in the fibre shearing mode; and that the bonding length ratio is constant across the mesostructure. Section 7.1 compares this estimate to experimental values.

4.4.3 Transverse Tensile Strength

It was observed that the FFF-ABS material failed in a brittle fracture mode when loaded in transverse tension. Brittle fracture initiated at the fibre surface cavity on the edge of the tensile specimen and grew across the specimen quickly, causing ultimate failure of the coupon. This signifies that linear-elastic fracture mechanics (LEFM) theory can likely be applied to predict the transverse tensile strength.

Attempts were made to model the transverse fracture of the specimen as occuring via growth of the surface fibre voids on the edge of the tensile coupon. A vertical bond length fraction b_3 is defined as shown in Figure 4.3.

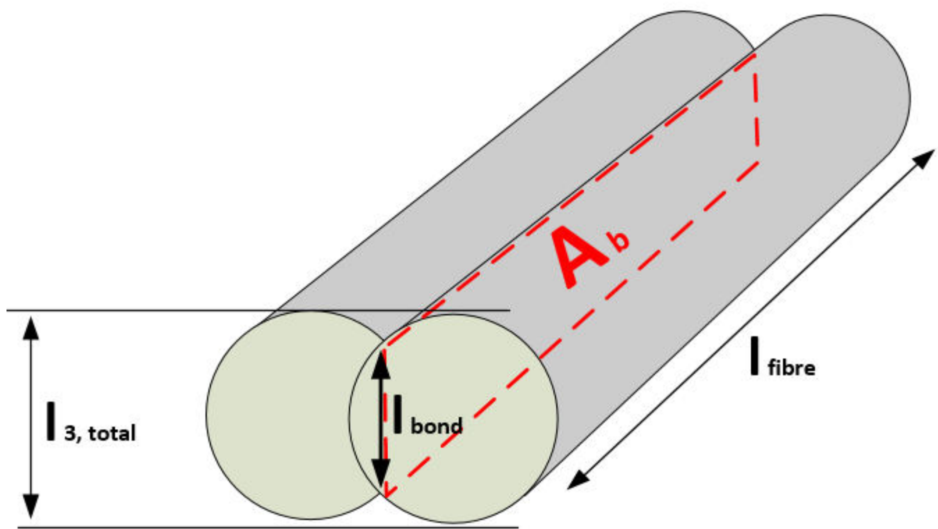

Figure 4.3: Illustration of vertical bond length fraction b_3.

This bond length fraction is given by the equation

$$b_3 = \frac{l_{bond,3}}{l_{total,3}} \tag{4.31}$$

If the surface cavity is taken as the initiating crack, the crack length a is therefore geometrically related to the vertical bond length fraction b_3:

$$a = \frac{b_3 d}{2} \tag{4.32}$$

where d is the fibre diameter. For LEFM theory to be valid, three 'rule of thumb' criteria must be satisfied (Gates, 2014):

- Crack length a must be larger than 50 times the plastic zone radius r_p. r_p can be determined by the
- Crack length a must be larger than $2.5(\frac{K_{Ic}}{\sigma_{ty}})^2$ where K_{Ic} is the material fracture strength.
- Applied stress must be less than 35% of the yield strength.

The first two criteria were failed by a factor of approximately 50; the third criteria was close to failing. LEFM theory is therefore invalid to characterise the transverse tensile strength[16]. Usually in this case Elastic-Plastic Fracture Mechanics (EPFM) theory would be applied to the problem to allow characterisation of the material response in the plastic zone. However, as EPFM data for ABS PA-747 was not available, an alternative strength approximation was formulated.

As Figure 4.3 shows, applied transverse tensile loading will be carried through the inter-fibre bonding area. The transverse strength was therefore estimated by performing a simple yield analysis on the effective bond area A_b. A_b is related to the horizontal bond length fraction as

$$A_b = b_3 \times l_{3,total} \times l_{fibre} \tag{4.33}$$

[16]LEFM characterisation was initially attempted to roughly estimate the transverse strength; however difficulties arise as the fracture plane must be predicted. The effective crack length may also be different to the geometrical relationship given above. It is not recommended to pursue this avenue in future research, as it contradicts the stated 'simple characterisation' goal of research.

where l_3 is the vertical length of the part geometry and l_{fibre} is the length of the fibre. As all tensile loading must be carried through the interfibre bonding area, the effective load-carrying area is A_b. The tensile load F_t to cause yield in the material is therefore

$$F_t = S_{ty} A_b \tag{4.34}$$

The effective transverse strength of the material is then given by the stress definition as

$$S_2 = \frac{F_t}{A} = \frac{S_{ty} A_b}{A} = \frac{S_{ty} b_3 l_{fibre} l_{3,total}}{l_{fibre} l_{3,total}} \tag{4.35}$$

which simplifies to give

$$S_2 = S_{ty} b_3 \tag{4.36}$$

The transverse tensile strength and the interfibre shear strength rely on estimating the effective interfibre bond area, though use mesostructural measures. This is due to the nature of the failure modes: transverse failures result in fracture along the minimum bond areas, which necessitates a minimum area approach; shear failures occur in a ductile mode, in which the 'smearing' nature of the plastic flow suggests an average transverse fibre area approach. It should be again stated that these strength predictions are estimates, and assume a negligible effect from stress concentrators and a constant mesostructure. These strength predictions result in simple but quite accurate characterisations. Section 7.1 compares these predictions to actual experimental testing.

5: Experimental Design

The experimental design was itself a major component of the study, as the manufacturing method can be adjusted greatly and testing procedures for composite materials are far from standardised. Section 3 presents research outlining the factors influencing the mechanical properties of the final part. Table 5.1 shows the set values of these factors used in the study. Two rounds of experimental testing took place, with the second test round incorporating adjustments to solve faults with the first.

Table 5.1: Summary of design parameters.

Slicing Parameters	
Layer Height	0.4 mm
Air Gap	–0.04 mm (10% of Layer Height)
Infill	Unidirectional rectilinear infill
Raster Orientation	Variable $\theta = 0, 10, 45, 60, 90$
Aligned/Skewed Mesostructure	Aligned mesostructure
Bulk Material Properties	
Bulk Material	ABS PA-747
Bulk Material Tensile Yield Strength	31.0 MPa
Material condition	New, stored with dessicant
Material Source	Chi-Mei Corporation
Material Colour	Natural (no composition-altering colourants)
Extrusion Parameters	
Printer Design	Solidoodle 3
Extrusion Speed	2700 mm/min
Gantry Speed	2700 mm/min
Extruder Temperature	210° C
Envelope Temperature	70° C
Post-Fabrication Heat Treatment	T=125° C. Test 1=0,30,90 minutes/Test 2=0,120 minutes annealing time
Design Parameters	
Coupon Standard	ASTM D3039 'Standard for Tensile Properties of Polymer Matrix Composite Materials' (ASTM-International, n.d.)
Coupon Design Length (x direction)	185 mm
Coupon Design Width (y direction)	25.0 mm
Coupon Actual Width (y direction)	Test 1=24.5–25.7 mm;Test 2=25.8–26.2 mm
Coupon Design Thickness (z direction)	2.0 mm
Coupon Actual Thickness (z direction)	Test 1=1.86–2.11 mm;Test 2=2.46 mm

5.1 G-Code Generator

A major part of the investigation was spent developing a precise test specimen slicer that would allow fabrication using desired air gap and extrusion parameters. Conventional slicing programs[1] are designed to be as simple to use as possible, and thus automatically determine the printer pathing. This lead to incorrectly pathed test specimens being produced; as precise control over the printer pathing was needed, a G-code generator was programmed.

This generator, referred to as 'OGCode', is attached in Appendix A. The code is presented as it helps to illustrate the slicing process, which is one of the main influences on the mechanical characteristics of the final part.

For fabrication of the test coupon, OGCode's `block` function is called with dimensions as shown in Table 5.1. The OGCode slicer then generates the printer pathing as follows:

- Layer height is found by `layer height = fibre diameter + vertical air gap`.
- Vertical slice count is then `coupon height` ÷ `layer height`.
- The pathing is then generated slice-by-slice, with each slice increasing the printer head height by `layer height`.
- The `theta`, `width` and `length` parameters[2] are then used to generate a line of points along the boundary of the block corresponding to the end of each fibre.
- OGCode then constructs a `G1` ('extrude and move') command for each of these points, in effect 'connecting the dots'.
- The filament feed driver then pushes `dE` mm filament per mm of movement into the feed chamber; `dE` is found by `area of filament` ÷ `area of desired fibre`.
- The `E` value (feed driver movement) is then found as `dE` × `extrude-move distance`. This value is concatenated to the `G1` command.

[1] such as 'slic3r' or 'skeinforge'
[2] `theta` denotes raster orientation

This generates a 'unidirectional rectilinear' pathing for the specimen, in which parallel fibres are deposited in straight-line movements. This is illustrated in Figure 3.6. The first tensile test used an airgap parameter of 0.0 mm, which was found to produce slightly inconsistent mesostructure. This can be seen in the measured actual dimensions for the first test in Table 5.1. The –0.04 mm air gap was found to be the most consistent through test printing and mesostructure microscopy.

The pather also illustrates the reason for the discrepancy between coupon design dimensions and actual dimensions in the second test: as the design thickness (2.0 mm) divided by the layer height (including air gap) is not an integer number, the OGCode slicer rounds the slice count up to the nearest value, producing the observed coupon width and thickness.

5.2 Method

5.2.1 Fabrication Method

A Solidoodle 3 printer was used to produce the test specimens. An aftermarket glass build plate was installed on the device, though this is in line with manufacturers recommendations. The fabrication method is outlined below:

- Filament kept in airtight container with desiccant sachets prior to use; kept in plastic bag with desiccant sachets during use.
- Filament measured at 10 locations along the cord to find the average filament diameter[3].
- Printer calibrated as per manufacturers recommendations[4], print bed levelled and filament loaded.
- 'ABS Glue'[5] painted in a thin layer on to print bed to ensure specimen-bed adhesion.
- Solidoodle control software 'Repetier-Host' initialised, printer interfaced with computer.

[3]Used in OGCode extrusion amount calculations as described previously.
[4]Calibration procedure is not described here as it is very machine-specific.
[5]A slurry of ABS plastic and acetone. If painted onto a surface, the acetone will evaporate, leaving a thin plastic coating. The glue was left to evaporate on the heated bed for 3–5 mins in the study.

- Print bed heated to 70°C, ABS glue allowed to dry.
- Extruder head heated to 210°C. Extrusion chamber pressure allowed to reach approximately ambient pressure by waiting for excess material to 'ooze' from nozzle.
- OGCode g-code loaded into control software.
- Control software relays g-code to printer, fabricating the part.
- Print bed heating is turned off, allowing component to reach ambient temperature.
- After ambient temperature is reached, component is carefully removed.

5.2.2 Heat Treatment Method

Some test specimens were heat-treated to investigate the effects of reptation on the inter-fibre bond strength. The specimens were heat treated in a conventional oven due to the lack of resources. Conventional ovens operate using a 'bang-bang' controller, in which the temperature is regulated by applying current to the heating element when a lower temperature bound is reached, and stopping the current when an upper temperature bound is reached. This caused the actual heat-treatment temperature to oscillate between 117°C–130°C. This does not invalidate the results, however, as the heat treatment component of the investigation is intended to demonstrate transverse strength increase with annealing rather than find precise values for the strength increase. The heat treatment was conducted as follows:

- A digital thermometer is used to 'tune' the oven bang-bang to the approximate temperature range.
- Specimens are laid flat between alfoil sheets, with two sheets below the specimens and two sheets above.
- The alfoil sheets are then placed atop a flat plate.
- Another flat plate is placed on top of this, each plate weighing approximately 700g.

- The digital thermometer probe is inserted into this assembly to measure the actual temperature the specimens are exposed to[6].
- The assembly is placed in the oven for the desired time.
- The oven is opened and the assembly is allowed to cool to room temperature.
- The test coupons are then removed from the sandwich assembly and placed in sealed, moisture-proof plastic bags.

It is important that the specimens cool evenly. As discussed in Section 3.4.3, an uneven temperature distribution will result in uneven thermal expansion/contraction, leading to residual stresses forming in the material. A reasonably even temperature distribution can be achieved by leaving the assembly structure in place during cooling.

5.2.3 Tensile Testing Method

The first round of tensile testing was performed on an Intron 5584 load frame; the second round was performed on an Instron 5500R. Both tests were performed to ASTM D3039 standard using a 5 kN load cell and an Instron 2620-601 extensiometer with a 25 mm gage length. Specimens had 100 mm of gage length between the jaws. Figure 5.1 shows the tensile testing apparatus used in the second experiment.

The first tensile testing was done using emery cloth tabs as a buffer between the specimen and the dimpled jaw grips. This was found to have caused a large amount of jaw breaks. Hydraulic jaws set at 200PSI were used to clamp the specimens in the second test, and the jaw break rate was found to decrease. The decrease in jaw breaks could however be due to the lower tensile loading required to break the second round of specimens[7].

The tensile testing method is described as follows:

- Thickness and Width of the specimen measured using generic vernier calipers (± 0.02 mm).
- Coupon placed in hydraulic grip, grip actuated to clamp specimen at 200PSI.
- Extensiometer pin placed in to zero gage length.

[6] In comparison to the oven air temperature, which fluctates more than the heat-treatment assembly temperature.

[7] As the second round tested specimens at larger raster orientation angles.

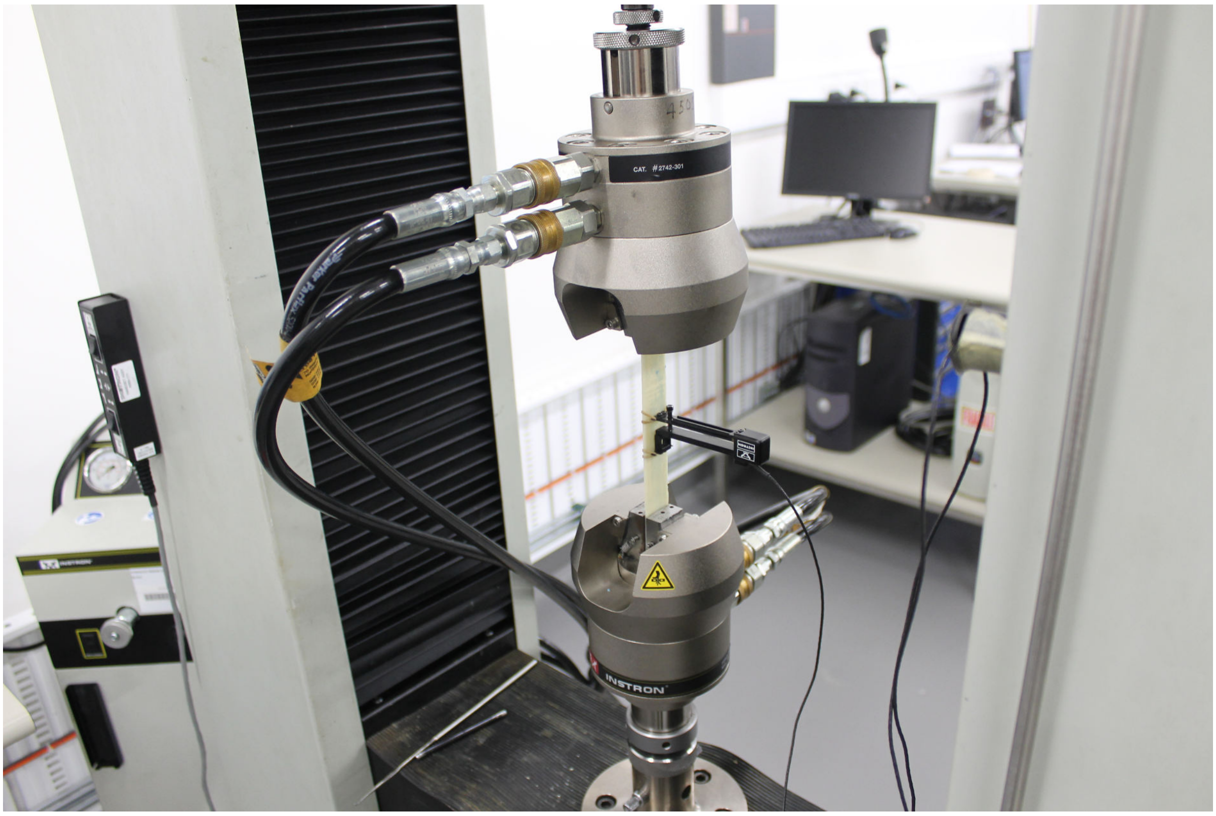

Figure 5.1: Instron 5500R load frame used in the second tensile testing round.

- Extensiometer attached to specimens using rubber bands around extensiometer band hooks.

- 'Balance all' balancing function run on Bluehill software.

- Extensiometer pin removed and test started. Load frame automatically re-zeroed.

- Post-failure coupon removed and load frame returned to original position.

Further information on the issues encountered in the tensile testing can be found in Section 7.4.2.

5.2.4 Mesostructural Analysis Method

The void density ρ_1 was experimentally determined based on image analysis of mesostructure microscopy. Representative specimens were produced then cut normal to the fibre axis with a hacksaw. 600 grit sandpaper was then loaded into an orbital sander and the specimen face sanded flat. 1200 grit sandpaper was then used to finish the specimens. Isopropyl alcohol was then sprayed onto the cross-section face to remove any sandpaper debris or grit.

A 'plugable USB microscope' was used for image capture. The image was then loaded into ImageJ image analysis software. The image was then converted to binary form, in which black pixels correspond to air voids and white pixels correspond to ABS fibre. An 'ImageJ measure' was then taken of a representative sample of voids, which counts the black pixels to find the total void area. This void area divided by the sample area gives the void density ρ_1. Figure 5.2 shows this process being applied to mesostructure microscopy produced by Jose F. Rodriguez (2001) to calculate the void density ρ_1 and the horizontal bond length b_3.

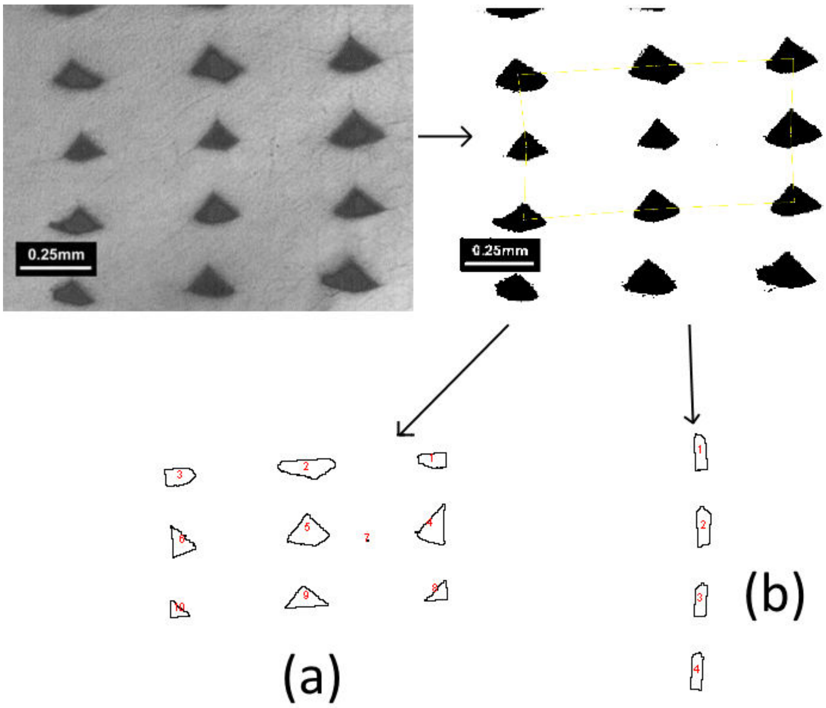

Figure 5.2: ImageJ (a) Void density estimation (b) Bond length estimation.

6: Results

6.1 Tensile Test 1

The first tensile test loaded specimens shown in Table 6.1.

Table 6.1: Tensile test 1 specimens.

ID	Orientation	Air Gap [mm]	Anneal Time [mins]	Sample Count
A	$\theta = 0°$	0	$t = 0$	3
B		0	$t = 30$	3
C		0	$t = 90$	3
D	$\theta = 10°$	0	$t = 0$	3
E		0	$t = 30$	3
F		0	$t = 90$	3
G	$\theta = 90°$	0	$t = 0$	3
H		0	$t = 30$	3
I		0	$t = 90$	3

The mesostructural microscopy of the representative test coupon is shown in Figure 6.1.

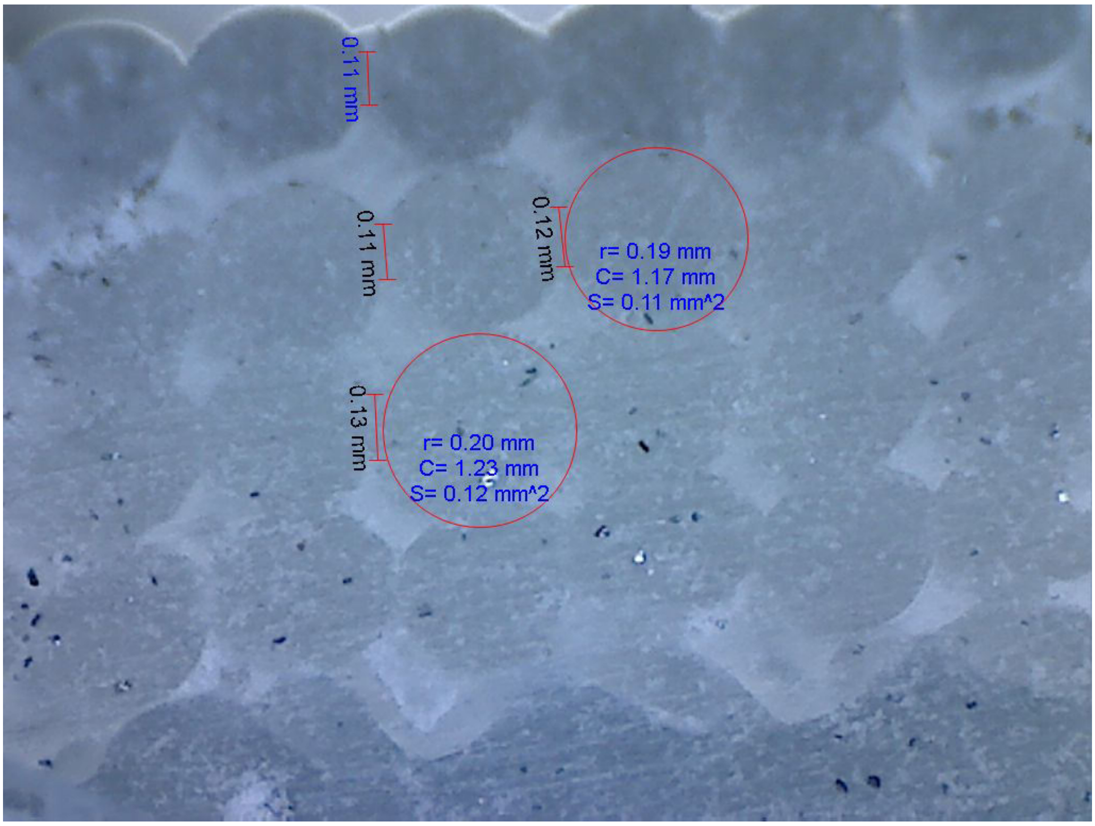

Figure 6.1: Representative mesostructure of first set of tensile testing coupons.

Image analysis of the representative mesostructure gave an average void density of ρ_1 of 0.2198 and a horizontal bond length b_3 of 0.358 over 5 analyses.

Some issues arose during the testing process. Very few of the specimens broke within the gage length[1]. Rupture for the 'non gage break' specimens usually initiated at the jaw edge. This does not invalidate the testing according to ASTM Standard D3039, however data "should be used with caution as this data may not be representative of the material. Failure in the grip region indicates that the stress concentration at the tab is greater than the natural strength variation of the material in the gage section." (ASTM-International, n.d.). The results for the tensile testing should therefore be interpreted as underestimating the actual mechanical strength. It is however probable that the stress/strain data are close to the true values as the data are similar to results found by Ahn et al. (2002), Ziemian et al. (2012), Sood et al. (2009) and Tymrak et al. (2014). See 7.4.2 for a discussion on recommended future improvements to the testing process.

6.1.1 $\theta = 0°$ Test Results

The $\theta = 0°$ tensile test data is shown in Figure 6.2.

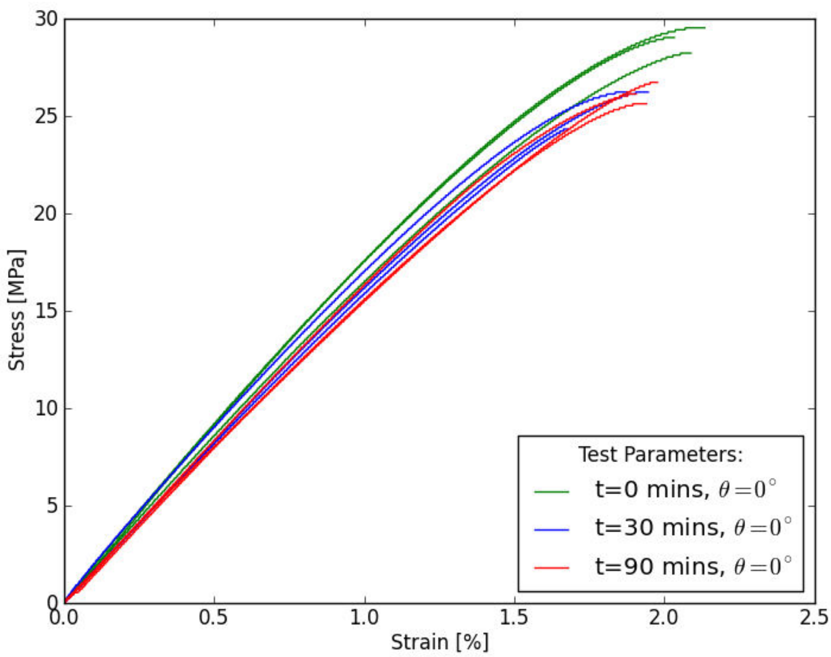

Figure 6.2: Tensile test data for $\theta = 0°$ case.

[1]Gage length represents the region of the specimen which a break is desirable; as a break near the gripping jaws will usually indicate some distortion of the results by the compressive forces of the jaws.

The linear elastic nature of the composite in longitudinal loading can be seen from the stress-strain curve. It can also be observed that the annealing process did not have a significant effect on the elastic modulus of the composite, but may have slightly reduced the tensile strength. Further testing would be needed to evaluate this effect properly, as the sample size was very small.

6.1.2 $\theta = 10°$ Test Results

The $\theta = 10°$ tensile test case showed extremely similar results to the $\theta = 0°$ case. The $\theta = 10°$ tensile test data is shown in Figure 6.3.

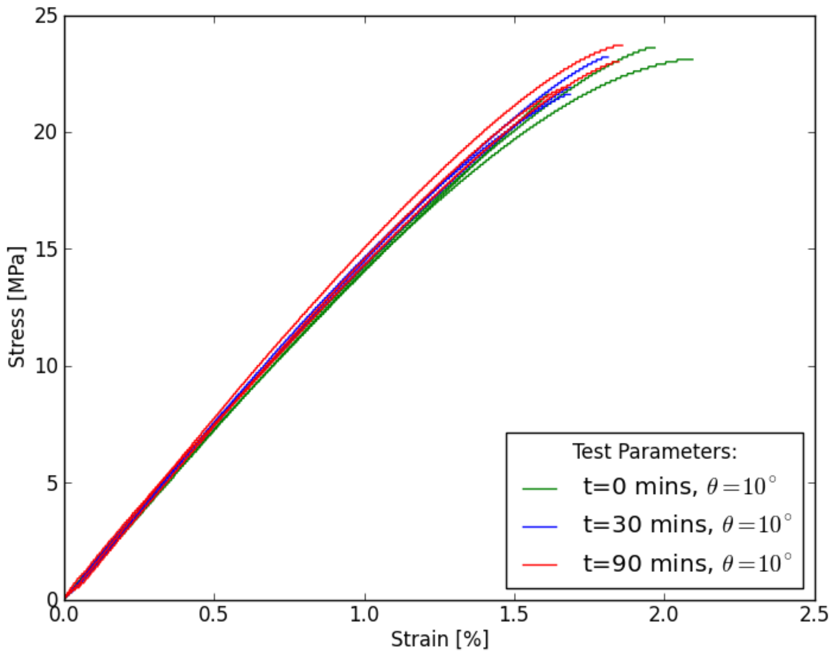

Figure 6.3: Tensile test data for $\theta = 10°$ case.

This similarity is due to the close raster orientations of the two experiments. The $\theta = 10°$ test was performed in an attempt to estimate the interfibre shear strength S_{12}. The test is recommended in prior research by Renaud et al. (1999). It was found to be unsuitable for this purpose, however. Reasons for this are discussed in Section 7.4.3.

6.1.3 $\theta = 90°$ Test Results

A zero air-gap was specified for the first tensile test in the slicing parameters. It is theorised that the zero air-gap did not force the extruding fibre onto the deposited material adequately, which led to fibres being slightly misaligned. This had two negative effects. The coupon dimensions were quite variable – thickness ranged from 1.86–2.11 mm and width varied from 24.5–25.7 mm. This variation was most pronounced in the $\theta = 90°$ case. The zero air-gap also led to extremely poor interfibre bonding, which caused the very low failure load for the $\theta = 90°$ case.

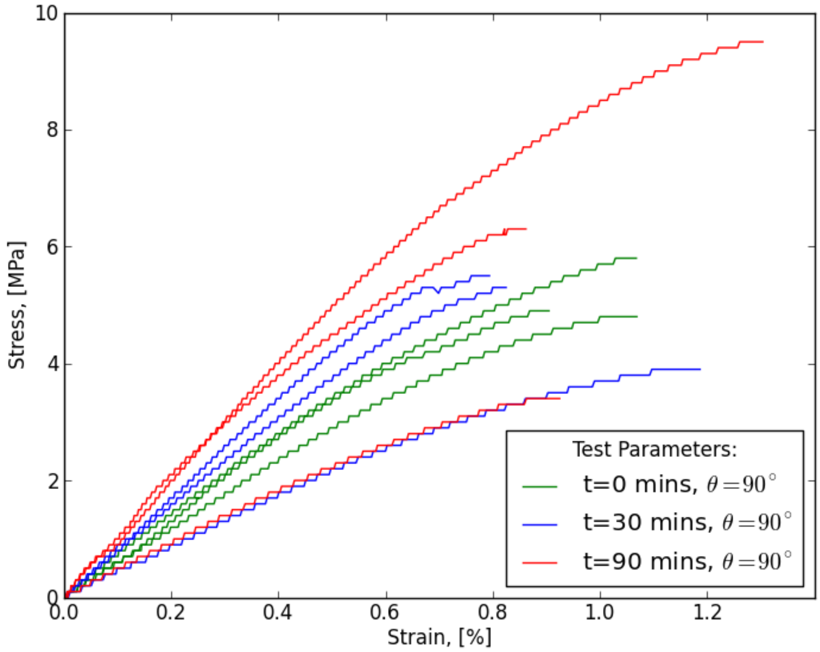

Figure 6.4: Tensile test data for $\theta = 90°$ case.

As shown in Figure 6.4, there were also stress fluctuations at the start of the test. As the grip extension increases, there are regions where the load plateaus, as shown in Figure 6.5[2].

[2]The graph is shown in load-extension rather than stress-strain as the fluctuations are more apparent.

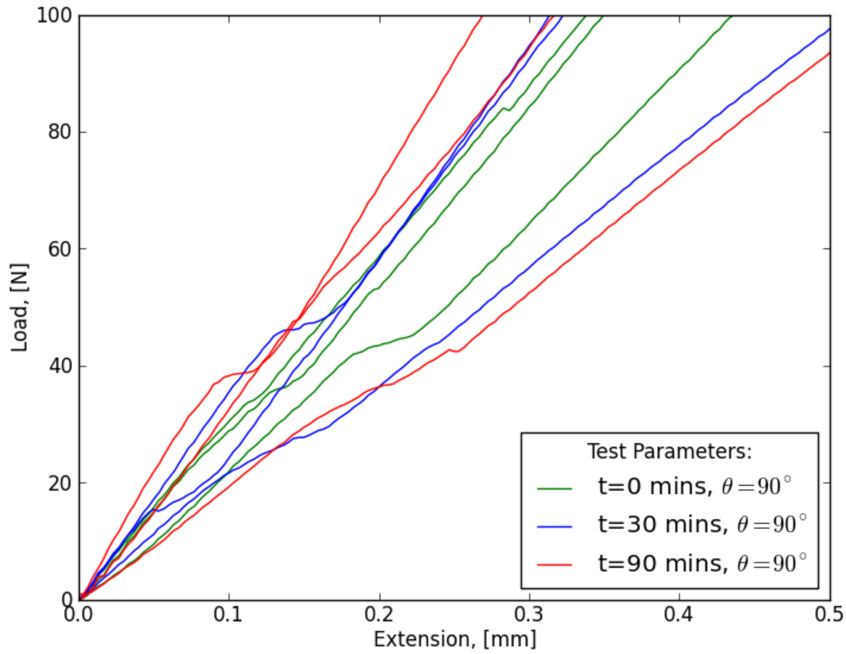

Figure 6.5: Stress fluctuations observed in the $\theta = 90°$ load case.

It is theorised that these fluctuations were present due to the localised yielding in the inconsistent mesostructure produced by the zero air-gap. As the bonding is inconsistent, some fibre bonds will fracture before others, temporarily relaxing the stress in the specimen as the specimen separates to take up the extended gage length. This therefore invalidates the results of the test and demonstrates that a zero air-gap leads to extremely poor interfibre bonding.

A second tensile test was performed with a –0.04 mm air gap. The results for this case are found in Section 6.2.

6.2 Tensile Test 2

The second tensile test loaded specimens shown in Table 6.2.

Table 6.2: Tensile test 2 specimens.

ID	Raster Orientation	Air Gap [mm]	Anneal Time [mins]	Sample Count
N45	$\theta = 45°$	–0.04	$t = 0$	3
T45		–0.04	$t = 120$	3
N60	$\theta = 60°$	–0.04	$t = 0$	3
T60		–0.04	$t = 120$	3
N90	$\theta = 90°$	–0.04	$t = 0$	5
T90		–0.04	$t = 120$	4

The mesostructural microscopy of the representative test coupon is shown in Figure 6.6.

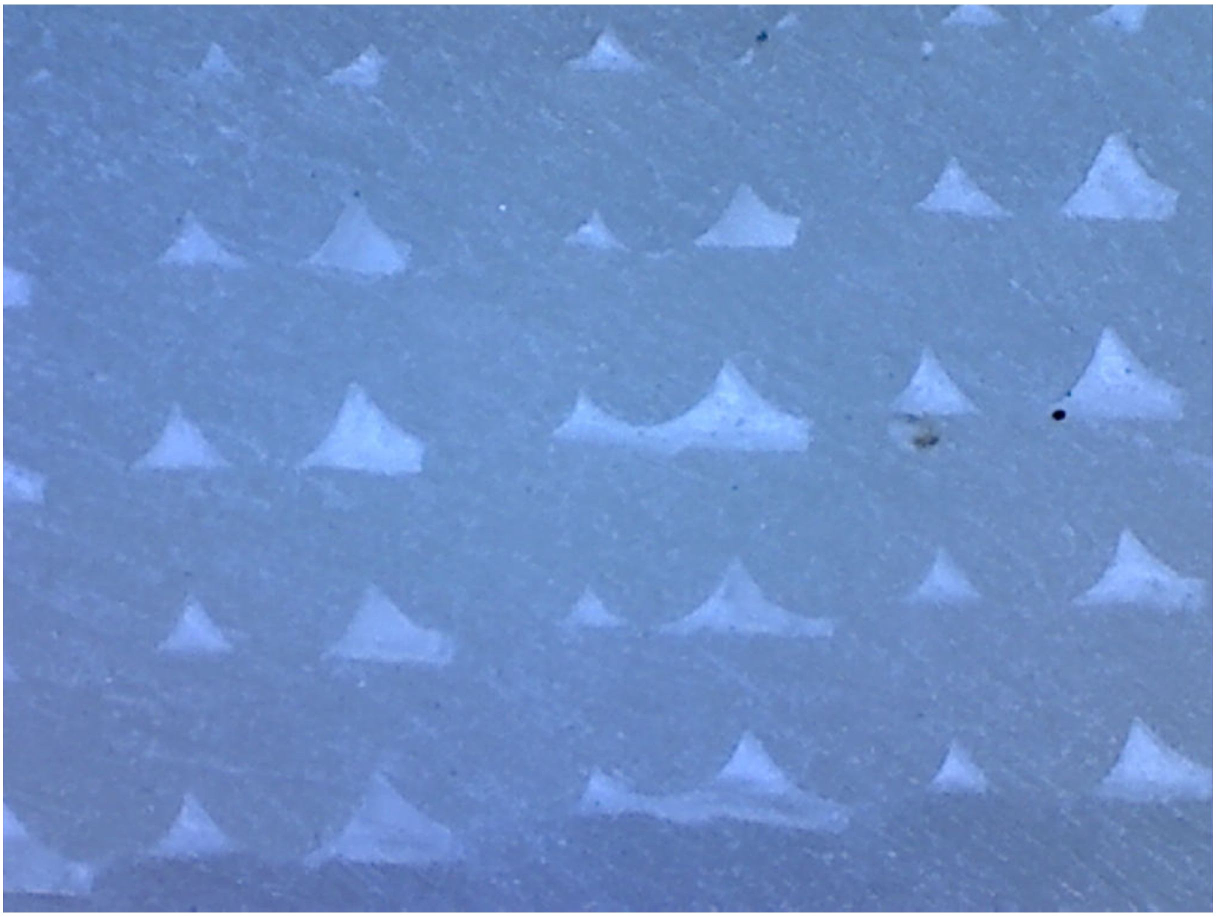

Figure 6.6: Representative mesostructure of second set of tensile testing coupons.

Image analysis of the representative mesostructure gave an average void density of ρ_1 of 0.0909 and a horizontal bond length b_3 of 0.594 over 5 analyses.

6.2.1 $\theta = 45^\circ$ Test Results

The $\theta = 45$ tensile test data is shown in Figure 6.7.

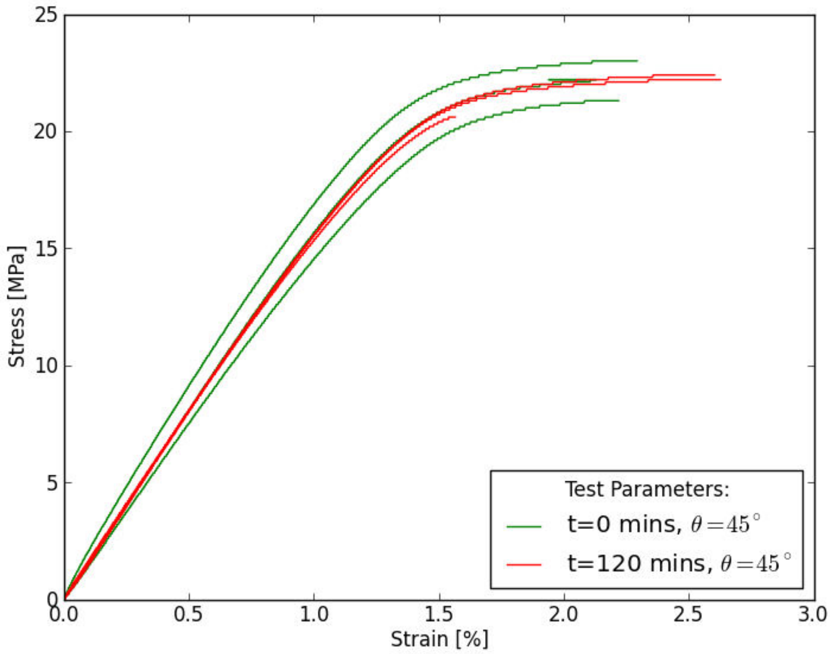

Figure 6.7: Tensile test data for $\theta = 45^\circ$ case.

6.2.2 $\theta = 60^\circ$ Test Results

The $\theta = 60$ tensile test data is shown in Figure 6.8.

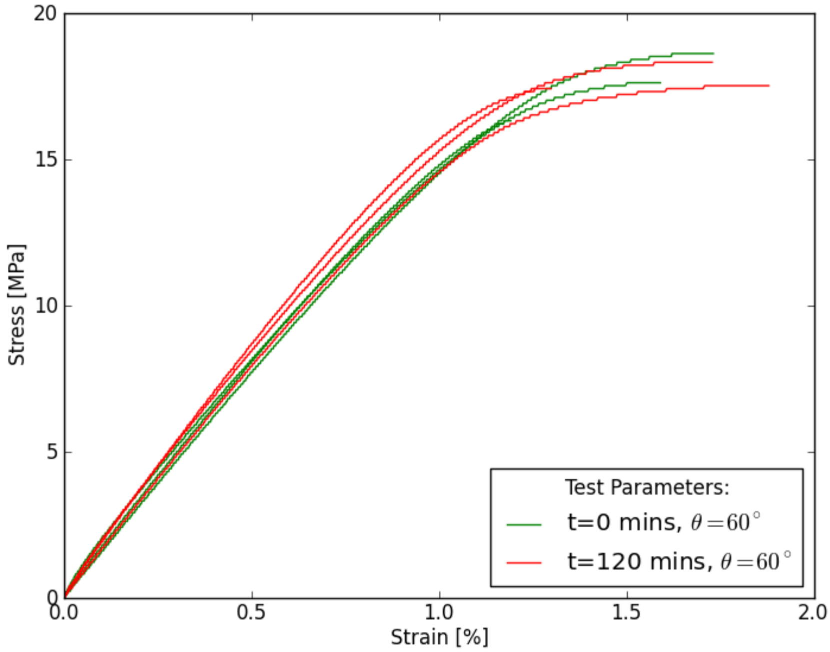

Figure 6.8: Tensile test data for $\theta = 60^\circ$ case.

6.2.3 $\theta = 90^\circ$ Test Results

The $\theta = 90$ tensile test data is shown in Figure 6.9.

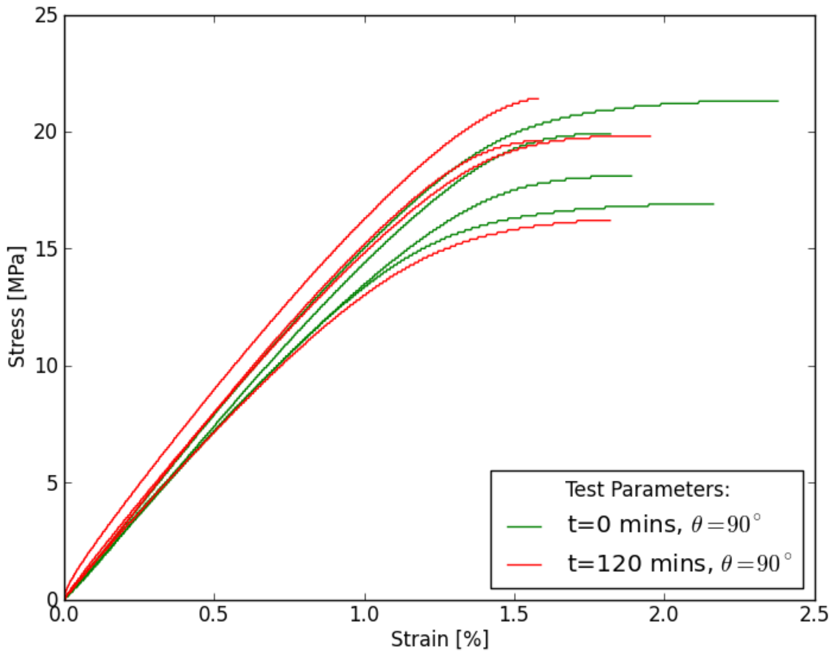

Figure 6.9: Tensile test data for $\theta = 90^\circ$ case.

Of particular note is the large strength increase when compared to the zero air gap $\theta = 90°$ case.

6.3 Experimental Mechanical Properties

The mechanical properties derived from the experimental data are shown in Table 6.3. Due to the insignificant effect of the heat-treatment, specimen data is also presented as grouped for constant raster orientation/air gap. These groups are denoted with *.

Table 6.3: Mechanical properties derived from experimental tensile tests.

ID	θ	**Air Gap, [mm]**	**Anneal Time, [mins]**	**Avg. Strength ± Std. Dev., [MPa]**	**Avg. Elastic Modulus ± Std. Dev., [MPa]**
ABC*	0	0		26.97 ± 1.6	1655.73 ± 73.22
A	0	0	0	29.0 ± 0.54	
B	0	0	90	25.67 ± 0.9	
C	0	0	30	26.23 ± 0.45	
DEF*	10	0		22.72 ± 0.81	1451.27 ± 28.95
D	10	0	0	22.87 ± 0.85	
E	10	0	30	22.33 ± 0.69	
F	10	0	90	22.97 ± 0.74	
45N&T*	45	–0.04		22.05 ± 0.78	1593.48 ± 78.92
45N	45	–0.04	0	22.27 ± 0.69	
45T	45	–0.04	120	21.83 ± 0.81	
60N&T*	60	–0.04		17.72 ± 0.73	1585.22 ± 60.6
60N	60	–0.04	0	17.6 ± 0.94	
60T	60	–0.04	120	17.83 ± 0.4	
GHI*	90	0		5.59 ± 1.65	716.23 ± 188.12
G	90	0	0	5.27 ± 0.45	
H	90	0	30	5.0 ± 0.71	
I	90	0	90	6.5 ± 2.49	
90N&T*	90	–0.04		18.9 ± 1.96	1515.74 ± 124.22
90N	90	–0.04	0	18.54 ± 1.94	
90T	90	–0.04	120	19.35 ± 1.89	

7: Discussion

7.1 Comparison of Results

Models developed in Section 4 were used to predict the theoretical mechanical properties. These estimates are contrasted with the experimental data to evaluate the accuracy of the model. As the void density ρ_1, bond length b_3 and coupon cross-section dimensions l_y and l_z changed between tests, two sets of calculations were performed. Table 7.1 and Table 7.2 presents the predicted material properties and their comparison with the experimental results for tensile test 1 and 2 respectively.

Table 7.1: Comparison of theoretical predictions and experimental results, test 1.

Property	**Theo. Prediction [MPa]**	**Exp. Result [MPa]**	**Error**
S_1	24.18	26.97 ± 1.6	10.34 %
S_{12}	N/A*	22.72 ± 0.81	N/A*
S_2	11.09	5.59 ± 1.65	98.38$^{\Delta}$ %
E_1	1404	1655.73 ± 73.22	15.2 %
E_{12}	N/A*	N/A*	N/A*
E_2	956.1	716.23 ± 118.12	27.0$^{\Delta}$ %

* No predictions were made as $\theta = 10°$ off-axis test was found invalid for FFF-ABS (see Section 7.4.3).

$^{\Delta}$ Error is likely due to the experimental data fluctuation discussed in Section 6.2.

Theoretical predictions for Tensile Test 1 used parameters of Void Density $\rho_1 = 0.2198$; Bond Length $b_3 = 0.358$; Coupon Width $l_w = 25.0$ mm; Coupon Thickness $l_z = 2.00$ mm.

Table 7.2: Comparison of theoretical predictions and experimental results, test 2.

Property	Theo. Prediction [MPa]	Exp. Result [MPa]	Error
S_1	28.12	N/A$^{\notin}$	N/A$^{\notin}$
S_{12}	10.82	10.81 $^{\diamond}$	0.09 %
$S_{\theta=45^\circ}$	18.65$^{\circledast}$	22.05 ± 0.78	15.87 %
$S_{\theta=60^\circ}$	17.95$^{\circledast}$	17.72 ± 0.73	1.29 %
S_2	18.41	18.9 ± 1.96	2.59 %
E_1	1636.38	N/A$^{\notin}$	N/A$^{\notin}$
$E_{\theta=45^\circ}$	1325.39$^{\circledast}$	1593.48 ± 78.92	16.82 %
$E_{\theta=60^\circ}$	1260$^{\circledast}$	1585.22 ± 60.6	20.5 %
E_2	1257.30	1515.74 ± 124.22	17.04 %

$^{\circledast}$ Values interpolated from theoretical predictions.

$^{\diamond}$ Values interpolated from experimental predictions.

$^{\notin}$ Values not shown as the interpolation functions are asymptotic for near-zero θ values.

Theoretical predictions for Tensile Test 2 used parameters of Void Density $\rho_1 = 0.0909$; Bond Length $b_3 = 0.594$; Coupon Width $l_w = 26.0$ mm; Coupon Thickness $l_z = 2.46$ mm.

7.2 Evaluation of Model

The second tensile test data correlated better with the mechanical property predictions than the first test. This is likely due to some of the flaws in the method employed in the first tensile test. These flaws are discussed in Section 7.4.2. It is also predicted that the model may degrade in accuracy as the air gap approaches zero. More testing would be needed to support or reject this hypothesis.

Each tensile test only tested a portion of the 0–90° range of angles. Ideally retesting would be performed to determine properties over the range of angles for a constant mesostructure. This was not possible due to time constraints of the project – each testing round took approximately four days to complete and the experimental design to overcome the experimental weaknesses required tremendous reseach effort. Figures 7.1–7.2 present theoretical prediction vs. experimental result plots over θ=0–90°. Void density ρ_1 and fibre bond length b_3 (and annealing time, though this was found to have a negligible effect) changes over the samples, which contributes to some of the error seen in the plots. The plots are presented as an indication that the mechanical characterisation correlates with the experimental predictions rather than as a definitive mechanical property plot. Applying the mechanical characterisation methods for a laminate with constant properties (constant b_3 and ρ_1) should achieve a better data fit.

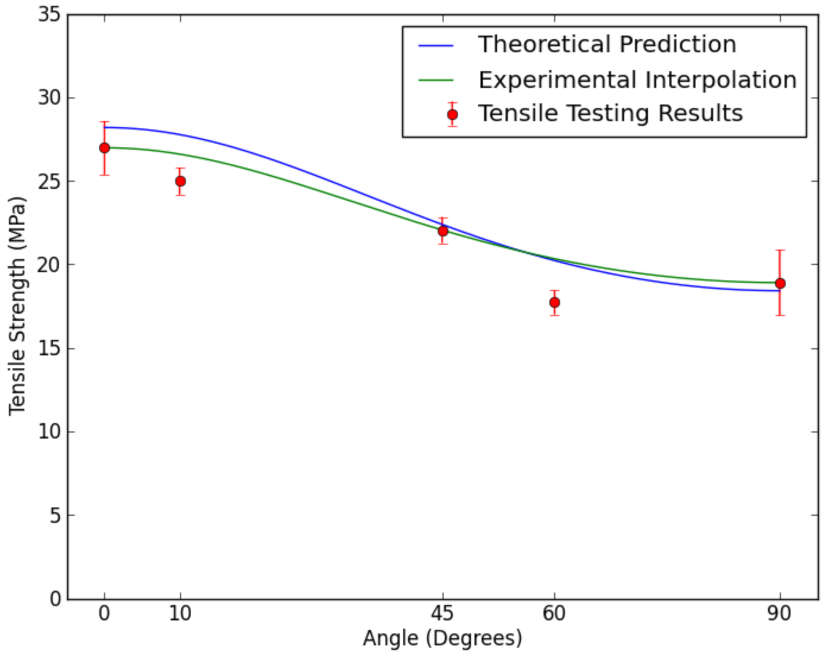

Figure 7.1: Plot of predicted strength vs. angle and comparison to experimental data.

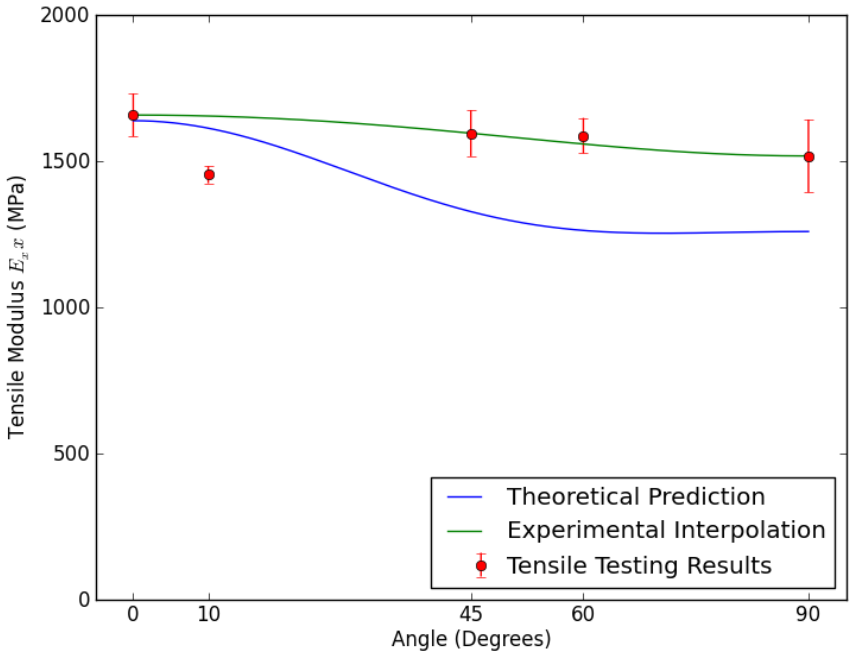

Figure 7.2: Plot of predicted elastic modulus vs angle and comparison to experimental data.

Figure 7.3 and 7.4 plot the property predictions for data published by Jose F. Rodriguez (2001) and Ahn et al. (2002) respectively. Mesostructure parameters were estimated based on data given in the studies. It should be noted that data published by Ahn et al. (2002) was incomplete, so the approximate mesostructure shape was derived from the fibre width, layer height and air gap parameters. This approximation is likely the source of the large error for small θ values. The figures are presented to demonstrate that the strength model applies across specimens fabricated under different influential parameters and on different FFF machines[1].

[1]Material strengths and other properties used to generate the model were taken from the respective published dataset.

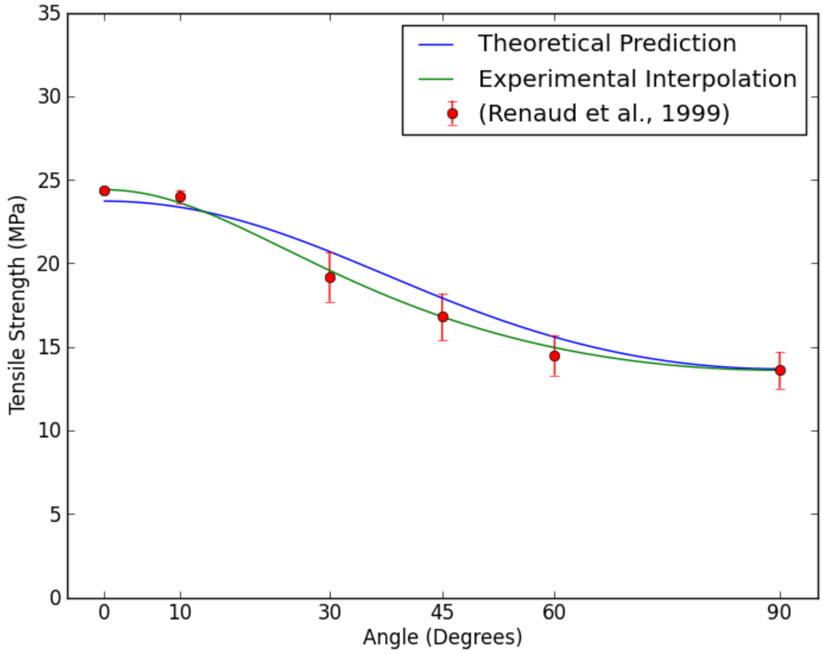

Figure 7.3: Plot of predicted strength vs. angle and comparison to data published by Rodriguez et al. (1999).

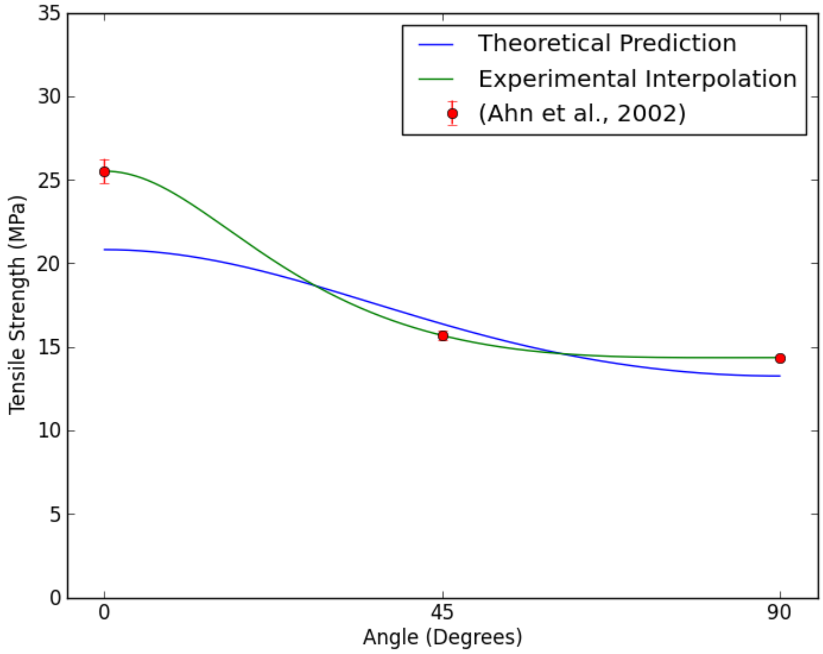

Figure 7.4: Plot of predicted strength vs. angle and comparison to data published by Ahn et al. (2002).

The strength predictions are shown to correlate well over a range of printing conditions.

The elastic modelling was found to correlate less well, though this is likely due to the varying void density conditions across the data. The elastic model also neglects to take into account the effects of strain in the y-direction[2]. This assumption was estimated to add about 7% error to the model[3].

The annealing of the specimens was found to have insignificant effect. This can be seen from the small variation between annealed and control groups in Table 6.3. The average difference between the non-annealed and the fully-annealed elastic modulus was 2.0%; the average difference for strength values was 1.1% [4]. This small difference between annealed and non-annealed indicates that even rudimentary temperature control during fabrication is sufficient to produce parts as reliable as those produced in the highly controlled environments of industrial printers. The insignificance of the heat-treatment time parameter also indicates that no significant molecular reorientation effects were present during fabrication, implying that the ABS elastic and strength properties were equivalent pre- and post- extrusion (see Section 3.4.4). This phenomena can thus be assumed to have negligible effect on the experimental results.

7.3 Failure Imagery

The experiment also gave supporting evidence to some of the assertions in the influential factors study (presented in Section 3).

Images of the post-failure specimens used in tensile test 1 are presented in Figures 7.5–7.7; Post-failure specimens used in tensile test 2 are presented in Figures 7.8–7.10.

[2] As the elastic characterisation has already been shown as accurate in Rodriguez et al. (1999), the study did not spend time on a full elastic characterisation and focused more on characterising the material strengths.

[3] Calculated using the elastic property prediction.

[4] These results excluded the θ=90° case from the first tensile test as the test was faulty.

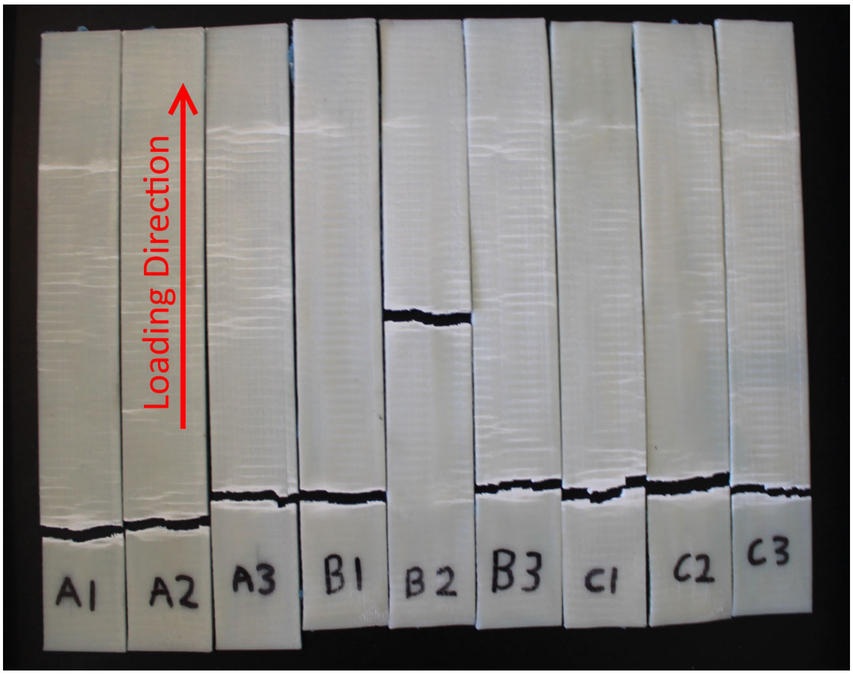

Figure 7.5: Tensile test 1 $\theta = 0°$ post-failure specimens.

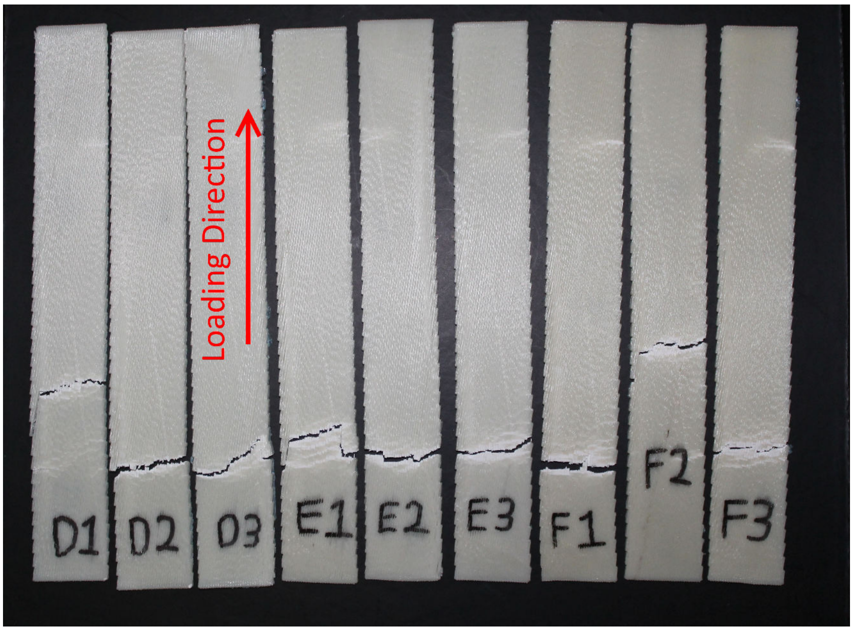

Figure 7.6: Tensile test 1 $\theta = 10°$ post-failure specimens.

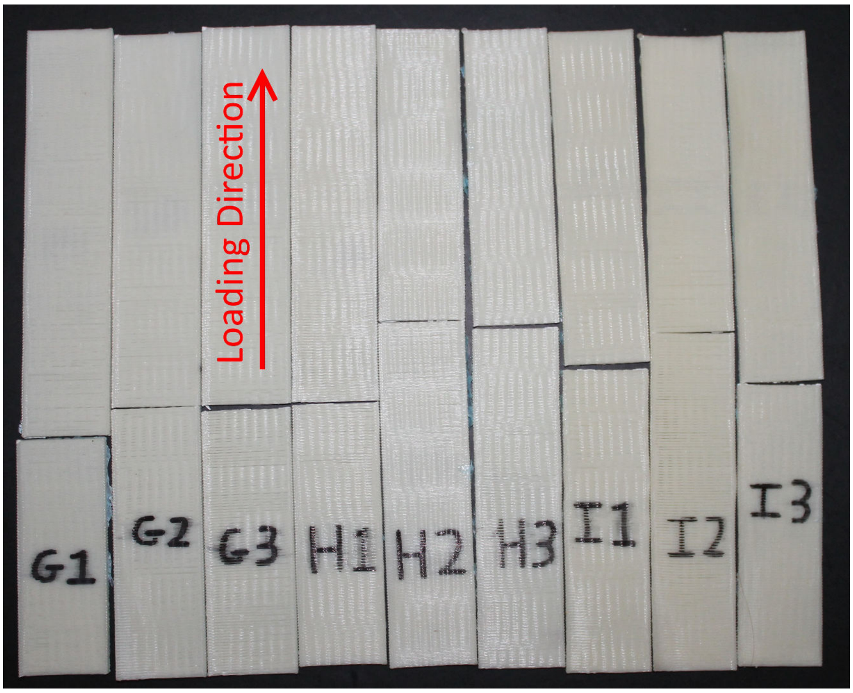

Figure 7.7: Tensile test 1 $\theta = 90°$ post-failure specimens.

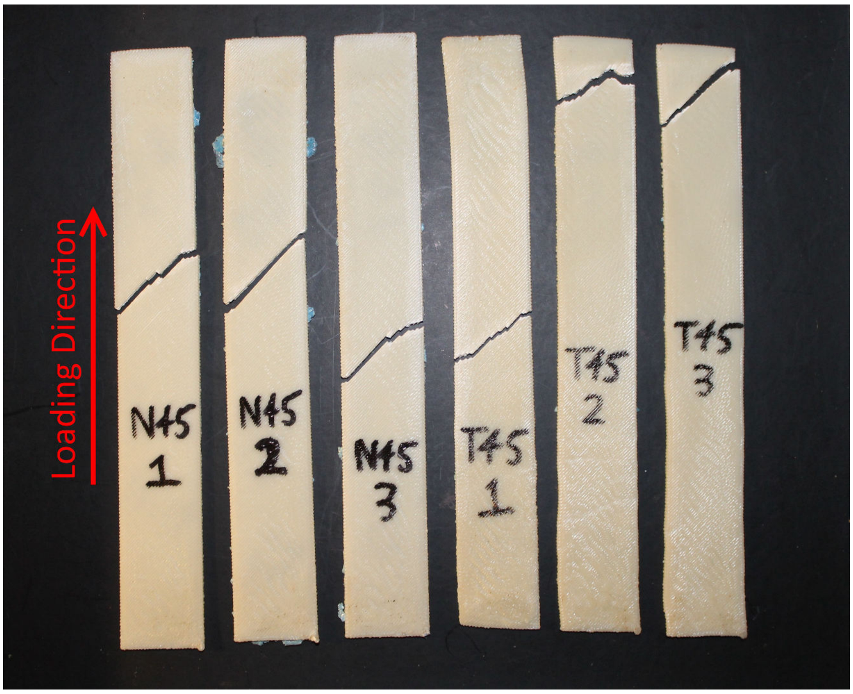

Figure 7.8: Tensile test 2 $\theta = 45°$ post-failure specimens.

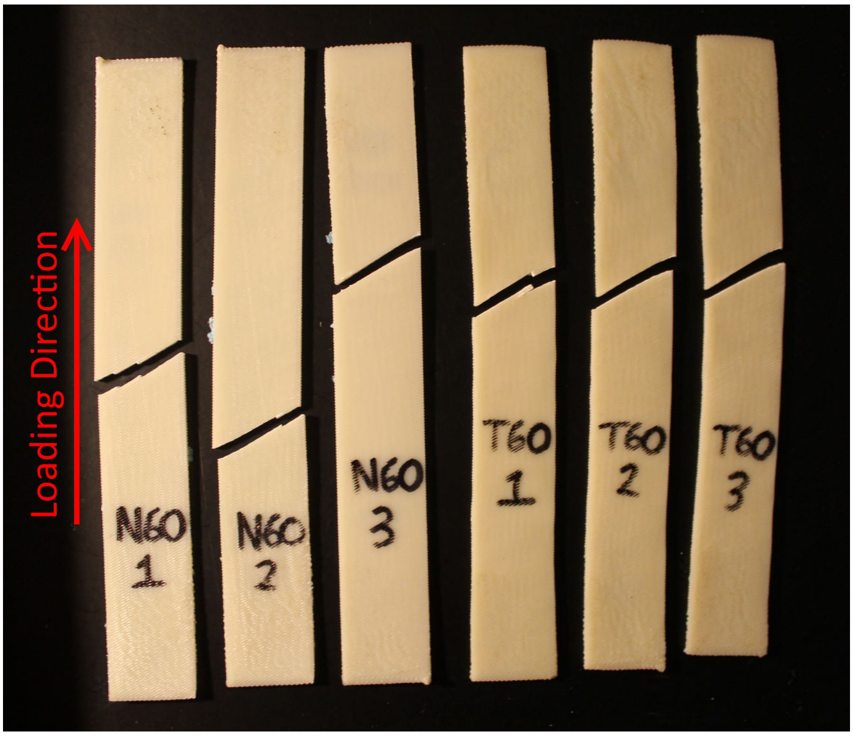

Figure 7.9: Tensile test 2 $\theta = 60°$ post-failure specimens.

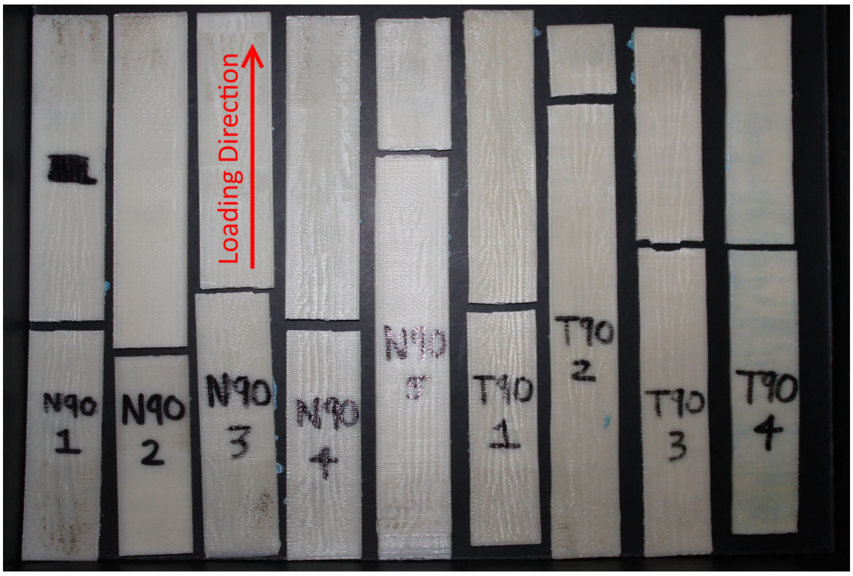

Figure 7.10: Tensile test 2 $\theta = 90°$ post-failure specimens.

Some interesting observations can be made from the post-failure specimens:

- The off-axis specimens failed in a very similar fashion to the longitudinal specimens. This is evidence for the invalidity of applying the off-axis test to characterise the shear strength of the FFF-ABS material (see Section 7.4.3).

- The $\theta = 45°$ and $\theta = 60°$ specimens failed in a mixed-shear failure mode, with the $\theta = 60°$ case being more similar to the transverse mode than the $\theta = 45°$ case. This provides evidence for the validity of using $\theta = 45°$ (and $\theta = 30°$) specimens to characterise interfibre shear strength (see Section 7.4.3).

- The $\theta = 90°$ specimens failed with no crazing[5] present, signifying that the composite failed well before the bulk material strength was reached. The specimens also failed very quickly compared to the ductile failure of the small angle specimens. This supports the assertion that transverse failure is characterised by brittle fracture across the bond surfaces.

7.4 Experimental Improvements

A major portion of the research was spent designing an adequate experimental process. Each issue encountered is detailed in this section as well as recommended solutions for future research.

7.4.1 Bulk Filament Material

The composition of ABS varies widely depending on the composition and manufacturer (Colborn et al., 1993). The magnitude of this variation is exemplified best by Lokensgard (2004): "Because [ABS grades] possess such a diverse combination of properties, many experts classify them as a family of plastics". Some material properties for the PA-747 grade were simply not available, notably the fracture strength, poissons ratio and shear modulus. Other material properties, such as tensile yield strength, were not explicitly stated or mislabelled and the correct property had to be inferred from the ISO standards. This study used the most well-specified filament found available for purchase – showing the issue as a problem across FFF filament suppliers.

It is proposed to use a standard composition in future research, perhaps from Stratasys Inc – their materials range seem to have better data available and are more reputable than generic filament manufacturers. This would effectively remove the variation in material between future studies, allowing the effects of the actual FFF process to be better understood. Material properties in future should also be compared pre- and post-

[5] Whitening due to strain as material appoaches the stress/strain limit.

extrusion[6], to quantify the effect of molecular reorientation during the printing process. This molecular reorientation process was determined by Jose F. Rodriguez (2001) to have a significant effect on the yield strength of the individual fibres.

Future testing using heat-treatment of the composite should also use a better control mechanism for the environment temperature; as discussed in Section 5.2.2, the 'bang-bang' controller present in the conventional oven used for heat treatment resulted in undesirable temperature fluctuations.

7.4.2 Tensile Testing Improvements

Coupon design plays a major role in determining the resultant tensile strength of the part. Some prior mechanical studies, notably those performed by Tymrak et al. (2014) and Sood et al. (2009), fabricated 'dogbone' shape tensile coupons commonly used in metal tensile testing. This coupon design is flawed for use in composites, however, as fibre discontinuities can be printed at the change in cross section, which results in a large local stress concentration. The material strength is therefore underestimated, as the specimens tended to fracture at the cross section discontinuity. It is recommended that future testing follows the ASTMD3039 standard tensile coupon shape.

The mechanical testing was also subject to a large amount of jaw breaks as discussed in Section 6. This showed that the maximum stress was underestimated as a stress concentration existed at the jaw interface. It was thought that this issue would be avoided by using cloth emery tabs to distribute the jaw compressive stress evenly. This was not the case. Simple bevelled tabs can not be used because of the stress discontinuity issue mentioned earlier; It is therefore recommended that future testing uses tabs of FFF-ABS or steel glued to the grip area of each specimen after fabrication.

Future testing should also be wary of the printer pathing and it's effects on the specimen. The first tensile test did not extrude ABS to join each fibre – extrusion was stopped at the end of a fibre and started at the beginning of a new fibre. This resulted in a large stress concentration being formed in between the ends of the fibres. Figure 7.11 illustrates this effect. This likely contributed to the weaker strengths seen in the first transverse tensile test; it is recommended that future testing uses a continuous rectilinear

[6] This can be accomplished by mechanical testing of filament and fibre respectively

pathing as shown in Section 3.2.4.

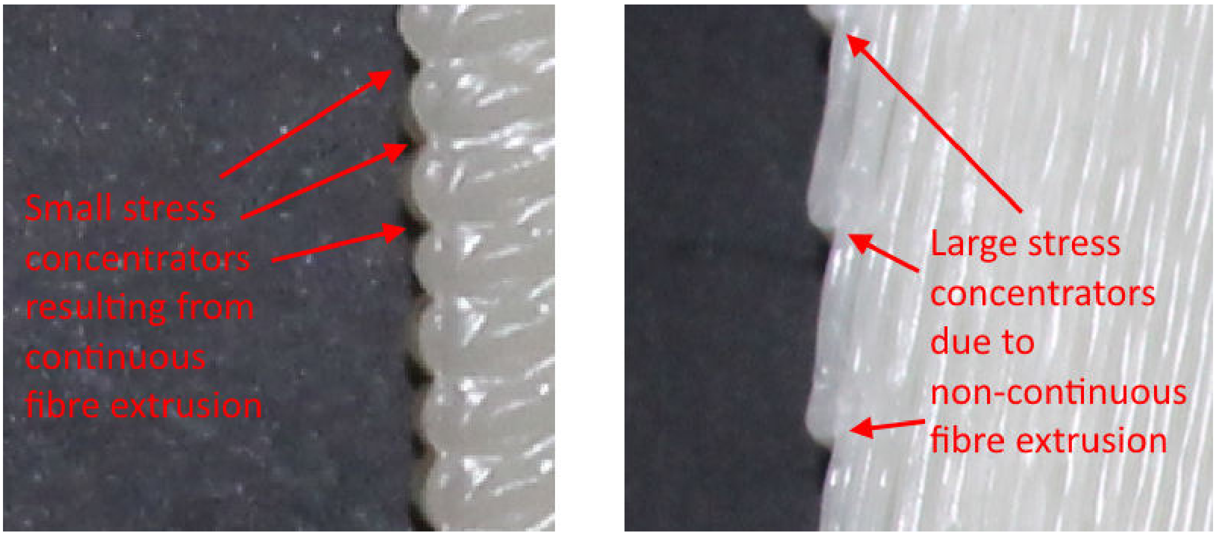

Figure 7.11: Illustration of the stress concentration effects of non-continuous extrusion.

The rate at which strain is applied to the tensile coupon also significantly influences the mechanical strength. Research shows the tensile strength for the same coupon varied from 19–28 MPa over three orders of magnitude of strain rate change. It is recommended that testing compensates for this by setting the extension speed[7] of the tensile test machine to 2 mm/minute. This guideline is recommended by ASTM in standard D3039 "Standard Test Method for Tensile Properties of Polymer Matrix Composite Materials" (ASTM-International, n.d.) and also chosen based on prior mechanical testing being performed at this speed. The speed also provides an approximation to true static behaviour as loading is at such a slow strain rate.

It is furthermore recommended that all future mechanical testing on FFF composites include full description of a parameters table and mesostructure microscopy, similar to Table 5.1 seen in this investigation. This allows meta-analyses to be carried out on prior studies.

7.4.3 Off-Axis Tensile Test

Some research, notably Renaud et al. (1999), condone using an *off-axis* test to estimate the interfibre shear strength S_{12}. In an off-axis test, a specimen with 10° raster orientation is tensile tested to failure. This failure stress is then taken as the σ_x stress in the Azzi and Tsai multiaxial strength equation (see Section 4.4). If longitudinal fibre strength S_1

[7] Also referred to as *cross-head speed* in some texts.

and transverse strength S_2 are known, the equation can be solved for the interfibre shear strength S_{12}. This study determined that the off-axis test is invalid to apply to FFF composites. Chamis and Sinclair (1976) gives criteria for validity of the off-axis test as

> "If a 10° off-axis specimen is to serve as a means for intralaminar shear characterisation of a uniaxial composite, the intralaminar shear stress σ_{12} must be the only one of these three stresses [axial, transverse and intralaminar shear] that is near its critical value, and fracture must occur at the 10° plane when σ_{12} reaches this critical value."

The off-axis test was found to fail both criteria for FFF-ABS material. The first criteria, for which σ_{12} must be near the critical value while σ_1 and σ_2 are not, can be shown to be false in both data from Renaud et al. (1999) and this experiment. If a tensile load is applied to a specimen with a raster orientation of $\theta = 0°$, the material-coordinate stresses are given by a stress transformation as:

$$\sigma_1 = \cos\theta^2 \sigma_x \approx 0.97\sigma_x \tag{7.1}$$

$$\sigma_2 = \sin\theta^2 \sigma_x \approx 0.03\sigma x \tag{7.2}$$

$$\tau_{12} = -\sin\theta\cos\theta\sigma_x \approx -0.17\sigma x \tag{7.3}$$

It can be observed that the $\frac{\sigma_{12}}{S_{12}} >> \frac{\sigma_1}{S_1}, \frac{\sigma_2}{S_2}$ criteria[8] is satisfied only if S_1 is much greater than S_{12}. Renaud et al. (1999) reported S_1 as 24.4 MPa and the studies‘ S_{12} value can be estimated by the multiaxial strength theory as $S_{12} \approx 10.6$ MPa, which does not satisfy this criteria.

It was also observed that fracture did not occur along the 10° plane during the off-axis test. Figure 7.6 shows the post-failure off-axis test coupons; it can be seen that fracture occured normal to the applied stress in almost all specimens. Only specimens D1 and E1 showed fracture along the 10° plane, and even these specimens ultimately failed normal to the tensile force axis. This is further supported by post-failure microscopy

[8] ie. "σ_{12} must be near the critical value while σ_1 and σ_2 are not"

shown in Figure 7.12, which shows the 'cup and cone' post-failure shape characteristic to ductile tensile failure.

Figure 7.12: Post-failure microscopy of the $\theta = 10°$ off-axis tensile test.

Having shown the off-axis test is inapplicable, it was then desirable to determine an effective method of characterising the interfibre shear strength. Figure 7.13 shows the multiaxial strength theory prediction using differing raster orientation failure stresses to estimate S_{12} (using data from Renaud et al. (1999) with $S_1 = \sigma_x$ at $\theta = 0°$ and $S_2 = \sigma_x$ at $\theta = 90°$); it can be seen from the plot that the 30°,45° and 60° orientations give very accurate S_{12} estimations.

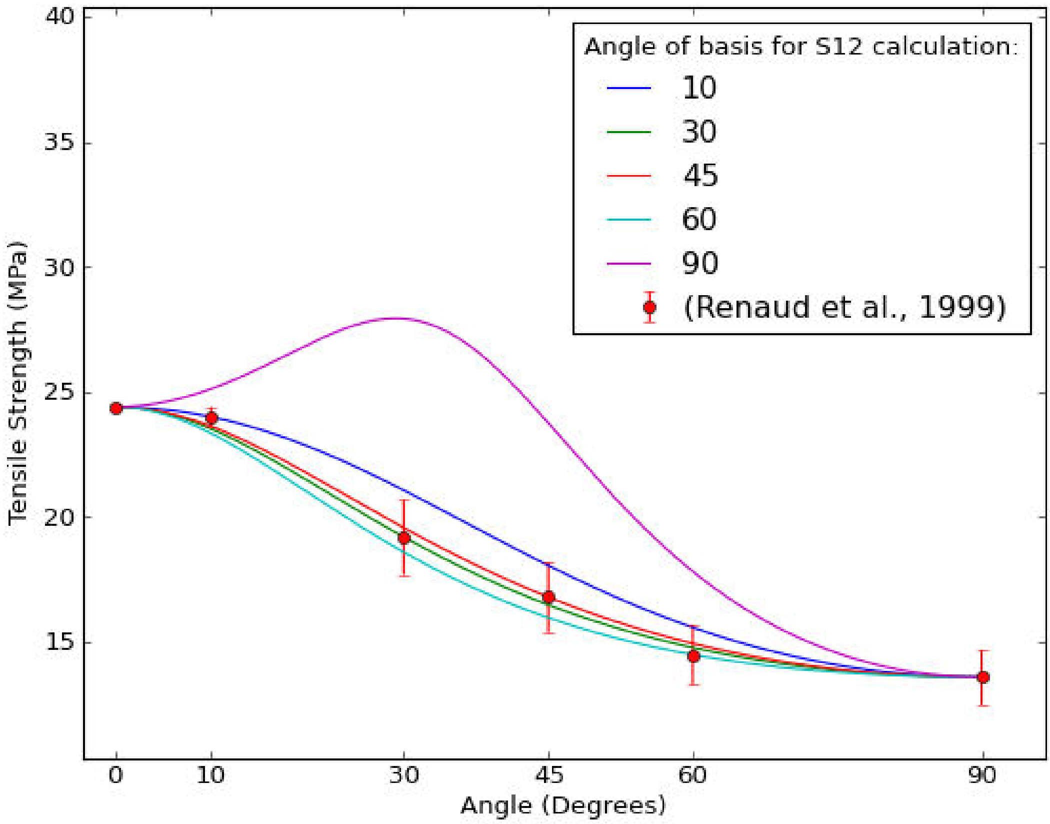

Figure 7.13: S12 estimation for different angles.

A tensile test at $\theta = 30°$ is therefore recommended for future mechanical estimation of S_{12} for FFF-ABS composites. Based on the testing criteria discussed above, it is desirable to estimate S_{12} based on testing performed where the other stresses are not approaching their critical value. As the transverse strength S_2 is usually half of the longitudinal strength S_1 in most prior mechanical testing, the angle where neither material stress is close to it's failure stress can be found by

$$\min \frac{\sigma_1}{S_1} \text{ and } \frac{\sigma_2}{S_2} \tag{7.4}$$

assuming $S_1 \approx 2S_2$ desirable θ can be found by stress transformation as (7.5)

$$\frac{\sigma_x \cos^2 \theta}{S_1} = \frac{\sigma_x \sin^2 \theta}{S_2} \approx \frac{\sigma_x \cos^2 \theta}{2S_2} = \frac{\sigma_x \sin^2 \theta}{S_2} \tag{7.6}$$

which simplifies to give

$$2 \sin^2 \theta = \cos^2 \theta \tag{7.7}$$

$$\therefore \sqrt{2} = \frac{\cos\theta}{\sin\theta} \tag{7.8}$$

$$\therefore \theta \approx 30^\circ \tag{7.9}$$

Future research could also investigate the possibility of applying polymer-matrix-composite test standards to FFF-ABS material to solve this problem, notably ASTM D3518[9].

[9]"Standard Test Method for In-Plane Shear Response of Polymer Matrix Composite Materials"

8: Conclusions and Recommendations

The study covered a broad scope of FFF topics. The major products of the research are listed below:

- A comprehensive list of parameters influential to the mechanical properties was developed, providing a background for future research to use. Prior to this being produced, a comprehensive list of influential factors did not exist (Section 3);
- It was found that an inexpensive microscope and public-domain image analysis software was sufficient to accurately determine the mesostructural properties of the printed material, removing the need for Scanning Electron Microscopy and enhancing the potential cost benefits of FFF manufacturing (Section 5.2.4);
- A laminate strength model was developed that allows prediction of the orthotropic material strengths from the mesostructural properties derived from microscopy (Section 4.4);
- Experimental tensile test data was produced for coupons fabricated on a consumer-level FFF machine (Section 6);
- Issues arising during tensile testing were discussed and mitigated, providing a base for further research (Section 7.4.2);
- The developed laminate strength model was compared to the experimental results, and found to correlate very well. Previously established elastic modelling approaches were also applied to the data, and found to correlate reasonably well (Section 7.1);

The investigation posed three research questions at the commencement of the study:

- Is it possible to predict the mechanical behaviour of FFF-ABS material?
- Is it possible to predict this behaviour consistently if the parts are produced using a consumer-level printer, as the machine may not have the same precision as industrial printers previously used in research?

- Can post-fabrication annealing 'heal' the effects of a varied temperature history on the material, allowing more consistent mechanical properties and thus a more accurate mechanical characterisation?

Mechanical behaviour was able to be consistently predicted even when specimens are fabricated using a consumer-level printer. The post-fabrication annealing was found to have negligible effects on the printed part, suggesting that a rudimentary build enclosure provides sufficient temperature control to produce reliable mechanical properties.

This suggests that reliable structural FFF parts are able to be printed for use in applications from flexible product manufacturing to biomedical engineering. Further research is required before this becomes a reality, however. It is recommended that future research focuses on characterising the FFF-ABS material under more complex loading cases. This was initially aimed to be accomplished by this study, however the required influential factor research and material characterisation methods did not exist.

The 'OGCode' pather was developed to make cylindrical hydrostatic test vessels and could easily be modified to produce arbitrary shapes. Hydrostatically burst-testing these arbitrary shapes could determine the accuracy of the strength model under a complex stress field. If the FFF-ABS material is able to be reliably characterised under complex loading, it could have enormous influence on the way products are made and used – allowing labour- and shipping-free recyclable products to be produced locally, cheaply and on-demand.

References

Agarwaia, M. K., Jamalabad, V. R., Langrana, N. A., Safari, A., Whalen, P. J., and Danforth, S. C. (1996). Structural quality of parts processed by fused deposition [Journal Article]. *Rapid Prototyping Journal*, *2*(4), 4-19.

Ahn, S.-H., Montero, M., Odell, D., Roundy, S., and Wright, P. K. (2002). Anisotropic material properties of fused deposition modeling abs [Journal Article]. *Rapid Prototyping*, *8*(4), 248-257.

ASM-International. (2004). *Tensile testing* (Second Edition ed.) [Book].

ASTM-International. (n.d.). *Standard test method for tensile properties of polymer matrix composite materials* (Vol. D3039/D3039M) [Standard]. ASTM International.

Azzi, V., and Tsai, S. (1968). Anisotropic strength of composites [Journal Article]. *Experimental Mechanics*, *5*(9), 283-288.

Barbero, E. J. (2008). *Finite element analysis of composite materials* [Book]. Boca Raton: CRC Press. (2007007536 000041323263 (OCoLC)85485011 Ever J. Barbero. ill. ; 26 cm. Includes bibliographical references and index.)

Barbero, E. J. (2011). *Introduction to composite materials design* (2nd ed.) [Book]. Boca Raton: Taylor and Francis. (2010018871 000045597655 (OCoLC)226357459 author, Ever J. Barbero. ill. ; 26 cm. Includes bibliographical references and index.)

Barbero, E. J. (2014). *Finite element analysis of composite materials using ansys* (2nd Edition ed.) [Book]. Boca Raton, FL, USA: CRC Press.

Bauer, J., Hengsbach, S., Tesari, I., Schwaiger, R., and Kraft, O. (2014). High-strength cellular ceramic composites with 3d microarchitecture [Journal Article]. *PNAS*, *111*(7), 2453-2458.

Bellehumeur, C., Li, L., Sun, Q., and Gu, P. (2004). Modelling of bond formation between polymer filaments in the fused deposition modelling process [Journal Article]. *Journal of Manufacturing Processes*, *6.2*, 170-178. Retrieved from `http://search.proquest.com.ezproxy.library.uq.edu.au/docview/195248994/abstract/AAF048BDBD5C4497PQ/1?accountid=14723`

Bellini, A., and Guceri, S. (2003). Mechanical characterisation of parts fabricated using fused deposition modeling [Journal Article]. *Rapid Prototyping Journal*, *9*(4), 252-264.

Bogetti, T. A., Hoppel, C. P., and Drysdale, W. H. (1995, October 1995). *Three-dimensional effective property and strength prediction of thick laminated composite media* (Report). Army Research Laboratory.

Boulton, C. (2013). *Printing out barbies and ford cylinders* [Newspaper Article]. Retrieved from `http://online.wsj.com/news/articles/SB10001424127887323372504578469560282127852`

Cantu, K. M., and Jonsson, E. W. (2012). *3d printing for end products* (Thesis).

Chamis, C. C., and Sinclair, J. H. (1976, April 1976). *10 degree off-axis tensile test for intralaminar shear characterization of fiber composites* (Report). National Aeronautics and Space Administration.

Chi-Mei-Corporation. (2006). *Chi mei polylac pa-747 abs datasheet* [Dataset]. Chi-Mei Corporation.

Colborn, R., Buckley, D., and Adams, M. (1993). *Acrylonitrile-butadiene-styrene* [Electronic Article]. iSmithers Rapra Publishing.

Corp, D. (2014). *Plastic properties of acrylonitrile butadiene styrene (abs)* (Vol. 2014) (Web Page No. 30 September 2014). Retrieved from `www.dynalabcorp.com/technical_info_abs.asp`

Corporation, C. M. (2005). *Polylac pa747 msds* [Dataset]. Chi-Mei Corporation.

Datavase, M. M. P. (2014). *Overview of materials for acrylonitrile butadiene styrene (abs), extruded* [Web Page]. Retrieved from `http://www.matweb.com/search/DataSheet.aspx?MatGUID=3a8afcddac864d4b8f58d40570d2e5aa&ckck=1`

El-Gizawy, A. S., Corl, S., and Greybill, B. (n.d.). *Process-induced properties of fdm products* (Report). Mechanical and Aerospace Engineering Department, University of Missouri, Columbia, MO.

Gates, D. J. (2014). *Lefm validity and limitations* (Report). University of Queensland.

Gibson, R. F. (2007). *Principles of composite material mechanics* (2nd ed.) [Book]. Boca Raton: CRC Press. (2007013616 000041499220 (OCoLC)122338139 Ronald F. Gibson. ill. ; 24 cm. Includes bibliographical references and index. Mechanical engineering series (Boca Raton, Fla.) ; 205. Mechanical engineering series (Boca Raton, Fla.))

Gray, P., and Kaila, V. (2006). *Anisotropic axisymmetric fem - advanced finite element methods* (Thesis).

Huang, Q., Zhang, J., Sabbaghi, A., and Dashupta, T. (n.d.). *Optimal offline compensation of shape shrinkage for 3d printing processes* (Thesis).

Illiescu, M., Nutu, E., and Comanescu, B. (2008). Applied finite element method simulation in 3d printing [Journal Article]. *International Journal of Mathematics and Computers in Simulation*, *2*(4).

Inc., S. (2011a). *3d printing with fdm: How it works* (Report). Author

Inc., S. (2011b). *Abs-p400 datasheet* [Dataset].

Industries, B. (2014). *The importance of high quality filament in 3d printing* [Aggregated Database]. Retrieved from `bootsindustries.com/portfolio-item/importance-of-good-filament`

Jose F. Rodriguez, J. E. R., James P. Thomas. (2001). Mechanical behaviour of acrylonitrile butadiene styrene (abs) fused deposition materials. experimental investigation [Journal Article]. *Rapid Prototyping Journal*, *7*(3), 148-158.

Kreiger, M., Anzalone, G., Mulder, M., Glover, A., and Pearce, J. (2013). Distributed recycling of post-consumer plastic waste in rural areas [Journal Article]. *MRS Online Proceedings Library*(1492).

Lan, J. (2013). *Design and fabrication of a modular multi-material 3d printer* (Thesis).

Landel, R. F., and Lielsen, L. E. (1993). *Mechanical properties of polymers and composites* (2nd Edition ed.) [Book]. CRC Press.

Leigh, S. J., Bradley, R. J., Purssell, C. P., Billson, D. R., and Hutchins, D. A. (2012). A simple, low-cost conductive composite material for 3d printing of electronic sensors [Journal Article]. *PLOS One*. doi: 10.1371/journal.pone.0049365

Li., L., Sun., Q., Bellehumeur., C., and Gu., P. (2001). *Composite modeling and analysis of fdm prototypes for design and fabrication of functionally graded parts* [Conference Paper].

Li, L., Sun, Q., Bellehumeur, C., and Gu, P. (2002). *Analysis and fabrication of fdm* *prototypes with locally controlled properties* (Thesis).

Li, L., Sun, Q., Bellehumeur, C., and Pu, G. (2002). *Investigation of bond formation in fdm process* [Conference Paper].

Lilleholm, L. (2014). *Awesome 3-d printing tech we can't show you on tv - yet* [Newspaper Article]. AlJazeera America. Retrieved from `http://america.aljazeera.com/watch/shows/techknow/blog/2014/1/2/awesome-3d-printingtechwecantshowyouontvyet.html`

Liu, G. R., and Quek, S. S. (2003). *The finite element method : a practical course* [Book]. Oxford ; Boston: Butterworth-Heinemann. (000025447748 (OCoLC)51234350 (Gui-Rong) G.R. Liu, S.S. Quek. ill. ; 25 cm. Includes bibliographical references (p. 342-343) and index.)

Lokensgard, E. (2004). *Industrial plastics: Theory and applications* (4th Edition ed.) [Book]. Delmar Learning.

Mamadapur, M. S. (2007). *Constitutive modeling of fused deposition modeling acrylonitrile butadiene styrene (abs)* (Thesis).

Martinez, J., Dieguez, J., Area, E., Pereira, A., Hernandez, P., and Perez, J. (2013). *Comparitive between fem models for fdm parts and their approach to a real mechanical behaviour.* [Conference Paper].

McCue, T. (2014). *3d printed prosthetics* [Newspaper Article]. Retrieved from `http://www.forbes.com/sites/tjmccue/2014/08/31/3d-printed-prosthetics/`

Nettles, A. (1994). *Basic mechanics of laminated composite plates* (Report).

Ning, X., and Pellegrino, S. (2012). *Design of lightweight structural components for direct digital manufacturing* (Thesis).

Nordgren, F., and Nyquist, M. (2006). *Fe modelling of pc/abs experimental tests and simulations* (Thesis).

Norris, C. (1962). *Strength of orthotropic materials subjected to combined stress* (Report). Forest Product Laboratory Report.

of Boiler, N. B., and Inspectors, P. V. (2013). Bulletin: Technical journal of the national board of boiler and pressure vessel inspectors [Journal Article]. *3D Printing: The New Design of Safety*, *Fall 2013*(1), 26-33.

Ogden, S., and Kessler, S. (n.d.). Anisotropic finite element modeling of the fused deposition modeling process [Conference Proceedings]. In J. S. Carpenter et al. (Eds.), *Characterization of minerals, metals and materials 2014*. TMS The Minerals, Metals and Materials Society.

Owyang, J. (2014). *Maker movement and 3d printing: Industry stats* (Web Page No. 30th September 2014). Retrieved from `www.web-strategist.com/blog/2014/02/13/maker-movement-and-3d-printing-industry-stats/`

Panda, S. K., Padhee, S., Sood, A. H., and Mahapatra, S. (2009). Optimization of fused deposition modeling (fdm) process parameters using bacterial foraging technique [Journal Article]. *Intelligent Information Management*, *1*, 89-97.

Renaud, J. E., Rodriguez, J., and Thomas, J. P. (1999). *Modeling the mechanical behaviour of fused deposition acrylonitrile-butadiene styrene polymer components* (Thesis).

Rodriguez, J., Thomas, J. P., and Renaud, J. E. (2000). Characterization of the mesostructure of fused-deposition acrylonitrile-butadiene-styrene materials [Journal Article]. *Rapid Prototyping*, *6*(3), 175-185.

Rodriguez, J., Thomas, J. P., and Renaud, J. E. (2003). Design of fused-deposition abs components for stiffness and strength [Journal Article]. *Journal of Mechanical Design, ASME*, *125*, 545.

Rooke, D., and Cartwright, D. (1974). *Compendium of stress intensity factors* [Book]. London: Her Majesty's Stationery Office.

Rust, W., Kracht, M., and Overberg, J. (2009). *Experiences with ansys in ultimate-load analyses of aircraft fuselage panels* (Report). University of Applied Sciences, Fachhochschule Hannover.

Sin, Q., Rizvi, G., Bellehumeur, C., and Gu, P. (2008). Effect of processing conditions on the bonding quality of fdm polymer filaments [Journal Article]. *Prototyping Journal*, *14*(2), 72-80.

Sood, A. K., Ohdar, R., and Mahapatra, S. (2009). Parametric appraisal of mechanical property of fused deposition modelling processed parts [Journal Article]. *Materials and Design*, *31*, 287-295.

Stegmann, J. (2005). *Analysis and optimisation of laminated composite shell structures* (Thesis).

Sun, C., and Jin, Z. (2012). *Fracture mechanics* [Book]. Elsevier.

Sun, C., and Vaidya, R. (1995). *Prediction of composite properties from a representative volume element* (Report). School of Aeronautics and Astronautics, Purdue University.

Thomas, J., and Rodriguez, J. (2000). *Modeling the fracture strength between fused-deposition extruded roads* [Conference Paper].

Townsend, V. (2010). *Relating additive and subtractive processes teleologically for hybrid design and manufacturing* (Thesis).

Tsai, S. W. (1965). *Strength characteristics of composite materials* (Report). National Aeronautics and Space Administration.

Tymrak, B., Kreiger, M., and Pearce, J. (2014). Mechanical properties of components fabricated with open-source 3-d printers under realistic environmental conditions [Journal Article]. *Materials and Design*, *58*, 242-246.

Yardimci, M., and Guceri, S. (1995). Numerical modeling of fused deposition processing [Journal Article]. *Proc. of ASME Materials Division*, *MD-v69-2*, 1225-1235.

Y. Zhang, Y. K. C. (2006). Three-dimensional finite element analysis simulations of the fused deposition modelling process [Journal Article]. *Journal of Engineering Manufacture*, *220*, 1633-1643.

Ziemian, C., Sharma, M., and Ziemian, S. (2012). Anisotropic mechanical properties of abs parts fabricated by fused deposition modeling [Book Section]. In D. M. Gokcek (Ed.), *Mechanical engineering.* Rijeka, Croatia: InTech.

Appendix A: 'OGCode' Slicer

The 'OGCode' slicer was written to allow precise control over the mesostructural parameters of the test specimen – as conventional slicing programs are designed to produce non-structural components, the programs usually only allow minimal changes to the pathing parameters. Slicing programs are being actively developed, however. Future research conducted on FFF should first investigate if a slicing program that allows control over mesostructural parameters exists before using this code.

The 'OGCode' slicer was built to provide simple, precise pathing to produce the test specimens. The program was written using Python (Portable Edition) (`version 3.2.5.1`) and the python `numpy` module. The G-code produced has only been tested as compatible with Solidoodle 3 firmware/hardware – other printers will likely require some re-working of the code to print properly.

The code is briefly documented as follows:

- OGCode outputs a G-code file named 'OGCodeOutput.gcode'. This file is overwritten when the code is run, and so should be renamed if it is to be saved.
- Printing parameters are established in the 'Build parameters' block at the start of the python code; these parameters are explained in Section 3.
- `startGcode` function calls the printer initialisation code: millimeter units are used; absolute position references are established; system fan is turned off (to remove influence on heating of the FFF part); extruder is moved to printer center.
- ASTMD3039 standard specimens (and arbitrary rectangular prisms) can be called through use of the `block` function: `pathAngleDeg` defines the raster orientation in degrees; `x0,y0,z0` define the starting corner (towards origin) of the block for the `x,y,z` coordinates; `xLength,yLength` define the lengths of the block in the x- and y- axes respectively; `height` defines the vertical build height of the block. For example, a $\theta = 90°$ ASTMD3039 standard should be called with parameters `(90.0,0.0,0.0,0.0,25.0,185.0,2.0)`.

- Cylindrical shapes can be called through use of the `cylinder` function. This feature was originally to be used to analyse the effect of curves and corner stress concentrators on the mechanical strength of a component by hydrostatic burst testing – though the project time constraints did not allow this, it is left in the code in case further research can make use of it. Cylindrical shapes can be called multiple times to build pressure test vessels - an example of this is shown in the 'Specimen Definition' block of the code.

- The `endGcode` function brings the extruder head back to the home position and writes the G-code file to 'OGCodeOutput.gcode'.

The 'OGCode' slicer program source code is included on the following pages.

```python
########################################################################
#                    'OgCode' pathing program.                         #
#          Perpetually providing precise printer pathing.              #
# Developed by Sam Barrett, samuel.alexander.barrett@gmail.com #
########################################################################

import numpy as np
import math

############################### Build parameters ###############################
#Proposed standard FFF tensile settings are:
#  layerHeight=0.4;layerWidth=0.4;bulkDiameter based on average of 20
    diameter measurements;
#  Eactual based on commanding 'extrude 100mm' and measuring filament feed-
    through.

layerHeight=0.4 #[mm]
fibreWidth=0.4 #[mm] Note: *Diameter*
fibreArea=(fibreWidth/2.0)*(layerHeight/2.0)*math.pi #Area of fibre,
    assuming elliptical x-section.

bulkDiameter=1.79 #[mm] Note: *Diameter* of the bulk filament.
bulkArea=math.pi*(bulkDiameter/2.0)**2 #Area of bulk filament x-section,
    assuming circular x-section.
dEpermm=fibreArea/bulkArea

#Account for incorrect calibration in extruder steps:
Einput=100 #Input extrusion value [mm]
Eactual=126.5 #Actual extruded value [mm]
Emod=Einput/Eactual #Modifier to tune to correct 'extrusion per mm' value
dEpermm=dEpermm*Emod

#Account for desired gap width - see 'slicing parameters' in report.
airGapHorizontal=-0.04 #Desired gap width modifier [mm], currently one-
    tenth of fibre diameter
airGapVertical=-0.04 #Desired gap width modifier [mm], currently one-tenth
    of fibre diameter
fibreWidth=fibreWidth+airGapHorizontal #fibreWidth now accounts for desired
     airGap
layerHeight=layerHeight+airGapVertical #layerHeight now accounts for
    desired airGap

############################ End Build Parameters ############################




######################## START OF OGCODE DEFINITIONS ########################
#Note: These definitions control the pathing parameters of the printer.
#They should not need to be altered to simply print a specimen.
#Specimens are defined at the bottom of the code.


gcodeFilename = 'OGCodeOutput.gcode'
gcode=open(gcodeFilename,'w')

#Define initial coordinates on global level. Sequence is G X Y Z F E.
G='G1'
X=0.0
Y=0.0
Z=0.0
F=0.0
E=0.0

def startGcode():
    #Comment on settings:
```

```python
    gcode.write(';Print Settings: \n')
    gcode.write(';layerHeight  ')
    gcode.write(str(layerHeight))
    gcode.write(',\n ;fibreWidth ')
    gcode.write(str(fibreWidth))
    gcode.write(',\n ;fibreArea ')
    gcode.write(str(fibreArea))
    gcode.write(',\n ;bulkDiameter ')
    gcode.write(str(bulkDiameter))
    gcode.write(',\n ;bulkArea ')
    gcode.write(str(bulkArea))
    gcode.write(',\n ;dEpermm ')
    gcode.write(str(dEpermm))
    gcode.write('\n')

    #Set units to [mm]:
    gcode.write('G21\n')

    #Set all coordinates to absolute positioning:
    gcode.write('G90\n')
    gcode.write('G90 X0 Y0 Z0\n')

    #Set E datum to 0:
    gcode.write('G92 E0\n')

    #Home X,Y axes:
    gcode.write('G28 X0 Y0 \n')

    #Fast move to center:
    gcode.write('G1 X100 Y100 F4000\n')

    #Home Z axis:
    gcode.write('G28 Z0\n')

    #Turn fan off:
    gcode.write('M107\n')

    #Set extruder to absolute positioning:
    gcode.write('M82\n')

def sendCommand(C,X,Y,Z,F,E):
    gcode.write(C)
    gcode.write(' ')
    gcode.write('X')
    gcode.write(str(X))
    gcode.write(' ')
    gcode.write('Y')
    gcode.write(str(Y))
    gcode.write(' ')
    gcode.write('Z')
    gcode.write(str(Z))
    gcode.write(' ')
    gcode.write('F')
    gcode.write(str(F))
    gcode.write(' ')
    gcode.write('E')
    gcode.write(str(E))
    gcode.write('\n')

def cylinder(pathing,xc,yc,zc,innerRadius,outerRadius,height):
    global E
    if innerRadius>outerRadius:
        print('Error: innerRadius bigger than outerRadius.')
        return
    gcode.write('\n')
```

```
    gcode.write(';Cylinder: Pathing is ')
    gcode.write(pathing)
    gcode.write(',xc ')
    gcode.write(str(xc))
    gcode.write(',yc ')
    gcode.write(str(yc))
    gcode.write(',zc ')
    gcode.write(str(zc))
    gcode.write('\n')
    gcode.write(';innerRadius ')
    gcode.write(str(innerRadius))
    gcode.write(',outerRadius ')
    gcode.write(str(outerRadius))
    gcode.write(',height ')
    gcode.write(str(height))
    gcode.write('\n')
    sliceCount=math.ceil(height/layerHeight)

    if pathing=='concentric':
        C='G1' #'Controlled Move' extrude-move G-code
        F=2700.000
        radialRoads=math.ceil((outerRadius-innerRadius)/fibreWidth)
        #Retract extruder:
        gcode.write('G1 F9000.000 E-2.500\n')
        gcode.write('G1 F9000.000 E0.0\n')
        for sliceIterate in np.arange(1,sliceCount+1):
            Z=zc+sliceIterate*layerHeight
            gcode.write('G92 E0\n')
            E=0.0
            for radialIterate in np.arange(radialRoads):
                pathRadius=innerRadius+radialIterate*fibreWidth
                stepsInCircle=60
                if pathRadius<2.4:
                    stepsInCircle=30
                for theta in np.linspace(0,2*math.pi,num=stepsInCircle): #
                    Circle is divided into straight-line segments.
                    if pathRadius==0.0:
                        break
                    if theta==0.0:
                        dE=0.0
                        F=4500.000
                    else:
                        dE=dEpermm
                        F=2700.000

                    X=round(xc+pathRadius*math.cos(theta),3)
                    Y=round(yc+pathRadius*math.sin(theta),3)
                    E=round(E+dE*(pathRadius*2*math.pi/stepsInCircle),3)
                    sendCommand(C,X,Y,Z,F,E)


def block(pathAngleDeg,x0,y0,z0,xLength,yLength,height):
    global E


    if xLength>yLength:
        print("To save me a lot of coding, just set xLength<yLength.")
        return

    pathAngleDeg=float(pathAngleDeg)
    pathAngleRad=pathAngleDeg*2.0*math.pi/360.0

    sliceCount=math.ceil(height/layerHeight)
    C='G1' #'Controlled Move' extrude-move G-code
    F=2700.000

    #Retract extruder:
```

```
gcode.write('G1 F9000.000 E-2.500\n')
gcode.write('G1 F9000.000 E0.0\n')
if pathAngleDeg<0.0:
    print("pathAngleDeg must be >=0 and <=90")

if pathAngleDeg>90.0:
    print("pathAngleDeg must be >=0 and <=90")

if pathAngleDeg==0.0:
    xSlicePointCount=math.ceil((xLength/fibreWidth))
    ySlicePointCount=0
    xHalfSlice=xSlicePointCount/2.0
    for sliceIterate in np.arange(1,sliceCount+1):
        Z=z0+sliceIterate*layerHeight
        gcode.write('G92 E0\n')
        E=0.0
        for passNumber in np.arange(xHalfSlice):
            xRel=fibreWidth*passNumber*2.0
            #One 'pass' is two roads width: (1)start, (2) extrude to
                the end, (3) move to the next roads end, (4) extrude
                back to start.
            #First point of pass:
            X=x0+xRel
            Y=y0
            E=round(E+dEpermm*fibreWidth*2.0,5)
            sendCommand(C,X,Y,Z,F,E)
            #Second point of pass:
            Y=y0+yLength
            E=round(E+dEpermm*yLength,5)
            sendCommand(C,X,Y,Z,F,E)
            #Third point of pass:
            E=round(E+dEpermm*fibreWidth*2.0,5)
            X=X+fibreWidth
            sendCommand(C,X,Y,Z,F,E)
            #Fourth point of pass:
            Y=y0
            E=round(E+dEpermm*yLength,5)
            sendCommand(C,X,Y,Z,F,E)

if pathAngleDeg==90.0:
    xSlicePointCount=0
    ySlicePointCount=math.ceil((yLength/fibreWidth))
    yHalfSlice=ySlicePointCount/2.0
    for sliceIterate in np.arange(1,sliceCount+1):
        Z=z0+sliceIterate*layerHeight
        gcode.write('G92 E0\n')
        E=0.0
        for passNumber in np.arange(yHalfSlice):
            yRel=fibreWidth*passNumber*2.0
            #One 'pass' is two roads width: (1)start, (2) extrude to
                the end, (3) move to the next roads end, (4) extrude to
                next start position.
            #First point of pass:
            Y=y0+yRel
            X=x0
            E=round(E+dEpermm*fibreWidth*2.0,5)
            sendCommand(C,X,Y,Z,F,E)
            #Second point of pass:
            X=x0+xLength
            E=round(E+dEpermm*xLength,5)
            sendCommand(C,X,Y,Z,F,E)

            #Third point of pass:
            E=round(E+dEpermm*fibreWidth*2.0,5)
            Y=Y+fibreWidth
            sendCommand(C,X,Y,Z,F,E)
```

```
            #Fourth point of pass:
            X=x0
            E=round(E+dEpermm*xLength,5)
            sendCommand(C,X,Y,Z,F,E)

    if pathAngleDeg>0.0 and pathAngleDeg<90.0:
        xSlicePointCount=math.floor((xLength/fibreWidth)*math.cos(
            pathAngleRad))
        ySlicePointCount=math.floor((yLength/fibreWidth)*math.sin(
            pathAngleRad))
        #Make xSlicePointCount and ySlicePointCount even:
        if xSlicePointCount%2==1:
            xSlicePointCount=xSlicePointCount+1
        if ySlicePointCount%2==1:
            ySlicePointCount=ySlicePointCount+1

        xHalfSlice=xSlicePointCount/2.0
        xBottomPoints=np.array([])
        xTopPoints=np.array([])
        yLeftPoints=np.array([])
        yRightPoints=np.array([])

        for i in np.arange(xSlicePointCount):
            xBottomPoints=np.append(xBottomPoints,[x0+i*xLength/
                xSlicePointCount])
            xTopPoints=np.append(xTopPoints,[x0+i*xLength/xSlicePointCount
                ])

        for i in np.arange(ySlicePointCount):
            yLeftPoints=np.append(yLeftPoints,[y0+yLength-i*yLength/
                ySlicePointCount])
            yRightPoints=np.append(yRightPoints,[y0+yLength-i*yLength/
                ySlicePointCount])

        for sliceIterate in np.arange(1,sliceCount+1):
            Z=z0+sliceIterate*layerHeight
            gcode.write('G92 E0\n')
            E=0.0

            #STAGE 1: Infill Top-Left Corner:
            X=x0
            Y=y0+yLength
            for passNumber in np.arange(xHalfSlice):
                #One 'pass' is two roads width: (1)start, (2) extrude to
                    the end, (3) move to the next roads end, (4) extrude to
                    next start position.
                #First point of pass:
                countIn=passNumber*2
                X=x0
                Y=yLeftPoints[countIn]
                xOld=X
                yOld=Y
                E=round(E+dEpermm*fibreWidth*2.0,5)
                sendCommand(C,X,Y,Z,F,E)

                #Second point of pass:
                X=xTopPoints[countIn]
                Y=y0+yLength
                E=round(E+dEpermm*(math.sqrt((X-xOld)**2.0+(Y-yOld)**2.0))
                    ,5)
                sendCommand(C,X,Y,Z,F,E)

                #Third point of pass:
                X=xTopPoints[countIn+1]
                xOld=X
                yOld=Y
```

```
        E=round(E+dEpermm*fibreWidth*2.0,5)
        sendCommand(C,X,Y,Z,F,E)

        #Fourth point of pass:
        X=x0
        Y=yLeftPoints[countIn+1]
        E=round(E+dEpermm*(math.sqrt((X-xOld)**2.0+(Y-yOld)**2.0))
            ,5)
        sendCommand(C,X,Y,Z,F,E)

    #STAGE 2: Infill middle (inherits X,Y coordinates from previous
        block):
    for passNumber in np.arange((ySlicePointCount-xSlicePointCount)
        /2):
        #One 'pass' is two roads width: (1)start, (2) extrude to
            the end, (3) move to the next roads end, (4) extrude
            back to start.
        #First point of pass:
        countIn=passNumber*2
        X=x0
        Y=yLeftPoints[countIn+xSlicePointCount]
        xOld=X
        yOld=Y
        E=round(E+dEpermm*fibreWidth*2.0,5)
        sendCommand(C,X,Y,Z,F,E)

        #Second point of pass:
        Y=yRightPoints[countIn]
        X=x0+xLength
        E=round(E+dEpermm*(math.sqrt((X-xOld)**2.0+(Y-yOld)**2.0))
            ,5)
        sendCommand(C,X,Y,Z,F,E)

        #Third point of pass:
        Y=yRightPoints[countIn+1]
        xOld=X
        yOld=Y
        E=round(E+dEpermm*fibreWidth*2.0,5)
        sendCommand(C,X,Y,Z,F,E)

        #Fourth point of pass:
        X=x0
        Y=yLeftPoints[countIn+1+xSlicePointCount]
        E=round(E+dEpermm*(math.sqrt((X-xOld)**2.0+(Y-yOld)**2.0))
            ,5)
        sendCommand(C,X,Y,Z,F,E)

    yCountUsed=countIn+2
    #STAGE 3: Infill Bottom Right (inherits X,Y coordinates from
        previous block):
    for passNumber in np.arange(xHalfSlice):
        #One 'pass' is two roads width: (1)start, (2) extrude to
            the end, (3) move to the next roads end, (4) extrude
            back to start.
        #First point of pass:
        countIn=passNumber*2
        Y=y0
        X=xBottomPoints[countIn]
        xOld=X
        yOld=Y
        E=round(E+dEpermm*fibreWidth*2.0,5)
        sendCommand(C,X,Y,Z,F,E)

        #Second point of pass:
        X=x0+xLength
        Y=yRightPoints[countIn+yCountUsed]
```

```
                E=round(E+dEpermm*(math.sqrt((X-xOld)**2.0+(Y-yOld)**2.0))
                    ,5)
                sendCommand(C,X,Y,Z,F,E)

                #Third point of pass:
                Y=yRightPoints[countIn+yCountUsed+1]
                xOld=X
                yOld=Y
                E=round(E+dEpermm*fibreWidth*2.0,5)
                sendCommand(C,X,Y,Z,F,E)

                #Fourth point of pass:
                X=xBottomPoints[countIn+1]
                Y=y0
                E=round(E+dEpermm*(math.sqrt((X-xOld)**2.0+(Y-yOld)**2.0))
                    ,5)
                sendCommand(C,X,Y,Z,F,E)

    #Raise Z-axis:
    gcode.write('G91\n')
    gcode.write('G1 Z50 F50\n')
    gcode.write('G90\n')


def endGcode():
    #Retract code:
    global E
    E=E-2.500
    gcode.write('G1 F9000.000 E')
    gcode.write(str(E))
    gcode.write('\n')

    #Set E datum to 0:
    gcode.write('G92 E0\n')

    #Raise Z-axis:
    gcode.write('G91\n')
    gcode.write('G1 Z50 F50\n')
    gcode.write('G90\n')

    #Home All Axes
    gcode.write('G28 X0 Y0\n')

    gcode.close()
####################### END OF GCODE DEFINITIONS #######################

########################## Specimen Definition ##########################
#Cylinder parameters: pathing,xc,yc,zc,innerRadius,outerRadius,height
#Block parameters: pathAngleDeg,x0,y0,z0,xLength,yLength,height

startGcode()

#Uncomment the shapes to be printed:

#Small Printer Calibration Test Block:
#block(0.0,100.0,50.0,0.0,10.0,10.0,2.0)

#Straight Cylindrical Pressure Vessel using two cylinders:
#Will produce cylinder with 10mm thick cap-end and 10mm ID.
#cylinder('concentric',100.0,100.0,0.0,0.0,10.0,10.0)
#cylinder('concentric',100.0,100.0,10.0,5.0,10.0,20.0)

#0 degree ASTMD3039 Specimen in middle of build area:
#block(0.0,90.0,7.5,0.0,25.0,185.0,2.0)

#10 degree ASTMD3039 Specimen in middle of build area:
#block(10.0,90.0,7.5,0.0,25.0,185.0,2.0)
```

```
#45 degree ASTMD3039 Specimen in middle of build area:
#block(45.0,90.0,7.5,0.0,25.0,185.0,2.0)

#60 degree ASTMD3039 Specimen in middle of build area:
#block(60.0,90.0,7.5,0.0,25.0,185.0,2.0)

#90 degree ASTMD3039 Specimen in middle of build area:
#block(90.0,90.0,7.5,0.0,25.0,185.0,2.0)

endGcode()
```

Appendix B: Derivation of Multiaxial Strength Theory

The interaction formula states that failure occurs if one of the equations B.1–B.3 are satisfied:

$$(\frac{\sigma_x}{S_x})^2 - \frac{\sigma_x\sigma_y}{S_xS_y} + (\frac{\sigma_y}{S_y})^2 + (\frac{\tau_{xy}}{S_{xy}})^2 = 1 \tag{B.1}$$

$$(\frac{\sigma_y}{S_y})^2 - \frac{\sigma_y\sigma_z}{S_yS_z} + (\frac{\sigma_z}{S_z})^2 + (\frac{\tau_{yz}}{S_{yz}})^2 = 1 \tag{B.2}$$

$$(\frac{\sigma_x}{S_x})^2 - \frac{\sigma_x\sigma_z}{S_xS_z} + (\frac{\sigma_z}{S_z})^2 + (\frac{\tau_{xz}}{S_{xz}})^2 = 1 \tag{B.3}$$

As we are tensile testing a thin plate, the plane stress and uniaxial stress assumptions apply: $\sigma_z = 0$,$\tau_{xz} = \tau_{zx} = \tau_{yz} = \tau_{zy} = 0$. The interaction formula therefore reduces to

$$(\frac{\sigma_x}{S_x})^2 - \frac{\sigma_x\sigma_y}{S_xS_y} + (\frac{\sigma_y}{S_y})^2 + (\frac{\tau_{xy}}{S_{xy}})^2 = 1 \tag{B.4}$$

The stress and strength components are described in global coordinates[1], however, not material coordinates. If the coordinates are transformed using Equation 4.1, the interaction formula becomes:

$$(\frac{\sigma_x \cos^2\theta}{S_1})^2 - \frac{\sigma_x^2 \cos^2\theta \sin^2\theta}{S_1S_2} + (\frac{\sigma_x}{S_y})^2 + (\frac{-\sigma_x \cos\theta \sin\theta}{S_{12}})^2 = 1 \tag{B.5}$$

The interaction formula does not allow for the effect of combined stresses, however. Allowing for these effects transforms the interaction formula to the aforementioned Azzi and Tsai multiaxial strength theory (Chamis and Sinclair, 1976):

$$(\frac{\sigma_x \cos^2\theta}{S_1})^2 - \frac{\sigma_x^2 \cos^2\theta \sin^2\theta}{S_1^2} + (\frac{\sigma_x}{S_y})^2 + (\frac{-\sigma_x \cos\theta \sin\theta}{S_{12}})^2 = 1 \tag{B.6}$$

[1]Where x describes the tensile axis and y,z describe the axes orthogonal to this.

which simplifies to

$$(\frac{\sigma_x \cos^2\theta}{S_1})^2 - (\frac{1}{S_{12}^2} - \frac{1}{S_1^2})\sigma_x^2 \cos^2\theta \sin^2\theta + (\frac{\sigma_x}{S_y})^2 = 1 \tag{B.7}$$

Failure occurs when this equation is satisfied.

Appendix C: Tensile Testing Results

The tensile testing data, as output from the Bluehill 3 software, is presented on the following pages. It should be noted that the 'Maximum Load' and 'Tensile Stress at Maximum Load' tabulated data are sometimes incorrect; this is due to a flaw in the software, and can be seen from comparison with the loading curves for those cases. This tabulated data was not used in the experiment – a post-processor was written to plot and calculate the material data.

Test Report

Cross Head Speed	2.000 mm/min

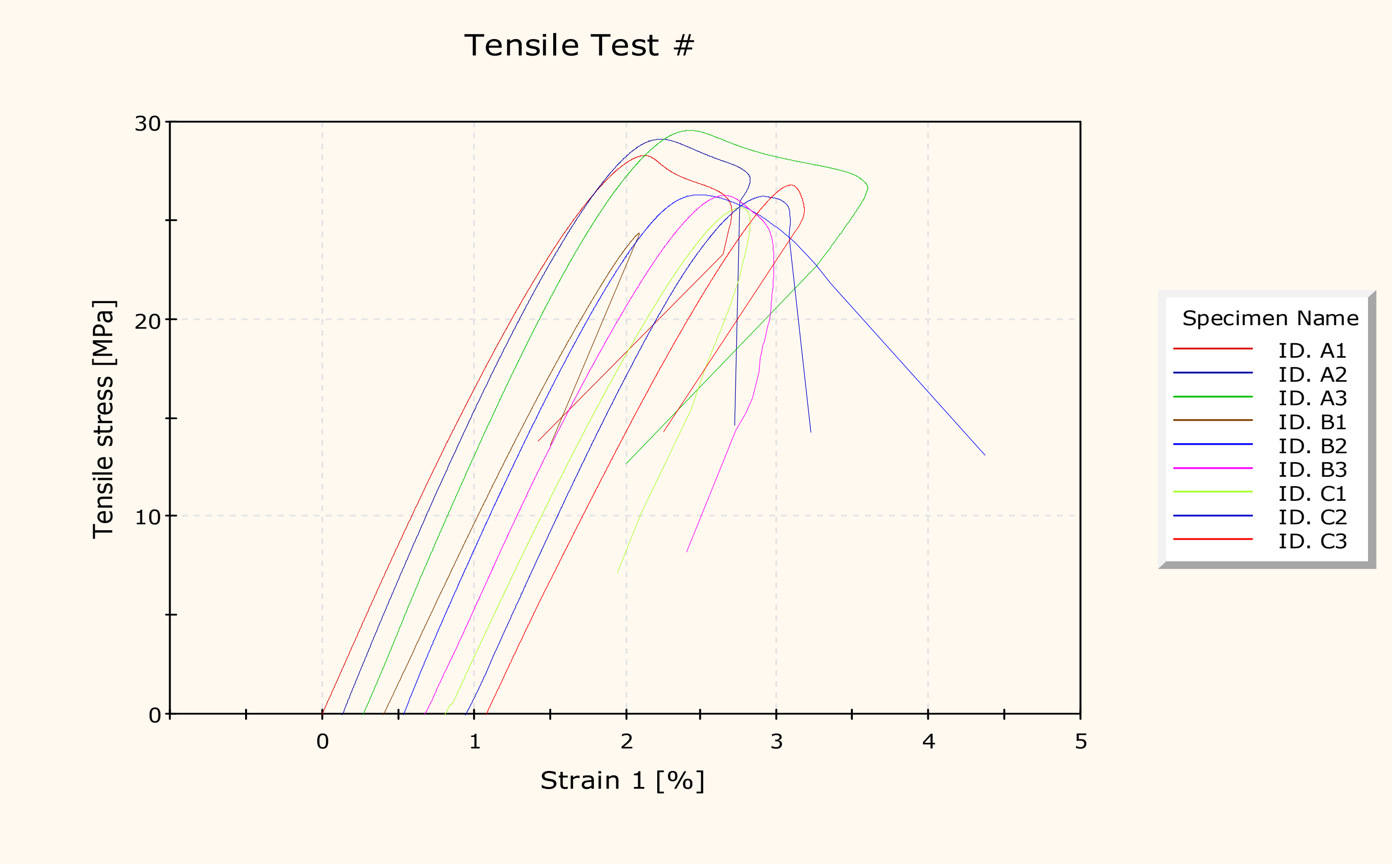

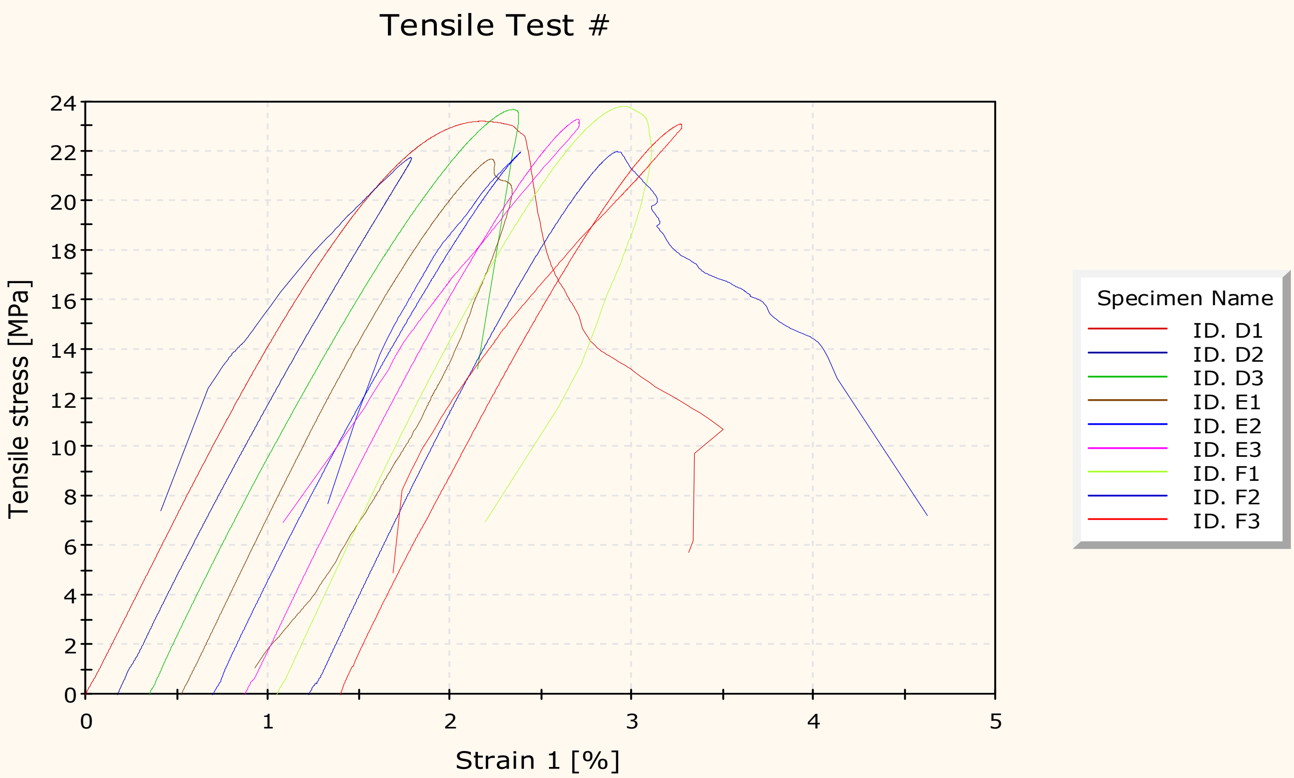

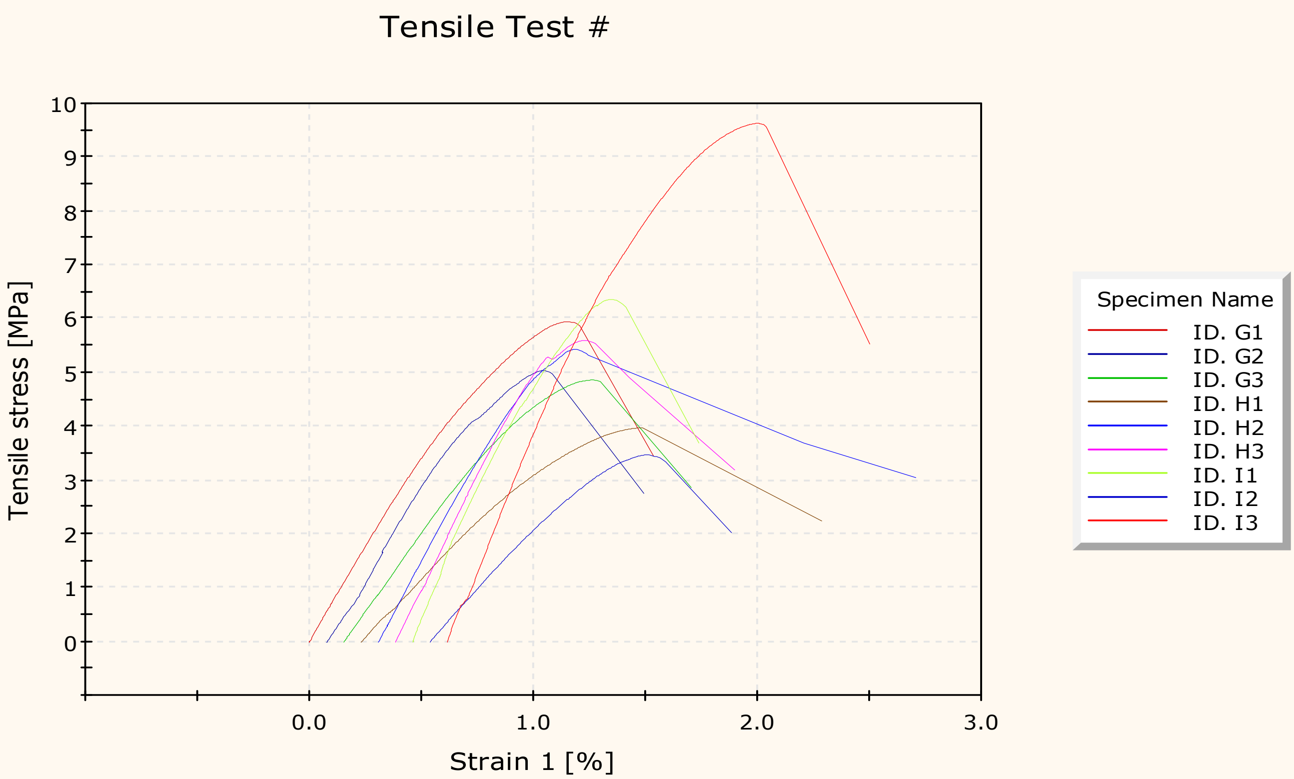

Results

	Specimen label	Thickness [mm]	Width [mm]	Maximum Load [N]	Tensile stress at Maximum Load [MPa]
1	ID. A1	1.820	25.720	1,191	25

	Specimen label	Thickness [mm]	Width [mm]	Maximum Load [N]	Tensile stress at Maximum Load [MPa]
2	ID. A2	1.710	25.740	1,191	27
3	ID. A3	1.710	25.740	1,174	27
4	ID. B1	1.900	25.600	1,184	24
5	ID. B2	1.900	25.770	643	13
6	ID. B3	1.920	25.720	1,125	23
7	ID. C1	1.960	25.770	1,253	25
8	ID. C2	1.890	25.700	694	14
9	ID. C3	1.910	25.540	1,247	26
10	ID. D1	2.010	25.180	543	11
11	ID. D2	1.890	25.700	1,054	22
12	ID. D3	1.910	25.700	1,150	23
13	ID. E1	1.910	25.700	999	20
14	ID. E2	1.930	25.700	1,089	22
15	ID. E3	1.930	25.700	1,153	23
16	ID. F1	1.860	25.700	1,054	22
17	ID. F2	1.910	25.700	356	7
18	ID. F3	1.910	25.700	1,128	23
19	ID. G1	1.980	25.700	176	3
20	ID. G2	1.950	25.710	138	3
21	ID. G3	1.960	25.710	145	3
22	ID. H1	1.990	24.950	112	2
23	ID. H2	1.970	25.250	152	3
24	ID. H3	1.970	24.960	157	3
25	ID. I1	1.830	24.820	168	4
26	ID. I2	2.110	24.710	106	2
27	ID. I3	1.950	24.790	267	6

Test Report

Cross Head Speed	2.000 mm/min

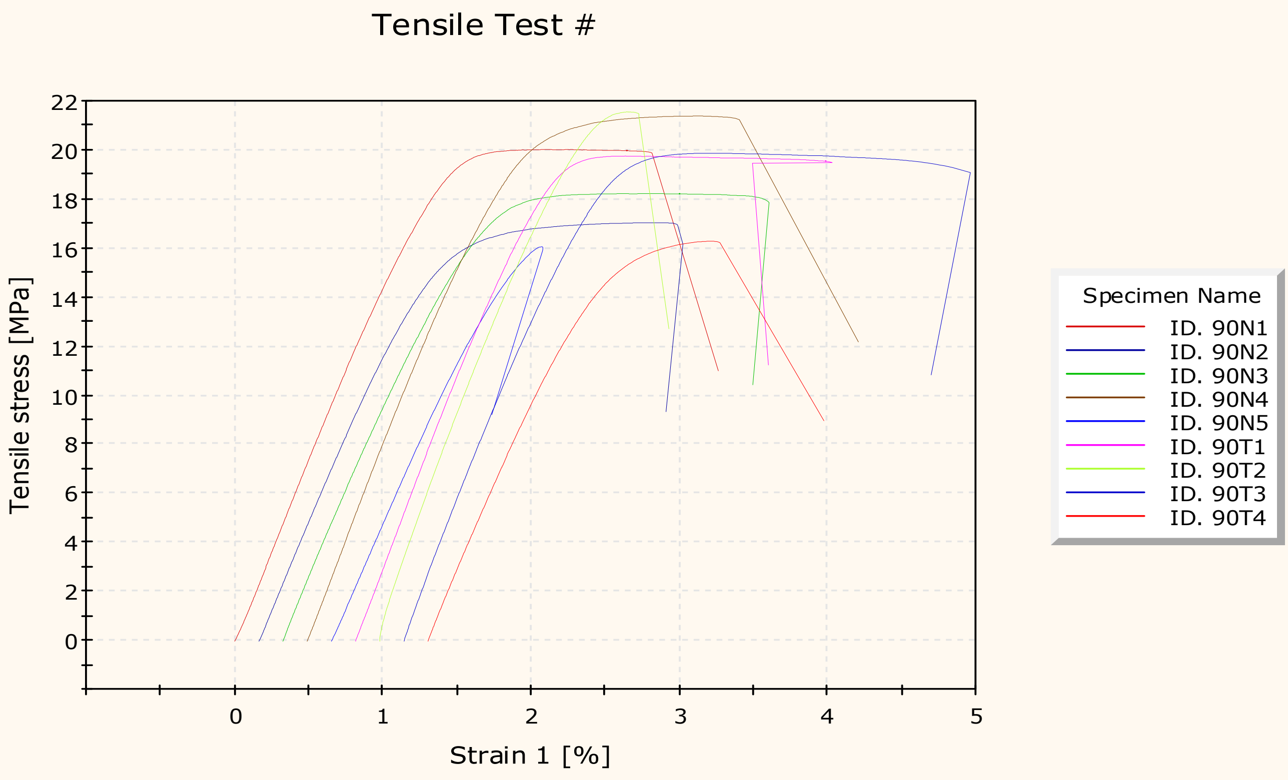

Tensile Test #

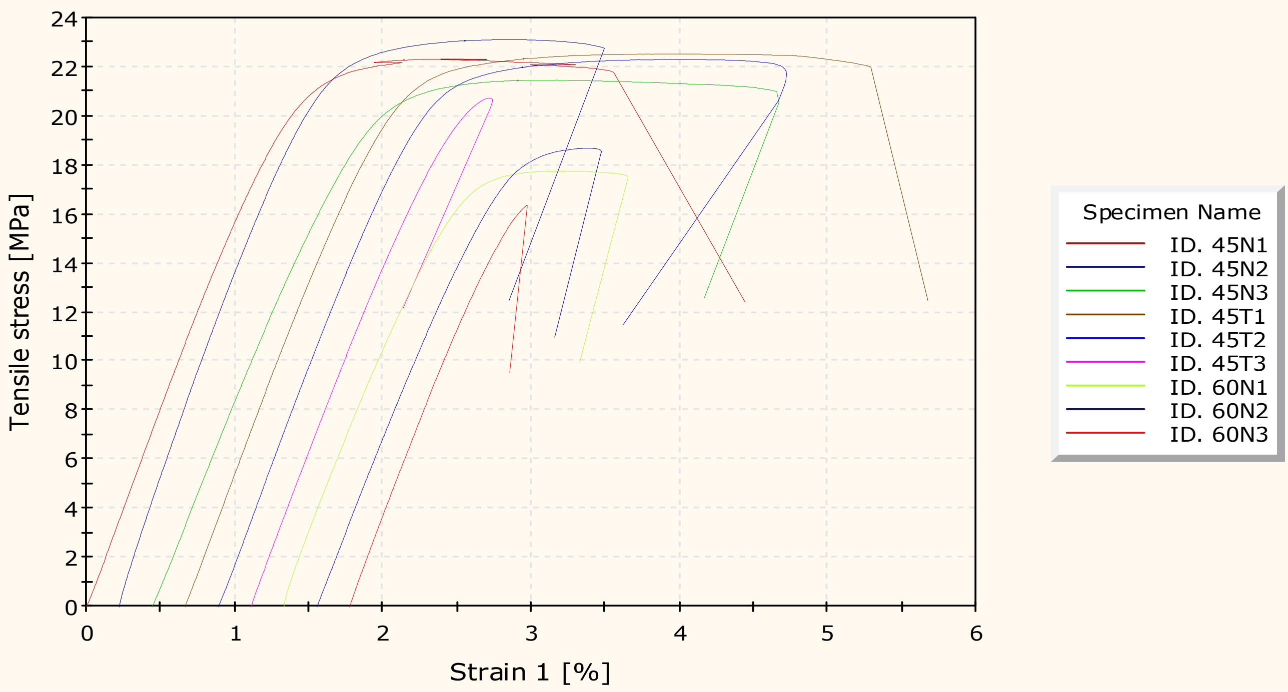

Tensile Test #

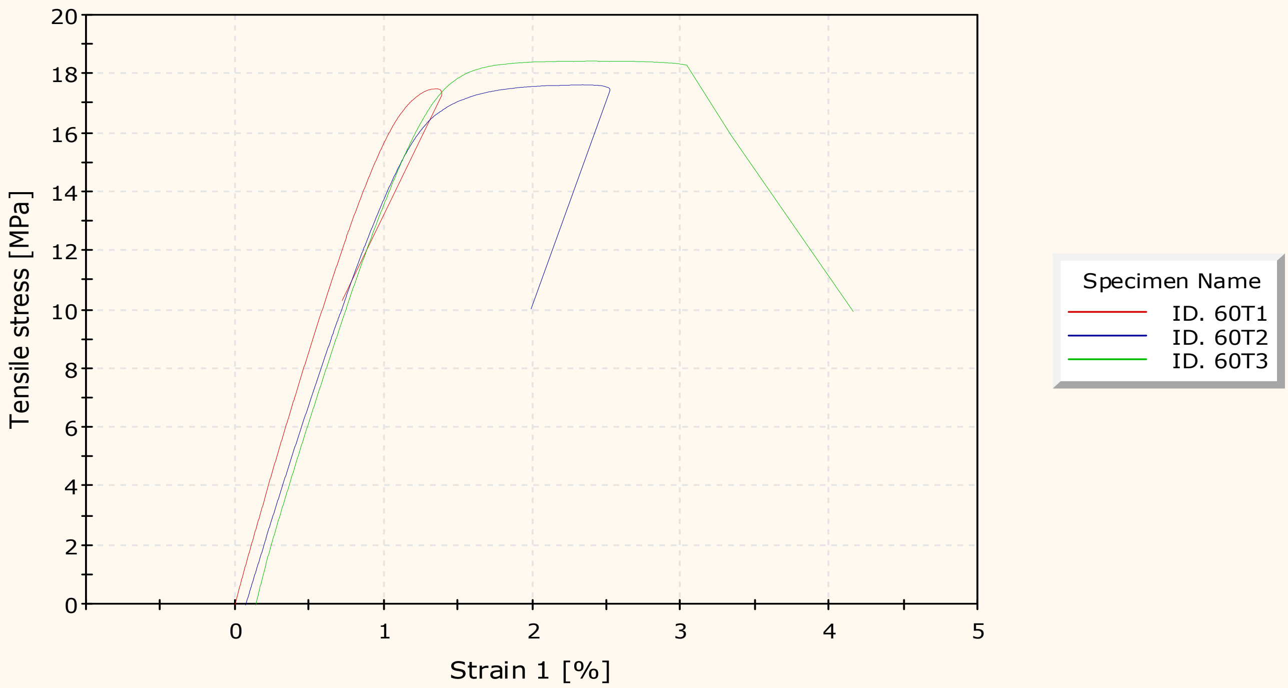

Results

	Specimen label	Thickness [mm]	Width [mm]	Maximum Load [N]	Tensile stress at Maximum Load [MPa]
1	ID. 90N1	2.400	25.800	681	11

	Specimen label	Thickness [mm]	Width [mm]	Maximum Load [N]	Tensile stress at Maximum Load [MPa]
2	ID. 90N2	2.340	25.600	968	16
3	ID. 90N3	2.400	25.900	1,110	18
4	ID. 90N4	2.300	25.900	725	12
5	ID. 90N5	2.300	25.980	955	16
6	ID. 90T1	2.450	24.200	1,155	19
7	ID. 90T2	2.550	24.200	785	13
8	ID. 90T3	2.500	24.000	1,145	19
9	ID. 90T4	2.400	24.000	517	9
10	ID. 45N1	2.150	26.200	699	12
11	ID. 45N2	2.120	26.100	1,259	23
12	ID. 45N3	2.300	26.100	1,233	21
13	ID. 45T1	2.360	24.500	721	12
14	ID. 45T2	2.400	24.800	1,292	22
15	ID. 45T3	2.350	24.600	1,192	21
16	ID. 60N1	2.350	25.900	1,064	17
17	ID. 60N2	2.380	26.020	1,148	19
18	ID. 60N3	2.350	24.600	945	16
19	ID. 60T1	2.350	24.300	989	17
20	ID. 60T2	2.450	24.700	1,058	17
21	ID. 60T3	2.400	24.500	585	10

Appendix D: ABS PA-747 Properties

Relevant material properties are tabulated in Table 3.1 in Section 3.3. The relevant bulk material data was supplied by (Chi-Mei-Corporation, 2006). The datasheet supplied by *Chi-Mei Corporation* is attached overleaf.

Chi Mei Polylac® PA-747 ABS

Categories: Polymer; Thermoplastic; ABS Polymer; Acrylonitrile Butadiene Styrene (ABS), Molded

Material Notes: High impact

Vendors: No vendors are listed for this material. Please click here if you are a supplier and would like information on how to add your listing to this material.

Physical Properties	Metric	English	Comments
Density	1.03 g/cc	0.0372 lb/in³	ISO 1183
Linear Mold Shrinkage	0.0030 - 0.0070 cm/cm	0.0030 - 0.0070 in/in	ASTM D955
Melt Flow	1.2 g/10 min @Load 5.00 kg, Temperature 200 °C	1.2 g/10 min @Load 11.0 lb, Temperature 392 °F	ASTM D1238
	13 g/10 min @Load 10.0 kg, Temperature 220 °C	13 g/10 min @Load 22.0 lb, Temperature 428 °F	ISO-1133

Mechanical Properties	Metric	English	Comments
Hardness, Rockwell R	108	108	ASTM D785
Ball Indentation Hardness	88.0 MPa	12800 psi	H358/30; ISO 2039-1
Tensile Strength at Break	31.0 MPa	4500 psi	50 mm/min; ISO 527
Tensile Strength, Yield	39.0 MPa	5660 psi	50 mm/min; ISO 527
Elongation at Break	45 %	45 %	50 mm/min; ISO 527
Flexural Strength	58.0 MPa	8410 psi	2 mm/min; ISO 178
Flexural Modulus	1.80 GPa	261 ksi	2 mm/min; ISO 178
Izod Impact, Notched	3.66 J/cm @Thickness 6.35 mm	6.86 ft-lb/in @Thickness 0.250 in	ASTM D256
	4.15 J/cm @Thickness 3.17 mm	7.77 ft-lb/in @Thickness 0.125 in	ASTM D256
Izod Impact, Notched (ISO)	29.0 kJ/m²	13.8 ft-lb/in²	ISO 180/1A
Izod Impact, Unnotched (ISO)	NB	NB	ISO 180/1C
Charpy Impact Unnotched	NB	NB	ISO 179
Charpy Impact, Notched	3.00 J/cm²	14.3 ft-lb/in²	ISO 179

Thermal Properties	Metric	English	Comments
Deflection Temperature at 1.8 MPa (264 psi)	86.0 °C	187 °F	unannealed; ISO 75
	96.0 °C	205 °F	annealed; ISO 75
Vicat Softening Point	92.0 °C @Load 5.00 kg	198 °F @Load 11.0 lb	50°C/hr; ISO 306
	94.0 °C @Load 5.00 kg	201 °F @Load 11.0 lb	120°C/hr; ISO 306
	101 °C @Load 1.00 kg	214 °F @Load 2.20 lb	50°C/hr; ISO 306
			120°C/hr; ISO 306

	103 °C @Load 1.00 kg	217 °F @Load 2.20 lb	
Flammability, UL94	HB @Thickness 1.59 mm	HB @Thickness 0.0625 in	UL 94

Processing Properties	Metric	English	Comments
Rear Barrel Temperature	193 °C	380 °F	
Middle Barrel Temperature	216 °C	420 °F	
Front Barrel Temperature	227 °C	440 °F	
Melt Temperature	232 - 260 °C	450 - 500 °F	Nozzle temp not greater than stock
Mold Temperature	48.9 - 65.6 °C	120 - 150 °F	
Drying Temperature	87.8 - 93.3 °C	190 - 200 °F	
Dry Time	2 - 24.0 hour	2 - 24.0 hour	
Injection Pressure	68.9 - 82.7 MPa	10000 - 12000 psi	
Back Pressure	0.689 MPa	100 psi	
Screw Speed	50 - 60 rpm	50 - 60 rpm	

Descriptive Properties	
Impact Flexural Test Notched (KJ/m²)	20
Impact Flexural Test Unnotched (KJ/m²)	NB